NASA CR-121110

THEORETICAL ANALYSIS OF IMPACT IN COMPOSITE PLATES

by F. C. Moon

prepared for

NATIONAL AERONAUTICS AND SPACE ADMINISTRATION

NASA Lewis Research Center

Contract NAS 3-14331

PRINCETON UNIVERSITY

Department of Aerospace and Mechanical Sciences

AMS Report No. 1099

1. Report No.	2. Government Accession No.	3. Recipient's Catalog No.
NASA CR-121110		

4. Title and Subtitle	5. Report Date
THEORETICAL ANALYSIS OF IMPACT IN COMPOSITE PLATES (U)	6. Performing Organization Code

7. Author(s)	8. Performing Organization Report No.
Francis C. Moon	AMS Report No. 1099
	10. Work Unit No.

9. Performing Organization Name and Address	11. Contract or Grant No.
4 Aero Lab. Department of Aerospace and Mechanical Sciences Princeton University Princeton, N. J. 08540	NAS 3-14331
	13. Type of Report and Period Covered Contractor Report

12. Sponsoring Agency Name and Address	14. Sponsoring Agency Code
National Aeronautics and Space Administration Washington, D. C. 20546	

15. Supplementary Notes

16. Abstract

The calculated stresses and displacements induced in anisotropic plates by short duration impact forces are presented in this report. The theoretical model attempts to model the response of fiber composite turbine fan blades to impact by foreign objects such as stones and hailstones. In this model the determination of the impact force uses the Hertz impact theory. The plate response treats the laminated blade as an equivalent anisotropic material using a form of Mindlin's theory for crystal plates. The analysis makes use of a computational tool called the "fast Fourier transform". Results are presented in the form of stress contour plots in the plane of the plate for various times after impact. Examination of the maximum stresses due to impact versus ply layup angle reveals that the $\pm 15^{\circ}$ layup angle gives lower flexural stresses than 0°, $\pm 30^{\circ}$ and $\pm 45^{\circ}$ cases.

(U)

17. Key Words (Suggested by Author(s))	18. Distribution Statement
Impact Stresses, Composite Plates, Stress Waves	Unclassified-unlimited

19. Security Classif. (of this report)	20. Security Classif. (of this page)	21. No. of Pages	22. Price*
Unclassified	Unclassified	100	$3.00

* For sale by the National Technical Information Service, Springfield, Virginia 22151

ABSTRACT

The calculated stresses and displacements induced in anisotropic plates by short duration impact forces are presented in this report. The theoretical model attempts to model the response of fiber composite turbine fan blades to impact by foreign objects such as stones and hailstones. In this model the determination of the impact force uses the Hertz impact theory. The plate response treats the laminated blade as an equivalent anisotropic material using a form of Mindlin's theory for crystal plates. The analysis makes use of a computational tool called the "fast Fourier transform". Results are presented in the form of stress contour plots in the plane of the plate for various times after impact. Examination of the maximum stresses due to impact versus ply layup angle reveals that the ±15° layup angle gives lower flexural stresses than 0°, ±30° and ±45° cases, for 55% graphite fiber-epoxy matrix composite plates.

TABLE OF CONTENTS

SUMMARY

This report summarizes the recent progress in the attempt to model foreign object impact of fiber composite fan blades by small objects such as stones and hardstones. The high speed impact of these objects with composite materials should result in short duration impact times (< 100 μsec). In the present model the composite blade is represented by an anisotropic plate of infinite extent. Thus only the mechanics in the area of the impact point are studied. The effect of edges and stress wave reflection are not treated in this report, though work is proceeding on this aspect of the problem.

The combined impact contact dynamics and plate response are separated into two sub-problems. The impact force time history is determined from the Hertz contact theory for a half space, while the plate response is determined from an assumed impact pressure distribution over the impact contact area. Linear elastodynamics is used, neglecting viscoelastic-plastic, nonlinear and fracture effects. Thus it is hoped that the model will predict, prefracture or predamage stresses.

Using an approximate theory of anisotropic plates due to Mindlin, five waves are shown to make up the main part of the motion. Two of the waves involve inplane displacements while the other three waves involve flexural plate motion. The analysis makes use of a computational tool called the fast Fourier transform. Several computer programs were developed to calculate the stress levels behind the wave fronts due to a specified impact force distribution. The output of these programs are

in the form of stress contour plots. It was generally found that the stress levels were highest in directions along the fibers. Also the maximum stresses appear to propagate in the lowest flexural mode. These waves are found to be highly dispersive and change their shape as the wave propagates. Examination of the maximum stresses due to impact versus ply layup angle, reveals that the ±15° layup angle gives lower flexural stresses than 0°, 30°, and 45° cases. The flexural stresses for the 15° case are 34% lower than those for the 45° layup angle case. For the interlaminar shear stresses, the values seem to be insensitive to layup angle. For the average membrane stresses due to inplane motion, the values immediately after impact appear to be lower for the lower fiber layup angles. The flexural stresses are found to depend on the ratio of impact object radius to plate thickness.

Continued work is in progress on the edge impact problem and the effect of leading edge protection.

INTRODUCTION

This research has been motivated by recent attempts to study the impact resistance of fiber composite materials. These materials are being considered for application to jet engine fan or compressor blades and must withstand the forces of impact due to the ingestion of objects such as birds, stones, or hailstones at speeds up to 500 meters per second. Recognizing, of course, that inelastic deformation will occur at the impact point, we none the less pursue an elastic analysis as a prelude to the more difficult task of predicting permanent damage. In this report we are interested principally in how the energy propagates away from the impacted area. It has been observed that damage in these fiber composite plates occurs away from the impact area near edges and boundaries as well as at the impact point.

In a previous paper (ref. 1), the author presented a mathematical model for stress wave propagation in anisotropic plates based on the work of Mindlin and co-workers. Five partial differential equations of motion were obtained for orthotropic symmetry in which the inplane and flexural motion were described. The two-dimensional velocity and wave surfaces were presented and the principal vibratory direction of particle motion for each wave normal was presented.

Section II will present an analysis of the two-dimensional impact problem. This analysis is based on the use of a Laplace transform on time and a two-dimensional Fourier transform on the

space variables. The solution permits the analytical inversion of the Laplace transform while a computational tool called the "Fast Fourier Transform" (ref. 2) is used to numerically invert the Fourier transform solution. Estimates of the impact time and force are made using the Hertz impact theory.

As a preliminary to the two-dimensional problem, the author tried this analytical-computational technique on a few simpler, one-dimensional wave problems. This section will present the results of that study. Displacement and stresses are calculated for a short duration line force normal to an anisotropic plate. The responses for various fiber layup angles are compared.

SECTION I: ONE-DIMENSIONAL TRANSIENT WAVES IN ANISOTROPIC PLATES

The mathematical model used in this paper is called an effective modulus theory of composites. The model is valid so long as the scale of the changes in stress levels (e.g. wavelength) is much larger than the sizes of the composite constituents (e.g. fiber diameter, ply spacing, etc.). This assumption has been used by many researchers to derive equivalent elastic constants from long wavelength or long pulse length wave propagation tests (e.g. Tauchert and Moon, (ref. 3)). Equivalent moduli determined in this way have checked very closely with elastic constants obtained from static and vibratory tests. Tauchert and Guzelsu (ref. 4), have used ultrasonic tests to measure dispersion in composites and found no significant departure from the effective modulus theory for longitudinal waves in boron fiber/epoxy matrix composites until the frequency exceeded 5 megahertz. Shear waves, however, began to show dispersion at about 0.5 megahertz. This corresponds to a wavelength to fiber diameter ratio of about 40. Sun et al. (ref. 5), in calculation on laminated composites, reports similar results. Thus the effective modulus theory used in this paper is subject to the restriction that the impact pulse spectrum have its most significant wavelengths greater than about 100 times the fiber diameter. Further discussion of dispersion in composites may be found in a review of the subject by the author, (ref. 6).

Equations of Motion

In the approximate theory of elastic plates in this study (ref. 7), the displacement is expanded in the thickness variable by using Legendre

polynomials $P_n(\eta)$,

$$\underset{\sim}{u} = \sum_{n=o}^{\infty} P_n(\eta)\underset{\sim}{u}^{(n)}(x_1, x_3, t) \tag{I-1}$$

where $\eta = x_2/b$, b is the half thickness, (see Fig. I-1). A variational method is used to obtain the equations of motion. For the purpose of this work, the series was truncated at $n = 2$, with only seven terms used; namely, u_1^0, u_2^0, u_3^0, u_1^1, u_2^1, u_3^1, $u_2^{(2)}$. This leaves all the strains, except e_{12}, e_{32}, as linear functions of the thickness variable η. To further simplify the equations, the inertias and high frequency terms (derivatives) of u_2^1, $u_2^{(2)}$ were dropped, resulting in explicit expressions for these terms;

$$\begin{aligned} q_2 - 2\left(C_{22}\frac{u_2^1}{b} + C_{12}\frac{\partial u_1^0}{\partial x_1} + C_{23}\frac{\partial u_3^0}{\partial x_3}\right) &= 0 \\ q_2 - 2\left(C_{22}\frac{3u_2^{(2)}}{b} + C_{12}\frac{\partial u_1^1}{\partial x_1} + C_{23}\frac{\partial u_3^1}{\partial x_3}\right) &= 0 \end{aligned} \tag{I-2}$$

where $(-q_2)$ is the transverse loading on the top plate surface. Elimination of the terms u_2^1 and $u_2^{(2)}$ from the remaining five differential equations results in the equations

$$\rho\frac{\partial^2 u_1^0}{\partial t^2} = \hat{C}_{11}\frac{\partial^2 u_1^0}{\partial x_1^2} + C_{55}\frac{\partial^2 u_1^0}{\partial x_3^2} + (C_{55} + \hat{C}_{13})\frac{\partial^2 u_3^0}{\partial x_1 \partial x_3} + \frac{C_{12}}{2C_{22}}\frac{\partial q_2}{\partial x_1} \tag{I-3a}$$

$$\rho \frac{\partial^2 u_3^0}{\partial t^3} = \hat{C}_{33} \frac{\partial^2 u_3^0}{\partial x_3^2} + C_{55} \frac{\partial^2 u_3^0}{\partial x_1^2} + (C_{55} + \hat{C}_{13}) \frac{\partial^2 u_1^0}{\partial x_1 \partial x_3} + \frac{C_{32}}{2C_{22}} \frac{\partial q_2}{\partial x_3} \tag{I-3b}$$

$$\rho \frac{\partial^2 u_2^0}{\partial t^2} = \hat{C}_{66} \left\{ \frac{\partial^2 u_2^0}{\partial x_1^2} + \frac{\partial^2 u_2^0}{\partial x_3^2} + \frac{1}{b} \frac{\partial u_1^1}{\partial x_1} + \frac{1}{b} \frac{\partial u_3^1}{\partial x_3} \right\} + \frac{q_2}{2b} \tag{I-4a}$$

$$\rho \frac{\partial^2 u_1^1}{\partial t^2} = \hat{C}_{11} \frac{\partial^2 u_1^1}{\partial x_1^2} + C_{55} \frac{\partial^2 u_1^1}{\partial x_3^2} + (C_{55} + \hat{C}_{13}) \frac{\partial^2 u_3^1}{\partial x_1 \partial x_3} - \frac{3}{b} \hat{C}_{66} \left(\frac{\partial u_2^0}{\partial x_1} + \frac{u_1^1}{b} \right) + \frac{C_{12}}{2C_{22}} \frac{\partial q_2}{\partial x_1} \tag{I-4b}$$

$$\rho \frac{\partial^2 u_3^1}{\partial t^2} = \hat{C}_{33} \frac{\partial^2 u_3^1}{\partial x_3^2} + C_{55} \frac{\partial^2 u_3^1}{\partial x_1^2} + (C_{55} + \hat{C}_{13}) \frac{\partial^2 u_1^1}{\partial x_1 \partial x_3} - \frac{3}{B} \hat{C}_{66} \left(\frac{\partial u_2^0}{\partial x_3} + \frac{u_3^1}{b} \right) + \frac{C_{32}}{2C_{22}} \frac{\partial q_2}{\partial x_3} \tag{I-4c}$$

where

$$\hat{C}_{11} = C_{11} - C_{12}^2 / C_{22}$$

$$\hat{C}_{33} = C_{33} - C_{32}^2 / C_{22}$$

$$\hat{C}_{13} = C_{13} - C_{12} C_{32} / C_{22}$$

$$\hat{C}_{66} = kC_{66}$$

In his approximate theory of crystal plates (ref. 7), Mindlin uses correction constants to adjust the thickness vibration mode to match the exact theory. Thus he replaces C_{44} and C_{66} by $k_1 C_{44}$ and $k_3 C_{66}$ respectively. In our case $C_{44} = C_{66}$ and $k_1 = k_3 = \pi^2/12$.

The stresses in the plate for orthotropic symmetry take the following form:

$$
\begin{aligned}
t_{11} &= \left\{ \hat{C}_{11} \frac{\partial u_1^0}{\partial x_1} + \hat{C}_{13} \frac{\partial u_3^0}{\partial x_3} \right\} + \frac{x_2}{b} \left\{ \hat{C}_{11} \frac{\partial u_1^1}{\partial x_1} + \hat{C}_{13} \frac{\partial u_3^1}{\partial x_3} \right\} + \frac{C_{12}}{2C_{22}} q_2 \left(1+\frac{x_2}{b}\right) \\
t_{22} &= \frac{q_2}{2} \left(1 + \frac{x_2}{b}\right) \\
t_{33} &= \left\{ \hat{C}_{33} \frac{\partial u_3^0}{\partial x_3} + \hat{C}_{13} \frac{\partial u_1^0}{\partial x_1} \right\} + \frac{x_2}{b} \left\{ \hat{C}_{33} \frac{\partial u_3^1}{\partial x_3} + \hat{C}_{13} \frac{\partial u_1^1}{\partial x_1} \right\} + \frac{C_{32}}{2C_{22}} q_2 \left(1+\frac{x_2}{b}\right) \\
t_{13} &= C_{55} \left\{ \frac{\partial u_1^0}{\partial x_3} + \frac{\partial u_3^0}{\partial x_1} \right\} + \frac{x_2}{b} C_{55} \left\{ \frac{\partial u_1^1}{\partial x_3} + \frac{\partial u_3^1}{\partial x_1} \right\}
\end{aligned}
\qquad \text{(I-5)}
$$

The interlaminar shear stresses t_{12} and t_{32} are quadratic functions of x_2 and cannot be accurately found from $\underset{\sim}{u}$. However in analogy to classical plate theories, we can integrate the original stress equations of motion to obtain

$$
\begin{aligned}
t_{21} &= \left\{1 - \left(\frac{x_2}{b}\right)^2\right\} \left\{ \frac{3}{2b} q_1 + \frac{C_{21}}{2C_{22}} \frac{\partial q_2}{\partial x_1} - \frac{3}{b} \left(\frac{\partial u_2^0}{\partial x_1} + \frac{u_1^1}{b}\right) \right\} \\
t_{23} &= \left\{1 - \left(\frac{x_2}{b}\right)^2\right\} \left\{ \frac{3}{2b} q_3 + \frac{C_{23}}{2C_{22}} \frac{\partial q_2}{\partial x_3} - \frac{3}{b} \left(\frac{\partial u_2^0}{\partial x_3} + \frac{u_3^1}{b}\right) \right\}
\end{aligned}
\qquad \text{(I-6)}
$$

The in-plane stresses t_{11}, t_{33}, t_{13} are comprised of two parts. One part is uniform through the thickness and is governed by dispersion free equations (I-3a) and (I-3b). The flexural part of the stress is linear in the thickness variable and is governed by equations (I-4a) through (I-4c) which exhibit strong dispersion of wave phenomena.

One-Dimensional Wave Solutions

We imagine an infinite plate on which a distributed load is placed along the line $\underset{\sim}{n} \cdot \underset{\sim}{x}$ = constant (see Fig. 1). The vector $\underset{\sim}{n}$ is normal to the line, and we assumed the load on the plate is independent of the position along the line. Thus the surface load has the form

$$\underset{\sim}{q}(x_1, x_3, t) = \underset{\sim}{q}(\underset{\sim}{n} \cdot \underset{\sim}{x}, t)$$

Because of this relation, the motion is also assumed to have this form, i.e.

$$u_1^0(x_1, x_3, t) = u_1^0(\underset{\sim}{n} \cdot \underset{\sim}{x}, t), \text{ etc.}$$

For derivatives of functions of this form, the following expressions are useful;

$$\frac{\partial f(\underset{\sim}{n} \cdot \underset{\sim}{x})}{\partial x_1} = f' \cos \alpha, \quad \frac{\partial f(\underset{\sim}{n} \cdot \underset{\sim}{x})}{\partial x_3} = f' \sin \alpha$$

where primes indicate differentiation with respect to the variable $\zeta = \underset{\sim}{n} \cdot \underset{\sim}{x}$, and

$$\underset{\sim}{n} \cdot \underset{\sim}{x} = x_1 \cos \alpha + x_3 \sin \alpha$$

The angle α , denotes the departure of $\underset{\sim}{n}$ from the symmetry axis $x_3 = 0$. To find solutions to the equations (I-3) and (I-4), one writes the unknowns in the forms

$$u_1^0 = U_1(\underset{\sim}{n} \cdot \underset{\sim}{x}, t), \quad u_2^0 = U_3(\underset{\sim}{n} \cdot \underset{\sim}{x}, t)$$

$$u_2^0 = W(\underset{\sim}{n} \cdot \underset{\sim}{x}, t), \quad u_1^1 = -b\, \Psi_3(\underset{\sim}{n} \cdot \underset{\sim}{x}, t), \quad u_3^1 = b\, \Psi_1(\underset{\sim}{n} \cdot \underset{\sim}{x}, t) \tag{I-7}$$

Note that q is a prescribed function in time, along a line parallel to the normal $\underset{\sim}{n}$. This reduces the differential equations of motion to equations in two variables ζ , t where $\zeta = \underset{\sim}{n} \cdot \underset{\sim}{x}$. The formal solution to this initial value problem is found by taking a Laplace transform on the time variable and a Fourier transform on the space variable. These operations are defined as follows:

$$L[f] = \bar{f}(s) = \int_0^\infty e^{-st} f(t)\, dt$$

$$T[f] = \hat{f}(k) = \int_{-\infty}^{\infty} e^{ik\zeta} f(\zeta)\, d\zeta \tag{I-8}$$

Thus when the displacements have the forms given by (I-7) and the operations (I-8) are performed on the equations of motion, the following algebraic set of equations result, where initial values of μ are assumed to be zero and where $q = 0$ for $t < 0$.

$$\begin{bmatrix} (A_{11} + \rho s^2/k^2) & A_{12}\cos\alpha\sin\alpha \\ A_{12}\cos\alpha\sin\alpha & (A_{22}+\rho s^2/k^2) \end{bmatrix} \begin{bmatrix} \hat{\bar{U}}_1 \\ \hat{\bar{U}}_3 \end{bmatrix} = -\frac{1}{k^2} \begin{bmatrix} -\hat{\bar{q}}_2 ika_1\cos\alpha \\ -\hat{\bar{q}}_2 ika_2\sin\alpha \end{bmatrix} \quad \text{(I-9)}$$

$$\begin{bmatrix} (\hat{C}_{66}k^2+\rho s^2) & -ik\hat{C}_{66}\cos\alpha & ik\hat{C}_{66}\sin\alpha \\ \rho\Omega_0^2 ik\cos\alpha & (A_{11}k^2+\rho\Omega_0^2+\rho s^2) & -k^2A_{12}\cos\alpha\sin\alpha \\ -\rho\Omega_0^2 ik\sin\alpha & -k^2A_{12}\cos\alpha\sin\alpha & (A_{22}k^2+\rho\Omega_0^2+\rho s^2) \end{bmatrix} \begin{bmatrix} W \\ \Psi_3 \\ \Psi_1 \end{bmatrix} = \begin{bmatrix} \hat{\bar{q}}_2/2b \\ \hat{\bar{q}}_2 ka_3\cos\alpha \\ -\hat{\bar{q}}_2 ika_4\sin\alpha \end{bmatrix} \quad \text{(I-10)}$$

where

$$A_{11} = \hat{C}_{11}\cos^2\alpha + C_{55}\sin^2\alpha$$

$$A_{22} = \hat{C}_{33}\sin^2\alpha + C_{55}\cos^2\alpha$$

$$A_{12} = C_{55} + \hat{C}_{13}$$

$$\Omega_0^2 = 3\hat{C}_{66}/b^2\rho$$

Ω_0 is the frequency of the first thickness shear mode from the exact theory. Also,

$$a_1 = C_{12}/2C_{22}\ ,\quad a_2 = C_{23}/2C_{22}\ ,\quad a_3 = C_{12}/2bC_{22}\ ,\quad a_4 = C_{23}/2bC_{22}$$

Inversion of Laplace Transform

When $\underset{\sim}{q}(\zeta,t)$ is given, these equations may be solved in the transformed variables. For example consider the following case.

CASE I.) Midplane Motion; Normal Load ($q_1 = q_3 = 0$)

$$\hat{U}_1 = i\hat{\bar{q}}_2\{(A_{22}+s^2/k^2)a_1 - A_{12}a_2\sin^2\alpha\}\cos\alpha/k\Delta$$

$$\hat{U}_3 = i\hat{\bar{q}}_2\{(A_{11}+s^2/k^2)a_2 - A_{12}a_1\cos^2\alpha\}\sin\alpha/k\Delta \qquad \text{(I-11)}$$

where

$$\Delta = (A_{11} + s^2/k^2)(A_{22} + s^2/k^2) - A_{12}^2\cos^2\alpha\sin^2\alpha$$

These solutions in the transformed plane are thus of the form

$$\hat{U} = i\hat{\bar{q}}_2 P(s^2)/k\Delta(s^2)$$

where $P(s^2)$, $\Delta(s^2)$ are polynomials in s^2 . $\Delta(s^2)$ has four zeros in the complex s plane for each k. The two roots $|s_1/k|$ and $|s_2/k|$ correspond to the two real wave speeds associated with the propagation of plane waves in the plate (ref. 1). In fact, A_{ij} , is simply the two-dimensional acoustic tensor for the plate as discussed in a previous paper. We are thus guaranteed four pure imaginary roots for s

$$s = \pm iv_1 k \quad , \quad \pm iv_2 k$$

The inversion can then be done by use of the convolution theorem; i.e., if

$$G(t) = L^{-1}\left[\frac{P(s^2)}{\Delta(s^2)}\right]$$

then

$$\hat{U}(k,t) = L^{-1}[\hat{\bar{U}}] = \frac{i}{k}\int_0^t \hat{q}_2(k,t-\tau)G(\tau)d\tau \qquad \text{(I-12)}$$

For our case it can easily be shown that

$$G(t) = -\frac{kP(-k^2v_1^2)}{(v_1^2-v_2^2)}\frac{\sin kv_1 t}{v_1} + \frac{kP(-k^2v_2^2)}{(v_1^2-v_2^2)}\frac{\sin kv_2 t}{v_2} \qquad \text{(I-13)}$$

CASE II.) Flexural Motion; Normal Load.

In a similar fashion when q is given, $\hat{\bar{W}}$, $\hat{\bar{\Psi}}_1$ or $\hat{\bar{\Psi}}_3$ can be solved and have the form

$$\hat{\bar{W}} = \hat{\bar{q}} \frac{R(s^2)}{\Delta_1(s^2,k^2)} \tag{I-14}$$

However, in this case the roots of $\Delta_1 = 0$ are not proportional to k. This means that the velocity of wave propagation depends on the wavelength. As $k \to \infty$ it is known that the wave speeds become independent of k and, in fact, two of them equal the non-dispersive wave speeds v_1, v_2 found in the previous example (ref. 1). It is also known from the dispersion relations for plates (ref. 7), that for k real, there will be six pure imaginary roots of $\Delta_1(s^2) = 0$ at

$$s = \pm i\omega_1(k), \quad \pm i\omega_2(k), \quad \pm i\omega_3(k)$$

The relations $\omega_i(k)$ are known as the branches of the dispersion relation for these plates. One branch goes through the origin, i.e.

$$\omega_1(k) \to 0 \quad \text{as} \quad k \to 0$$

The other two branches are sometimes called optical since as the wavelength becomes infinite, i.e. $k \to 0$, ω_2 and ω_3 denote the vibratory frequency of the thickness shear mode for the plate

$$\omega_2(0) = \omega_3(0) = \Omega_0$$

A typical dispersion curve is shown in Figure 2.

The inversion again makes use of the convolution theorem and the residue calculus to invert $1/\Delta_1(s^2)$. Thus we obtain

$$\hat{W}(k,t) = \int_0^t \hat{q}(k,t-\tau)H(\tau)d\tau$$

$$H(t) = \frac{R(\omega_1)}{(\omega_2^2-\omega_1^2)(\omega_3^2-\omega_1^2)} \frac{\sin\omega_1 t}{\omega_1} + \frac{R(\omega_2)}{(\omega_1^2-\omega_2^2)(\omega_3^2-\omega_2^2)} \frac{\sin\omega_2 t}{\omega_2} + \frac{R(\omega_3)}{(\omega_1^2-\omega_3^2)(\omega_2^2-\omega_3^2)} \frac{\sin\omega_3 t}{\omega_3} \qquad \text{(I-15)}$$

Numerical Inversion of the Fourier Transform

It is at this juncture that the solutions to most problems in transient wave propagation are limited by analytic skill in extracting information from the inversion. In a few cases the complete solution can be given, while in most, far field, near field, short and long time approximations must be invoked. The numerical inversion of the transform has until recent years been limited by the calculation of an integral for each point in the space ζ. However, recently a technique has been developed which obviates the need for a separate inversion for each point in the real space ζ. Known as the "Fast Fourier Transform" (ref. 8), it takes a sampling matrix of the transform of U, say $(\hat{U}(k_1), \hat{U}(k_2), \ldots \hat{U}(k_N))$ and returns a sampling matrix of the original function

$$(U(\zeta_1), U(\zeta_2), U(\zeta_3), \ldots U(\zeta_N))$$

For a large enough N, one will obtain a picture of the original function $U(\zeta)$. Application of this algorithm to our problem is described below.

The specific operation that these computational algorithms perform is called a finite, discrete Fourier transform. Thus if $D(I)$ is a one x N matrix of data, the output of the algorithm $T(J)$ is given by

$$T(J) = \sum_{I=1}^{N} D(I) e^{\frac{-2\pi i (I-1)(J-1)}{N}} \tag{I-16}$$

The properties of this operator are similar to the conventional Fourier operators in the space of continuous variables (ref. 8). The sum is not performed in a direct manner on the computer but in a manner which reduces the number of arithmetic steps and makes the operation attractive as a computational tool.

In the solution of partial differential equations by Fourier transforms we are led to evaluate integrals of the type

$$U(\zeta) = \frac{1}{2\pi} \int_{-\infty}^{\infty} \hat{U}(k) e^{-ik\zeta} dk$$

If significant changes in $U(\zeta)$ occur over distances greater than λ, then the largest wave number of interest will be

$$\kappa = 2\pi/\lambda$$

Thus we may be satisfied with an approximation to $U(\zeta)$ of the form

$$\tilde{U}(\zeta) = \frac{1}{2\pi} \int_{-\kappa}^{\kappa} \hat{U}(k) e^{-ik\zeta} dk$$

or shifting the coordinates

$$\tilde{U} = \frac{e^{i\kappa\zeta}}{2\pi} \int_0^{2\kappa} \hat{U}(k-\kappa)e^{-ik\zeta}dk$$

This latter integral may further be approximated by the limit of a sum

$$\tilde{U} = \frac{\kappa}{\pi N} e^{i\kappa\zeta} \Sigma \hat{U}(k_I-\kappa)e^{-ik_I\zeta} \qquad \text{(I-17)}$$

where

$$k_I = \frac{2\kappa}{N}\left(\frac{1}{2} + (I-1)\right) = \frac{4\pi}{N\lambda}\left(\frac{1}{2} + (I-1)\right)$$

or

$$\tilde{U} = \frac{\kappa}{\pi N} e^{i\kappa\zeta(1-\frac{1}{N})} \sum_{I=1}^{N} \hat{U}(k_I-\kappa)\, e^{-\frac{i2\pi(I-1)}{N}\frac{2\zeta}{\lambda}}$$

So far $\tilde{U}(\zeta)$ has remained a continuous function of ζ. However at the points

$$\zeta_J = \frac{\lambda}{2}(J-1) \quad , \quad J = 1, 2, .. N$$

the summation becomes identical to the finite descrete Fourier transform

$$\tilde{U}(\zeta_J) = \tilde{U}(J) = e^{\frac{i\pi(J-1)(N-1)}{N}} \frac{\kappa}{\pi N} T(J) \qquad \text{(I-18)}$$

where $T(J)$ is defined in (I-16) and

$$D(I) = \hat{U}(k_I - \kappa)$$

Note that this scheme gives details of $U(\zeta)$ of distance no smaller than $\lambda/2$. This was implicit in choosing maximum wave number. Further when N is even, the output matrix $\tilde{U}(J)$ describes the function only up to $\zeta = \frac{\lambda}{2}(\frac{N}{2} - 1)$. When $\tilde{U}(k_I - \kappa)$ is real, and N even, we have the identities

$$\tilde{U}\ (\tfrac{N}{2} + 1) = 0 \quad , \quad \text{Imag}(\tilde{U}(J)) = 0$$

$$U(\tfrac{N}{2} + 1 + \kappa) = -\tilde{U}(\tfrac{N}{2} + 1 - \kappa)$$

Thus the one-dimensional output matrix $\tilde{U}(J)$ which approximates our original function is antisymmetric about $J = \frac{N}{2} + 1$ and symmetric about $J = 1$. Since $\tilde{U}(J) = 0$ for $J = 1 + N/2$ we must choose N large enough, or the time small enough to ensure that our wave has not reached $\zeta = \lambda(N + 2)/4$. In this approximation, we have effectively replaced a single impact source by

an infinite periodic array of sources and negative sources. Our approximation will be valid as long as the waves from each of these sources do not interact with each other.

Notes on the Numerical Fourier Inversion

There were several checks made of the fast Fourier computer routine (ref. 8) used in this paper. First, known functions were transformed analytically and inverted numerically. The results of these tests revealed that the inversion program works best on continuous functions if one is to avoid spurious oscillations near points of discontinuity.

Second, the initial value problem for a nondispersive medium such as a string was programmed. The results of this test are shown in Figure 3a. The shape of the string at the initial time and subsequent times as predicted by the computer preserve the original triangular shape and exhibit the wave shift at the proper speed.

Lastly the impact of a string was programmed using the same force applied to the plate problem. The theoretical result predicts a constant displacement behind the wave front as shown in Figure 3b.

For the line impact of an anisotropic Mindlin plate, a specific load distribution was chosen for ease of analytical calculation of the Fourier transform and Laplace convolution integral;

$$\text{for} \quad |\zeta| < a \quad \text{and} \quad t < \tau_o$$

$$q_2 = -P_o \frac{1}{2}\left(1 + \cos\frac{\pi\zeta}{a}\right) \sin\frac{\pi t}{\tau_o} \tag{I-19}$$

$$\text{for} \quad |\zeta| > a \quad \text{or} \quad t > \tau_o$$

$$q_2 = 0$$

By using the fast Fourier transform (with a proper sign change) one could find the transform for an arbitrary load distribution. However, this has not been done. Nor has the author used the load distribution for a Hertz contact problem, as might be supposed in an impact problem (reasons for this will be given below). However the chosen distribution, it is hoped, will exhibit most of the salient effects of the impact of a plate.

While ad hoc, the particular choice of the load distribution is not entirely arbitrary. Continuity of the first and second derivatives (as the function (I-19) exhibits) is dictated by a desire to have all stresses continuous (i.e. to avoid shocks) and thus spurious oscillations in the numerical inversion. This stems from the fact that in the Mindlin theory the midplane stresses, having as wave sources the term ∇q_2 , have the following form for their transforms

$$\hat{t}_{\alpha\beta} \sim \int_0^t k\hat{q}_2(k,\tau)\ \text{sin}kv(t-\tau)d\tau\ , \quad (\alpha,\beta = 1,3)$$

where v denotes either the first or second wave speed. Thus when $\hat{q}_2$ has the form

$$\hat{q}_2 = \hat{Q}(k)\delta(\tau)$$

the stresses are proportional to

$$\hat{t}_{\alpha\beta} \sim k\ \hat{Q}(k)\ \text{sin}kvt \sim T\left[\frac{\partial^2 Q}{\partial \zeta^2}\right]\ T\ [F(vt-\zeta)]$$

where,

$$F(vt-\zeta) = 1, \quad |\zeta| < vt$$
$$= 0 \quad |\zeta| < vt$$

Thus for continuous stresses at early times after the wave arrival, the spacial part of q_2 must have continuous second derivatives, which led to the choice of (I-19). This conclusion was found also in the numerical results when non-smooth load distributions were used.

Results for the Line Impact Problem

Using the transient load distribution described above, calculations were made, on an IBM 360-91 computer, of the stresses and displacements in both a classical and Mindlin plate due to impact type loading. The results are shown in Figures 4-8.

One of the important parameters in this problem is the ratio of load extent to plate half thickness, a/b. When a/b is of order unity or less, one would expect that shear effects would become important and the Mindlin and classical plate solutions would differ. This is so, as shown in Figure 4 for the case of $a/b = 1$. However in Figure 5 when $a/b = 10$ the displacements calculated by both Mindlin and classical theories do not differ by very much.

The remaining figures are for the Mindlin plate and were calculated for the composite, 55% graphite fiber-epoxy matrix, using equivalent elastic constants for various layup angles of the fibers. The constants were taken from Chamis (ref. 9).

In Figure 6 we have plotted the center plate displacement versus time for both the classical and Mindlin theories. For the classical plate this function can be found explicitly. The displacement increases as the square root of time when the impact force is a delta function

in time and space. This result is confirmed by the numerical results in Figure 6 and is also the case for the Mindlin plate for large time. (Note that for a string, the displacement at the center is time independent after impact.)

The effect of layup angle on the plate response is shown in Figure 7, for various times after impact. As can be seen, the displacement is somewhat insensitive to layup angles of up to about $\pm 15^{o}$ for either line loads along the x_3 axis or along the x_1 axis.

Finally in Figure 8 the induced membrane or average in-plane stress $1/2(t_{11} + t_{33})$ is shown for various layup angles at a time immediately after the impact time. One can see that the initial compression pulses are preceeded by wave fronts which vary in magnitude and velocity with layup angle. Also for a wave propagating along the x_1 axis (load on the x_3 axis), the $\pm 45^{o}$ layup results in higher stresses than for other layup angles. While the flexural stresses are higher than the membrane stresses, the membrane stresses will propagate ahead of the bending waves and will have a tension pulse in the signal which might cause splitting through the plate or plys as have been observed in experiments.

In the case of one-dimensional wave propagation in a direction $n = [\cos\alpha, \sin\alpha]$,, the direction of the displacement is not parallel to n but is known for the particular wave in question. The direction

of displacement for the first two in-plane waves was given in Figure 6 of Ref. 1

$$[u_1^0, u_3^0] = U(\underset{\sim}{n}\cdot\underset{\sim}{x}-vt)[\cos\beta, \sin\beta]$$

From (I-5), the stress may be determined. In particular, the average in-plane stresses t_{11}^o, t_{33}^o, t_{13}^o can be found as functions of the mean stress $\sigma \equiv 1/2(t_{11}^o + t_{33}^o)$;

$$t_{11}^0 = 2\sigma(\hat{C}_{11}\cos\alpha\cos\beta + \hat{C}_{13}\sin\alpha\sin\beta)/D$$

$$t_{33}^0 = 2\sigma(\hat{C}_{33}\sin\alpha\sin\beta + \hat{C}_{13}\cos\alpha\cos\beta)/D$$

$$t_{13}^0 = 2\sigma C_{55}(\cos\beta\sin\alpha + \cos\alpha\sin\beta)/D$$

where

$$D = (\hat{C}_{11}+\hat{C}_{13})\cos\alpha\cos\beta + (\hat{C}_{33}+\hat{C}_{13})\sin\alpha\sin\beta$$

SECTION II: STRESS WAVES DUE TO CENTRAL IMPACT OF ANISOTROPIC PLATES

In Section I of this report, an analytical-computational method was described for the calculation of the impact induced stresses behind the wave front. The method was checked for known, one-dimensional problems such as the impact of a string, and the line impact of a classical anistotropic plate. The induced stresses were given in terms of the impact pressure. However, no prediction was made of the maximum impact pressure in terms of the velocity and mass of the impacting body.

In this part of the report, the problem of normal or central impact is discussed. Two-dimensional stress patterns are presented in terms of the impact pressure and an estimate is made of its magnitude for a spherical impacting body of known velocity and mass.

Description of the Mathematical Model

Before discussing the results, a discussion of the assumptions made in the model will be given. In practice, fiber composite plates are made

up of a number of unidirectional plys oriented at various angles to obtain certain desired properties. When the properties and lay up angles of each ply are known, one can obtain the plate constants by averaging across the thickness. These average elastic constants represent an equivalent anisotropic-homogeneous material. In the present work the laminated plate is replaced by an equivalent anisotropic plate. The equivalent elastic constants were obtained from a computer code developed by Chamis (ref. 9). The following additional assumptions are implicit in this model.

Linear Elastic Properties

This model is based on linear elasticity. Thus, plastic, viscoelastic, and fracture effects are not taken into account. The results of these effects is to decrease the amount of wave energy that can propagate into the plate. Thus, the elastic analysis represents an upper bound on the actual stresses during impact. The effect of initial stress in the plate has also not been considered in this report.

Boundaries and Tapering

Another limitation of this work is the neglect of the effect of boundaries or edges of the composite fan blade. The reflections from boundaries can of course be handled with the linear elastic theory. However, if one is interested in the maximum stresses, these should occur near or at the impact point except for the case of edge or near edge impact. Also, for small impact times, the waves behave as if the finite plate were infinite. The case of edge impact is under study at this writing.

In this report the plate thickness is assumed to be constant, while

in a fan blade taper and twist will be present. The neglect of these effects seem to be of lesser importance than those due to inelasticity and boundaries.

Thickness Reflections and the Mindlin Theory

The use of an equivalent anisotropic plate neglects the reflections of waves at the ply boundaries. However, this approximation will be valid for wavelengths* greater than the ply thickness, and valid also for wavelengths greater than the plate thickness. There are analyses which consider wave-ply interactions, (Ref. 10), but in general the change in stress must occur over distances comparable to ply or fiber thickness for these effects to become important.

In the Mindlin theory of plates, the wave reflections are averaged through the thickness. (ref. 7). In dynamic loading of a plate, the stresses will propagate through the plate thickness as well as away from the impact point. These waves will suffer many reflections as they propagate back and forth between the plate surfaces. The calculations of these many reflections for a three-dimensional plate thus become impossible for anything but very early times after impact. The Mindlin plate theory thus restricts the mathematical equations to a description of the average plate midplane motion and rotations.

In the Mindlin theory used in this report the plate displacements $u = (u_1, u_2, u_3,)$ (See Fig. 9) have the form (See Ref. 1)

*An effective wavelength can be defined as the contact time of impact multiplied by the smallest wave velocity in the material.

$$\underset{\sim}{u} = \underset{\sim}{u}^{\circ}(x_1,x_3,t) + \frac{x_2}{b}\,\underset{\sim}{u}^{(1)}(x_1,x_3,t) + \frac{1}{2}[3(\frac{x_2}{b})^2-1]\,\underset{\sim}{u}^{(2)}(x_1,x_3,t) \qquad \text{(II-1)}$$

The equations governing the motion are listed below. The first two equations are for the inplane displacements u_1°,u_3° and the next three govern the transverse displacement u_2° and flexural rotations u_1^1/b , u_3^1/b . The transverse impact loading is represented by $-q_2(x_1,x_3,t)$ which we will prescribe in the following section.

$$\rho\frac{\partial^2 u_1^0}{\partial t^2} = \hat{C}_{11}\frac{\partial^2 u_1^0}{\partial x_1^2} + C_{55}\frac{\partial^2 u_1^0}{\partial x_3^2} + (C_{55}+\hat{C}_{13})\frac{\partial^2 u_3^0}{\partial x_1\,\partial x_3} + \frac{C_{12}}{2C_{22}}\frac{\partial q_2}{\partial x_1}$$

$$\rho\frac{\partial^2 u_3^0}{\partial t^2} = \hat{C}_{33}\frac{\partial^2 u_3^0}{\partial x_3^2} + C_{55}\frac{\partial^2 u_3^0}{\partial x_1^2} + (C_{55}+\hat{C}_{13})\frac{\partial^2 u_1^0}{\partial x_1\,\partial x_3} + \frac{C_{23}}{2C_{22}}\frac{\partial q_2}{\partial x_3} \qquad \text{(II-2)}$$

$$\rho\frac{\partial^2 u_2^0}{\partial t^2} = C_{66}\frac{\partial^2 u_2^0}{\partial x_1^2} + C_{44}\frac{\partial^2 u_2^0}{\partial x_3^2} + C_{66}\frac{1}{b}\frac{\partial u_1^1}{\partial x_1} + C_{44}\frac{1}{b}\frac{\partial u_3^1}{\partial x_3} + \frac{1}{2b}q_2$$

$$\rho\frac{\partial^2 u_1^1}{\partial t^2} = \hat{C}_{11}\frac{\partial^2 u_1^1}{\partial x_1^2} + C_{55}\frac{\partial^2 u_1^1}{\partial x_3^2} + (C_{55}+\hat{C}_{13})\frac{\partial^2 u_3^1}{\partial x_1\,\partial x_3} - \frac{3}{b}C_{66}\left(\frac{\partial u_1^0}{\partial x_1} + \frac{u_1^1}{b}\right) + \frac{C_{12}}{2C_{22}}\frac{\partial q_2}{\partial x_1} \qquad \text{(II-3)}$$

$$\rho\frac{\partial^2 u_3^1}{\partial t^2} = \hat{C}_{33}\frac{\partial^2 u_3^1}{\partial x_3^2} + C_{55}\frac{\partial^2 u_3^1}{\partial x_1^2} + (C_{55}+\hat{C}_{13})\frac{\partial^2 u_1^1}{\partial x_1\,\partial x_3} - \frac{3}{b}C_{44}\left(\frac{\partial u_2^0}{\partial x_3} + \frac{u_3^1}{b}\right) + \frac{C_{23}}{2C_{22}}\frac{\partial q_2}{\partial x_3}$$

where

$$\hat{C}_{11} = C_{11} - \frac{C_{12}^2}{C_{22}}$$

$$\hat{C}_{33} = C_{33} - \frac{C_{32}^2}{C_{22}}$$

$$\hat{C}_{13} = C_{13} - \frac{C_{12}\,C_{23}}{C_{22}} \quad , \quad \hat{C}_{66} = \kappa C_{66}$$

The factor κ is a correction factor introduced by Mindlin and equal to $\kappa = \pi^2/12$

If the plate is struck at a point, the energy will propagate into the composite in the form of elastic waves (see Ref. 1). Two of these waves will have anisotropic wave fronts and will depend on the fiber layup angle of the composite as shown in Figure 10. The average in-plane stresses across the thickness will propagate in this manner. The flexural energy will propagate behind a slower isotropic wave front.

The stresses in the plate are given in terms of the displacement (Section I of this report). The mathematical problem to be solved consists of the following: find a solution to the coupled partial differential equations (II-2), (II-3) when the loading function q_2 is a prescribed function of the plate coordinates x_1, x_3 and time, and the plate is initially at rest.

The solution of this problem was accomplished using a combination

analytical and computational technique involving Laplace and Fourier transforms. Details of finding the solution are discussed in Appendix A of this report. Results of these calculations are discussed below.

Before considering the results, we must discuss the choice of the impact loading function q_2 .

To determine the maximum contact pressure one must know the impact pressure distribution on the plate surface. In the static Hertz theory, this pressure is given by (see Ref. 11 and 12)

$$q_2 = -P_0(1 - (\frac{r}{a})^2)^{1/2} \qquad \text{(II-4)}$$

This distribution is not suitable for our theory since the infinite slope of $P(r)$, at $r = a$, would appear in our approximate equations (II-2) and (II-3) as a source term. In fact, it is shown in Section I of this report that the second derivative of $P(r)$ must be finite at $r = a$ for the stresses to be continuous. To resolve this problem, an ad hoc pressure distribution is assumed which produces finite stresses;

$$\begin{aligned} q_2 &= -P_0(1 - 2(\tfrac{r}{a})^2 + (\tfrac{r}{a})^4)f(t); \; r \leq a \\ q_2 &= 0 , \quad r > a \\ f(t) &= \sin \pi t/\tau , \quad t \leq \tau , \; f(t) = 0 \quad t > \tau \end{aligned} \qquad \text{(II-5)}$$

It should be noted that in an actual impact, the impact area changes with time. This effect is difficult to model in the analytical part of the problem. Instead we have chosen to prescribe a time varying pressure over the maximum contact area.

The total force produced by such a pressure distribution is

$$F_0 = 2\pi \int_0^a q(r)\, r\, dr$$

$$F_0 = \frac{\pi a^2 P_0}{3} \qquad \text{(II-6)}$$

Using (9) we may calculate the total impulse to be

$$I = \int_0^\tau F_0 \sin\frac{\pi t}{\tau}\, dt = \frac{2}{3} a^2 P_0 \tau \qquad \text{(II-7)}$$

If the rebound velocity is V_1, and the inital velocity V_0, the impulse given by

$$I = M(V_1 + V_0) \qquad \text{(II-8)}$$

Herztian Impact Stress

In order to determine the impact stress equations (II-2, 3), the impact pressure distribution must be found in terms of the object mass, velocity, geometry and elastic properties. No exact solutions to this dynamic problem are known in the theory of elasticity. However the static theory of contact of elastic isotropic bodies is known and was developed by Hertz (ref. 11). It is known, however, that even under small contact forces the contact pressure exceeds the elastic limit of conventional materials (see e.g. Goldsmith, (ref. 12)). One would expect then that for high speed impact (>100 m/sec.) the local contact

stresses would exceed the elastic limit of most materials. In spite of this violation of the elastic assumption of the Hertz theory of impact, experiments have shown that the impact times predicted by the elastic theory agree reasonably well with data from impact tests. The stresses predicted by this theory however are upper bounds on the actual stresses. Also if the surface of impact belongs to a structure which can move, then the contact times predicted by this theory are lower bounds on the actual time of contact of object and structural surface. With these restrictions in mind the Hertz theory of impact will be reviewed as it can be adapted to composite materials.

Consider the contact of a sphere of radius R and elastic half space. The contact force between the two bodies F, is related to the relative approach of the bodies α, and has the dependence

$$F = k_2 \alpha^{3/2} \tag{II-9}$$

where k_2 is a constant dependent on the properties of the bodies. When both bodies are isotropic this constant is given by

$$k_2 = \frac{4}{3} R^{1/2} \left[\frac{1-\nu_1^2}{E_1} + \frac{1-\nu_2^2}{E_2} \right]^{-1} \tag{II-10}$$

where ν, E are Poisson's ratio and Young's modulus respectively for each body.

Composite materials however are anisotropic in general. The

corresponding problem for the contact of anisotropic bodies has recently been given by Willis (ref. 13). For this case the contact area is an ellipse, the dimensions of which must be determined from algebraic equations. The shape of this ellipse for typical composite anisotropy has not been determined, though from experiments of the author on graphite/epoxy and boron/aluminum composites seem to show that the contact area is close to a circle. It is assumed then that for the impact of an isotropic sphere with a composite surface the contact area is a circle. Also the constant k_2 is replaced by

$$k_2 = \frac{4}{3} R^{1/2} \left[\frac{1-\nu_1^2}{E_1} + \frac{1}{C_{22}} \right]^{-1} \qquad \text{(II-11)}$$

where E_1, ν_1 are the elastic constants of the sphere, and C_{22} is the elastic modulus of the composite plate. This assumption of course is just an educated guess.

In the Hertz impact theory the force (II-9), which was determined from a static solution, is used in Newtons law for the sphere

$$M \frac{dV}{dt} = - k_2 \alpha^{3/2} \qquad \text{(II-12)}$$

where M is the mass of the sphere and V the instantaneous velocity of the sphere.

This assumption is only valid when the contact time is much greater than the time for elastic waves in the sphere to traverse the object.

Further when the motion of the plate becomes large during the contact interval, (II-12) must be replaced by

$$M \frac{d^2U}{dt^2} = k(U-W)^{3/2} \tag{II-13}$$

where U is the displacement of the sphere and W is the displacement of the plate at the point of contact. This problem requires simultaneous determination of the motion of the sphere and plate. This has not been done in this report but work on this problem is in progress.

When $W \tilde{=} 0$ during the contact period, the time of contact can be shown to be (see e.g., Goldsmith (ref. 12))

$$\tau = 2 \int_0^{\alpha_1} \frac{d\alpha}{\left[V^2 - \frac{k_2}{M} \alpha^{5/2}\right]^{1/2}} = \frac{2.943\ \alpha_1}{V} \tag{II-14}$$

where α_1 is the maximum approach of the impacting object. This value is given by

$$\alpha_1 = \left(\frac{5}{4} \frac{MV^2}{k_2}\right)^{2/5} \tag{II-15}$$

For elastic impact the maximum radius of contact is given by

$$a = \sqrt{\alpha_1 R} \tag{II-16}$$

The impact force in this theory as determined from the solution of (II-12) is given by

$$F = F_0 \sin \pi t/\tau \quad , t \leq \tau$$
$$= 0 \quad , t > \tau \qquad \text{(II-17)}$$

where $F_0 = 3.36 \frac{MV}{\tau}$. The pressure distribution in this theory is given by the expression

$$P = P_0 \left(1 - \left(\frac{r}{a}\right)^2\right)^{1/2}$$

where $P_0 = \frac{3}{2} F_0/\pi a^2$. It is interesting to note that the impact pressure P_0, is independent of the radius of the impacting object. This distribution, however, is determined from a static elasticity solution and should not be expected to hold under dynamic impact. Of course the contact radius varies with time reaching a maximum value (II-4) at half the period.

Another limitation of the theory is the fact that it predicts a rebound velocity equal to the initial velocity V_0. In an actual impact, momentum would be transmitted to the structure, thus changing rebound velocity to something less than V_0. Solution of the coupled problem (II-13) should enable a better determinatinn of the rebound velocity.

A further improvement of the theory might be achieved if a more general contact law is used, say (called the Meyer Law, see (ref. 12))

$$F = k \alpha^n$$

where n, k, would be determined from static experiments on composite materials. This approach is presently under investigation.

Well aware of the long list of limitations on the above model for impact, we have nonetheless used the above procedure to obtain estimates of the impact time, contact force, and maximum contact pressure for different impacting bodies and speeds. The results of these calculations are shown in Figures 11 and 12 where data is presented for spherical ice particles and for granite-like stones.

For impact speeds from 100 to 500 meters/sec. and 1/2 to 2 cm. diameter granite spheres, the contact times range from 15 to 85 μsec.

In summary, these impact formuli reveal the following dependence on impact velocity:

$$\tau \sim 1/V^{1/5}, \quad P_0 \sim V^{2/5}$$

These results should only be used as guidelines, since many assumptions are made which break down at high velocities.

Goldsmith and Lyman (ref. 14) have shown the Hertz theory to be remarkably valid insofar as contact time and peak pressure are concerned for the impact of hard steel spheres (1/2" diameter) into a hard steel surface for velocities up to 300 ft./sec. (91.5 meters/sec.). The calculations in this report based on the Hertz law of impact extend well beyond this limit (100-500 meters/sec.). Thus the contact times and maximum impact pressures presented in Figures 11, 12 for graphite/epoxy can only be used as rough guides for which the values for contact times are lower bounds on the actual times and the values for pressure are upper bounds.

One further reason why the Hertz law is not valid is that for velocities in the range of 100 to 500 meters/sec., the contact area diameter approaches the diameter of the striking object, which certainly violates one of the assumptions in the Hertz theory.

At the writing of this report, work is in progress on using a proper Hertz contact theory for anisotropic materials. However, for large deformations, plates, and fracture effects in the impact zone, a more detailed analysis of the impact zone is needed than is given in this report.

Results for Impact Stresses

Solutions to equations (II-2, II-3), which govern the central impact of anisotropic plates, were found for impact-like pressures using an analytical/computational method as described in Appendix A of this report. In this model there are eight different stresses (see Section I) associated with the membrane, flexural and interlaminar stresses. The presentation of all of these stresses for different times after impact and various layup angles becomes an enormous task. Instead certain key stresses or stress measures are presented in this report to give an overall view of the stress picture.

The three stress measures chosen for this report were the average membrane stress $(t^0_{11} + t^0_{33})/2$, the average flexural stress $(t^1_{11} + t^1_{33})/2$ at the surface of the plate, and the maximum interlaminar shear stress given by $(t^2_{21} + t^2_{23})^{1/2}$. These stresses are not necessarily the maximum stresses at a point, but they are independent of the orientation

about an axis normal to the plate. The program also allows individual stresses to be obtained if desired.

The stresses were calculated in a quarter plane of the plate for a specific time after the initiation of impact and were normalized with respect to the maximum impact pressure as calculated in the above section. The data is presented for various times and layup angles in the form of stress contour plots (Fig. 14-25) which were made on a "Calcomp" plotter at the NASA Lewis Research Center, (ref. 16). Superimposed on these curves are the theoretical wave front for the particular wave in question and the radius of the circle which bounds the impact pressure. The wave front calculations were based on the work and represent a locus of wave surfaces originating from the edge of the impact circle for a given time after start of impact.

These results show the effect of the change of fiber layup angles on the stress distributions. In general, the maximum stresses tend to lie along the fiber directions. For most of the cases treated, the significant stressed region revealed by the calculations is bounded by the theoretical wave fronts as calculated in (ref. 1). This provides a check on the accuracy of the approximations made in the numerical computation scheme.

For this elastic model, the maximum mean stresses $\frac{1}{2}(t_{11} + t_{33})$ occur at about the end of the impact time. The question about an optimum fiber layup angle is partially answered by the data in Fig. 33. For the flexural stresses, the optimum layup angle is about $\pm 15^{\circ}$ showing a 34% lower mean stress level than the $\pm 45^{\circ}$ case. However, regarding the interlaminar stresses, for the same impact conditions, there seems to be little difference in the maximum stress level with layup angle despite significant changes in stress distribution in space with layup angle.

For the average membrane mean stress $t^{0}_{11} + t^{0}_{33}$, immediately after impact, the lower layup angle plates yield lower maximum stresses. However, at later times, the $\pm 45^{\circ}$ layup case appears to give a lower maximum stress in the plate.

Another result of these calculations is that the induced stresses depend on the impact circle radius-to-plate-thickness ratio (a/2b). On the other hand, the impact circle depends on the incoming particle velocity as determined by equation (8). Thus, for each impact velocity, a different impact radius/thickness ratio must be chosen as well as a different contact time. The integration of these two programs has not been performed at this time but will be attempted in the near future.

Of course, to evaluate the possibility of fracture or failure of the composite under impact, the complete stress matrix at a point must be known, as well as the failure criteria, which will itself be anisotropic (ref. 8). The integration of programs described in this section into a computer code suitable for use for pre-design engineering calculations is to be the next phase of this report.

CONCLUSIONS

The successful application of composite materials to jet engine fan blades depends, in part, on the ability of these materials to retain structural integrity under transient loadings due to bird strikes or hailstone impact or other foreign object encounter. While there are a number of experimental investigations connected with this problem, theoretical understanding of impact response and damage is lacking. Such understanding might enable a reduction in costly empirical studies and testing. This report presents the first of a series of analytical models to attempt to understand impact mechanics of composite plates.

Using the method of stress wave analysis, the stresses induced during and after impact with a line load and central impact have been determined. The model has been put into a computer program where the transverse loading force on the composite plate is arbitrary. For central impact the results indicate that the energy propagates into the plate in the form of extensional and flexural waves. At several impact circle diameters from the center, the highest stresses propagate along the fiber directions. The speed of propagation varies with the direction in the plane of the plate.

It has been determined that for composites similar to graphite/epoxy, there is an optimum layup angle near $\pm 15^{\circ}$ for which the flexural stresses are minimized. The maximum stress in a plate without edges, due to central transverse impact, occurs at the end of the contact time.

Using a modified Hertz contact theory, an estimate of the contact times, pressures and forces for various impact velocities and sizes of ice and granite spheres has been calculated. However, the effect of the plate motion has been neglected, which might increase the calculated contact time.

The next parameters to study in this program are the effect of edges on impact, and the effect of plate motion on the contact time and pressures. Also the validity of the Hertz theory is in question for the impact velocity range of interest. A modified Hertz theory or a fluid-solid interaction model should be developed. Some of these effects will be investigated in a continuing study of impact and stress waves in composite fan blades.

REFERENCES

1. Moon, F. C., "Wave Surfaces Due to Impact on Anisotropic Plates," Journal of Composite Materials, Vol. 6, 1972, p. 62.

2. Cooley, J. W. and Tukey, J. W., "An Algorithm for the Machine Calculation of Complex Fourier Series," Mathematics of Computation, Vol. 19, No. 90, April 1965, pp. 297-301.

3. Tauchert, T. R. and Moon, F. C., "Propagation of Stress Waves in Fiber-Reinforced Composite Rods," AIAA/ASME 11th Structures, Structural Dynamics and Materials Conference, Denver, Colorado, 1970.

4. Tauchert, T. R. and Guzelsu, A. N., "An Experimental Study of Dispersion of Stress Waves in a Fiber-Reinforced Composite," Journal of Applied Mechanics, Vol. 39, 1972, p. 98.

5. Sun, C-T., Achenbach, J. D. and Herrmann, G., "Continuum Theory for a Laminated Medium," Journal of Applied Mechanics, Vol. 35, 1968, p. 467.

6. Moon, F. C., "Wave Propagation and Impact in Composite Materials," to appear as a chapter in Treatise on Composite Materials, Ed. Broutman, Krock, Academic Press.

7. Mindlin, R. D., "High Frequency Vibrations of Crystal Plates," Quarterly of Applied Mathematics, Vol. 19, 1961, p. 51.

8. Brenner, N. M., "Three Fortran Programs that Perform the Cooley-Tukey Fourier Transform," Massachusetts Institute of Technology, Lincoln Laboratory Technical Note 1967-2, July 1967.

9. Chamis, C. C., "Computer Code for the Analysis of Multilayered Fiber Composites," Users Manual NASA TN D-7013, 1971.

10. Hutchinson, J. R., "Stress Waves in Layered Materials," AIAA Journal, Vol. 7, No. 4,

11. Hertz, H., "Uber die Beruhrung fester elastischer Körper," Journal Reine Angew Math (Crelle), Vol. 92, 1881, p. 155.

12. Goldsmith, W., Impact. E. Arnold Ltd. (Publishers) 1960, Chapter IV.

13. Willis, J. R., "Hertzian Contact of Anisotropic Bodies," Journal of Mechanics of Physical Solids, Vol. 14, 1966, pp. 163-176.

14. Goldsmith, W. and Lyman, P. T., "The Penetration of Hard Steel Spheres into Plane Metal Surface," Journal of Applied Mechanics, December 1970, pp. 717-725.

15. Chamis, C. C., "Failure Criteria for Filamentary Composites," NASA TN D-5367, Lewis Research Laboratory, August 1967.

16. Canright, R. B. and Swigert, P., "PLOT3D - A Package of Fortran Subprograms to Draw Three-Dimensional Surfaces," NASA Technical Memorandum TM X-1598, Lewis Research Center, June 1968.

LIST OF FIGURES

15 Average Membrane Stress Contours $(t_{11}+t_{33})/2$ for Graphite Fiber-Epoxy Matrix, After Impact for 15^{o} Fiber Layup Angle, Normalized Time $t=2\tau$

16 Average Membrane Stress Contours $(t_{11}+t_{33})/2$ for Graphite Fiber-Epoxy Matrix, After Impact for 30^{o} Fiber Layup Angle, Normalized Time $t=2\tau$

17 Average Membrane Stress Contours $(t_{11}+t_{33})/2$ for Graphite Fiber-Epoxy Matrix, After Impact for 45^{o} Fiber Layup Angle, Normalized Time $t=\tau$

18 Average Membrane Stress Contours $(t_{11}+t_{33})/2$ for Graphite Fiber-Epoxy Matrix, After Impact for 45^{o} Fiber Layup Angle, Normalized Time $t=3\tau$

19 Average Membrane Stress Contours $(t_{11}+t_{33})/2$ for Graphite Fiber-Epoxy Matrix, After Impact for 45^{o} Fiber Layup Angle, Normalized Time $t=2\tau$

20 Average Flexural Stress Contours $(t_{11}+t_{33})/2$ for Graphite Fiber-Epoxy Matrix, After Impact for 15^{o} Layup Angle, Thickness/Impact Diameter Ratio 10.0

21 Average Flexural Stress Contours $(t_{11}+t_{33})/2$ for Graphite Fiber-Epoxy Matrix, After Impact for 30^{o} Layup Angle, Thickness/Impact Diameter Ratio 10.0

22 Average Flexural Stress Contours $(t_{11}+t_{33})/2$ for Graphite Fiber-Epoxy Matrix, After Impact for 45^{o} Layup Angle, Thickness/Impact Diameter Ratio 10.0

23 Average Flexural Stress Contours $(t_{11}+t_{33})/2$ for Graphite Fiber-Epoxy Matrix, After Impact for 30^{o}, 45^{o} Layup Angles, Thickness/Impact Diameter Ratio = 10.0

24 Maximum Interlaminar Shear Contours for Graphite Fiber-Epoxy Matrix After Impact for $\pm 30^{o}$ Fiber Layup Angle, Thickness/Impact Radius Ratio = 10.0

25 Maximum Interlaminar Shear Contours for Graphite Fiber-Epoxy Matrix After Impact for $\pm 45^{o}$ Fiber Layup Angle, Thickness/Impact Radius Ratio = 10.0

26 Midplane Transverse Displacement Distribution in the Quarter Plane of the Plate for Graphite Fiber-Epoxy Matrix After Impact for $\pm 45^{\circ}$ Fiber Layup Angle, Thickness/Impact Radius Ratio = 1.0

27 Midplane Transverse Displacement Distribution in the Quarter Plane of the Plate for Graphite Fiber-Epoxy Matrix After Impact for $\pm 45^{\circ}$ Fiber Layup Angle, Thickness/Impact Radius Ratio = 1.0

28 Average Membrane Stress Distribution in the Quarter Plane of the Plate for Graphite Fiber-Epoxy Matrix After Impact for 0° Layup Angle

29 Average Membrane Stress Distribution in the Quarter Plane of the Plate for Graphite Fiber-Epoxy Matrix After Impact for $\pm 45^{\circ}$ Layup Angle

30 Average Flexural Stress Distribution in the Quarter Plane of the Plate for Graphite Fiber-Epoxy Matrix After Impact for $\pm 45^{\circ}$ Layup Angle, Thickness/Impact Radius Ratio = 10.0

31 Average Flexural Stress Distribution in the Quarter Plane of the Plate for Graphite Fiber-Epoxy Matrix After Impact for $\pm 45^{\circ}$ Layup Angle, Thickness/Impact Radius Ratio = 10.0

32 Maximum Interlaminar Shear Stress Distribution in the Quarter Plane of the Plate for Graphite Fiber-Epoxy Matrix After Impact for $\pm 45^{\circ}$ Layup Angle

33 Flexural Mean Stress History, $t_{11}+t_{33}$ versus Time After Impact, at Origin for Graphite-Fiber Epoxy

34 Interlaminar Flexural Stress History $\sqrt{t_{12}^2+t_{32}^2}$ Versus Time After Impact for Graphite-Epoxy r/a=0.6

Note:

τ = Time/a, (μsec/mm) for Figs. 14-19

τ = Time/$[b/(\hat{C}_{66}/\rho)^{1/2})]$ for Figs. 20-27 and Figs. 30-32

APPENDIX A: THEORETICAL ANALYSIS OF IMPACT IN COMPOSITE PLATES

Introduction

In a previous paper, (ref. 1) and in section I of this report the Author examined the propagation of wave surfaces in composite plates, and the response to a line impact load respectively. In section II of this report results for the two-dimensional plate response to a distributed impact load were presented. This analysis makes use of a computational tool called the "Fast Fourier Transform," which permits the calculation of the inverse of Fourier transforms on the digital computer. The application of this technique to the calculation of impact induced stresses is renewed in this section.

The mathematical model treats the laminated plate as an equivalent anisotropic material using a program developed by Chamis (ref. 9). A modification of Mindlin's theory of crystal plates is used, which results in five two-dimensional stress waves. Two of these waves describe the average or membrane stresses, while three other waves are associated with the flexural motion. The two former waves are non-dispersive, while the flexural waves exhibit strong dispersion at the low frequencies. In the Mindlin plate theory, (ref. 7), the impact transverse surface force enters the problem directly through the differential equations. To solve this initial value problem, a Laplace transform is taken on the time variable, and a double Fourier transform is taken on the two space variables. A solution of this triple transformed problem is obtained

in the transform space. Finally, the solution is completed by an analytical inversion of the double Fourier transform using the fast Fourier transform algorithm.

The displacement variables used in the theory are described as follows: u_1^0 and u_3^0 represent the midplane displacements in the plane of the plate, (see Fig. 9); u_2^0 represents the transverse midplane displacement u_1^1 and u_3^1 are a measure of the rotation of a line normal to the midplane. The equations, which were derived in Reference 1, are listed below, where q_2 is a transverse tension force on the plate surface and the constants C_{ij} are the equivalent elastic stiffnesses for the composite plate.

$$\rho\frac{\partial^2 u_1^o}{\partial t^2} = \hat{C}_{11}\frac{\partial^2 u_1^o}{\partial x_1^2} + C_{55}\frac{\partial^2 u_1^o}{\partial x_3^2} + (C_{55}+\hat{C}_{13})\frac{\partial^2 u_3^o}{\partial x_1 \partial x_3} + \frac{C_{12}}{2C_{22}}\frac{\partial q_2}{\partial x_1}$$

$$\rho\frac{\partial^2 u_3^o}{\partial t^2} = \hat{C}_{33}\frac{\partial^2 u_3^o}{\partial x_3^2} + C_{55}\frac{\partial^2 u_3^o}{\partial x_1^2} + (C_{55}+C_{13})\frac{\partial^2 u_1^o}{\partial x_1 \partial x_3} + \frac{C_{32}}{2C_{22}}\frac{\partial q_2}{\partial x_3} \qquad \text{(A-1)}$$

$$\rho \frac{\partial^2 u_2^o}{\partial t^2} = \hat{C}_{66}\left\{ \frac{\partial^2 u_2^o}{\partial x_1^2} + \frac{\partial^2 u_2^o}{\partial x_3^2} + \frac{1}{b}\frac{\partial u_1^1}{\partial x_1} + \frac{1}{b}\frac{\partial u_3^1}{\partial x_3} \right\} + \frac{q_2}{2b}$$

$$\rho \frac{\partial^2 u_1^1}{\partial t^2} = \hat{C}_{11}\frac{\partial^2 u_1^1}{\partial x_1^2} + C_{55}\frac{\partial^2 u_1^1}{\partial x_3^2} + (C_{55} + \hat{C}_{13})\frac{\partial^2 u_3^1}{\partial x_1 \partial x_3}$$

$$- \frac{3}{b}\hat{C}_{66}\left(\frac{\partial u_2^o}{\partial x_1} + \frac{u_1^1}{b}\right) + \frac{C_{12}}{2C_{22}}\frac{\partial q_2}{\partial x_1} \qquad \text{(A-2)}$$

$$\rho \frac{\partial^2 u_3^1}{\partial t^2} = \hat{C}_{33}\frac{\partial^2 u_3^1}{\partial x_3^2} + C_{55}\frac{\partial^2 u_3^1}{\partial x_1^2} + (C_{55} + \hat{C}_{13})\frac{\partial^2 u_1^1}{\partial x_1 \partial x_3}$$

$$- \frac{3}{b}\hat{C}_{66}\left(\frac{\partial u_2^o}{\partial x_3} + \frac{u_3^1}{b}\right) + \frac{C_{32}}{2C_{32}}\frac{\partial q_2}{\partial x_3}$$

where

$$\hat{C}_{11} = C_{11} - C_{12}^2/C_{22}$$

$$\hat{C}_{33} = C_{33} - C_{32}^2/C_{22}$$

$$\hat{C}_{13} = C_{13} - C_{12}C_{32}/C_{22}$$

$$\hat{C}_{66} = \kappa C_{66}$$

$$\kappa = \pi^2/12$$

Analytical Part of Solution: Midplane Motion

Solutions for the transforms of u_1^0 and u_3^0 are easily found. The Laplace variable is denoted by s and the Fourier variables are $k_1 = k \cos \alpha$, $k_3 = k \sin \alpha$. The vector formed

from $(k_1, k_3) = \underline{k}$ represents a Fourier wave number vector corresponding to the harmonic frequency $\omega = -is$. The resulting expressions become,

$$T[L[u_1^0]] = \hat{\bar{U}}_1 = i\,\hat{\bar{q}}\,\{(A_{22} + s^2/k^2)a_1 - A_{12}a_2\sin^2\alpha\}\cos\alpha/k\Delta$$

$$T[L[u_3^0]] = \hat{\bar{U}}_3 = i\,\hat{\bar{q}}\,\{(A_{11} + s^2/k^2)a_2 - A_{12}a_1\cos^2\alpha\}\sin\alpha/k\Delta \qquad \text{(A-3)}$$

$$\Delta = (A_{11} + s^2/k^2)\,(A_{22} + s^2/k^2) - A_{12}^2\cos^2\alpha\,\sin^2\alpha$$

where,

$$A_{11} = \hat{C}_{11}\cos^2\alpha + C_{55}\sin^2\alpha\,, \quad A_{22} = \hat{C}_{33}\sin^2\alpha + C_{55}\cos^2\alpha,$$

$$A_{12} = \hat{C}_{13} + C_{55}$$

$$a_1 = C_{12}/2C_{22}\,, \quad a_2 = C_{23}/2C_{22}$$

(A bar indicates a Laplace transform, and $\hat{q}$ indicates a double Fourier transform.) These solutions have the form.

$$\hat{\bar{U}} = i\,\hat{\bar{q}}\,P(s^2)/k\Delta(s^2)$$

where $P(s^2)$, $\Delta(s^2)$, are polynomials in s^2. $\Delta(s^2)$ has four zeroes in the complex s plane for each $\underline{k}$. These roots have the form,

$$s = \pm iv_1 k\,, \pm iv_2 k$$

where v_1 and v_2 are the plane wave velocities corresponding to the wave normal $\underline{k}$. Values of v_1 and v_2 versus α were reported in Reference 1. The Laplace inversion of (A-3) can then be done by use of the convolution theorem;

$$\hat{U}(k,\alpha,t) = \frac{i}{k} \int_o^t \hat{q}(k,\alpha,t-\tau)\, G(\tau)\, d\tau \tag{A-4}$$

$$G(t) = -\frac{k\, P(-k^2v_1^2)}{(v_1^2-v_2^2)} \frac{\sin k\, v_1 t}{v_1} + \frac{k\, P(-k^2v_2^2)}{(v_1^2-v_2^2)} \frac{\sin k\, v_2 t}{v_2}$$

Analytical Part: Flexural Motion

By a similar procedure, one can solve for u_2^o, u_1^1, u_3^1, which have the form

$$\hat{\bar{W}} = \hat{\bar{q}} \frac{R(s^2)}{\Delta_1(s^2,k^2)} \tag{A-5}$$

However in this case the roots of $\Delta_1 = 0$ are not proportional to k. This means that the velocity of the waves depends on the wavelength. It is known from the dispersion relations for these plates (ref. 7), that for k real, there will be six pure imaginary roots of $\Delta_1(s^2) = 0$;

$$s = \pm i\omega_1(\underset{\sim}{k}), \quad \pm i\omega_2(\underset{\sim}{k}), \quad \pm i\omega_3(\underset{\sim}{k})$$

The Laplace inversion of (A-5) again makes use of the convolution theorem and the residue calculus to invert $1/\Delta(s^2)$. Thus we obtain

$$\hat{W}(\underset{\sim}{k},t) = \int_0^t \hat{q}(\underset{\sim}{k},t-\tau)\ H(\tau)d\tau \qquad \text{(A-6)}$$

where

$$H(t) = \frac{R(\omega_1)}{(\omega_2^2-\omega_1^2)} \frac{\sin \omega_1 t}{(\omega_3^2-\omega_1^2)\omega_1} + \frac{R(\omega_2)}{(\omega_1^2-\omega_2^2)} \frac{\sin \omega_2 t}{(\omega_3^2-\omega_2^2)\omega_2}$$

$$+ \frac{R(\omega_3)}{(\omega_1^2-\omega_3^2)} \frac{\sin \omega_3 t}{(\omega_2^2-\omega_3^2)\omega_3}$$

Numerical Inversion:

The inversion of the Fourier transforms involves integrals of the form

$$U(x_1,x_3) = \frac{1}{4\pi^2} \int_{-\infty}^{\infty} \int \hat{U}(k_1,k_3)\ e^{-i\underset{\sim}{k}\cdot\underset{\sim}{x}} dk_1 dk_3 \qquad \text{(A-7)}$$

If significant changes in $U(\underline{x})$ occur over distances greater than λ, then the largest wave number of interest will be

$$K = 2\pi/\lambda \ .$$

Thus we may be satisfied with an approximation to $U(\underline{x})$ of the form

$$\tilde{U}(\underset{\sim}{x}) = \frac{1}{4\pi^2} \int_{-K}^{K}\int \hat{U}(\underset{\sim}{k})\ e^{-i\underset{\sim}{k}\cdot\underset{\sim}{x}} dk_1 dk_3$$

Shifting coordinates, this becomes

$$\tilde{U}(\underset{\sim}{x}) = \frac{e^{i(Kx_1+Kx_3)}}{4\pi^2} \int_0^{2K}\int \hat{U}(k_1-K,k_3-K)\ e^{-i\underset{\sim}{k}\cdot\underset{\sim}{x}} dk_1 dk_3$$

This latter integral may further be approximated by the following sum,

$$\tilde{U} = \frac{K^2}{\pi^2 N^2} e^{i(Kx_1+Kx_3)} \sum_{I,J=1}^{N} \hat{U}(k_1(I)-K, k_3(J)-K) e^{-i[k_1(J)x_1+k_3(J)x_3]}$$

where

$$k_1(I) = \frac{2K}{N}\left(\frac{1}{2} + (I-1)\right), \quad k_3(J) = \frac{2K}{N}\left[\frac{1}{2} + (J-1)\right]$$

or

$$\tilde{U} = \frac{K^2}{\pi^2 N^2} e^{iK(1-\frac{1}{N})(x_1+x_3)} \sum_{I,J=1}^{N} \hat{U}(I,J) e^{\frac{-i2\pi}{N}[(I-1)x_1+(J-1)x_3]} \tag{A-8}$$

When x_1 and x_3 are continuous variables, a summation of the type above must be performed for each point (x_1,x_3), which makes the calculation of the sums impractical for a large number of grid points (x_1,x_3). However, if x_1 and x_3 take on certain descrete values, there is an algorithm (ref. 8), which makes the calculation of these sums feasible for a large number of grid points. This algorithm, known as the "fast Fourier transform," takes a sampling matrix of the transform, say $A(k_I,k_J)$, and returns the following sampling matrix of the original transformed function,

$$T(L,M) = \sum_{J=1}^{N} \sum_{J=1} A(k_I,k_J) e^{-2\pi i[\frac{(I-1)(L-1)}{N}] + \frac{(J-1)(M-1)}{N}]} \tag{A-9}$$

This operation is known as a descrete finite Fourier transform. To put the above expression into this form we choose for the discrete values of x_1 and x_3 the numbers

$$x_1(L) = \frac{\lambda}{2}(L-1) \quad , \quad x_3(M) = \frac{\lambda}{2}(M-1) \tag{A-10}$$

Numerical Results

Several checks were made of the fast Fourier computer routine (ref. 8) used in this paper. First, known functions were transformed analytically and inverted numerically. These tests revealed that one must work with continuous functions if spurious oscillations near points of discontinuity are to be avoided.

Second, known one-dimensional solutions were checked using the numerical transform method, such as the impact of a string and the impact of a classical beam (see Section I). All these checks revealed very close agreement between the numerical transform output and the known analytical result.

The impact pressure distribution used was the following (see Figure 13)

$$q_2 = -P_o \left(1 - 2\left(\frac{r}{a}\right)^2 + \left(\frac{r}{a}\right)^4\right) \sin \frac{\pi t}{\tau_o} \tag{A-11}$$

for $r<a$, $(r^2 = x_1^2 + x_3^2)$ and $t<\tau_o$

$q_2 = 0$, for $r \geq a$ or $t>\tau_o$

The Hertz contact pressure based on static isotropic elasticity has the form

$$q_2 = P_o \left\{1 - \frac{r^2}{a^2}\right\}^{1/2} \qquad \text{(A-12)}$$

The principal difference between (A-11) and (A-12) lies in the infinite slope in (A-12) at $r=a$. The form of the impact pressure (A-11) was chosen to avoid such infinite slope. A distribution with continuous first and second derivatives (as the function (A-11) exhibits) was dictated by a desire to have all stresses continuous (i.e. to avoid shocks) and thus avoid spurious oscillations in the numerical inversion. This requirement results from the fact that in the Mindlin theory the average mid-plane stresses, having as wave sources terms proportional to ∇q_2, have the form

$$\hat{t}_{\alpha\beta} \sim \int_o^t k\hat{q}_2(k\tau)\sin k\, v(t-\tau)d\tau, \quad (\alpha,\beta = 1,3)$$

where v denotes either the first or second wave speed. Thus when $\hat{q}_2$ has the form of a short duration impact i.e.

$$\hat{q}_2 = \hat{Q}(k)\delta(\tau)$$

the Fourier transforms of the stresses are proportional to

$$\hat{t}_{\alpha\beta} \sim k^2\hat{Q}(k)\frac{\sin k\, vt}{k}$$

or for small times,

$$\hat{t}_{\alpha\beta} \sim \frac{\partial^2 Q(r)}{\partial r^2}$$

Thus for the stresses to be continuous at early times after the wave arrival, the spacial part of q_2 must have continuous second derivatives, which led to the choice of (A-11).This conclusion was also reached in numerical tests of the fast Fourier program when non-smooth load distributions were used. (See Section II of this report).

Using a "fast Fourier" computer routine written in Fortran IV, the induced impact stresses were calculated on both an IBM 360-91, and IBM 7094 computers. The grid used was 32 x 32 or 1024 points in the x_1 - x_3 plane. Execution time on the 360-91 was of the order of 12 seconds, and 22 seconds on the 7094. A denser grid of 64 x 64 was also tried with a running time of less than a minute on the IBM 360-91.

The output data consisted of a matrix (32 x 32) of stress values for the quarter plane of the plate. Interpolation, contour plotting, and three-dimensional plot routines, developed at the NASA Lewis Research Laboratory for use with a "Cal Comp" plotter, were used to obtain stress contours and three-dimensional plots as shown in Figure 2 of Section II.

The significant stress levels all lie within the surface bounded by the theoretical wave surface. In Figures 14, 17 the average or membrane mean stress contours $\frac{1}{2}(t^0_{11} + t^0_{33})$ for graphite fiber/epoxy matrix laminate plates are shown for layup angles of 0°, $\pm 45^\circ$.

The stresses shown correspond to the faster wave speed (quasi compressional wave) which is anisotropic, as is seen from the wave surfaces in Figure 10 . The stresses associated with the second wave speed (or quasi shear wave) were much smaller than those in the faster wave and are not presented.

The flexural or bending motion has three waves associated with it. The largest stresses however were found in the lowest flexural wave which travels at an isotropic wave speed given by

$$v_3 = [C_{66}\ \kappa/\rho]^{1/2}$$

($\kappa = \pi^2/12$, is Mindlin's correction factor (ref. 3). Stress contours for the mean flexural stress $\frac{1}{2}\left(t^1_{11} + t^1_{33}\right)$ in this wave are shown in Figures 20-25 for graphite fiber/epoxy matrix laminate plates under the transverse impact pressure (A-11). Note that the wave front is circular since v_3 is isotropic for laminate plates. Stresses in the second and third flexural waves were found to be small. Three-dimensional computer plots are shown in Figures 26-32.

The maximum stress levels were found to occur immediately after the end of impact and appeared to propagate along the fiber directions, given by the layup angles.

APPENDIX B: LIST OF SYMBOLS

a	half width of impact contact line (one dimensional) or radius of impact contact circle (two dimensional)
a_i	ratios of elastic constants
A_{ij}	acoustic tensor components
b	half thickness of plate
C_{ij}	anisotropic elastic constants
$D(I)$	column matrix of discrete Fourier Transform
e_{ij}	elastic strain tensor
E	Young's Modulus
F	impact force
$k, \underset{\sim}{k}, K$	wave number
k_2	Hertz contact law constant
$L[f]$	Laplace transform
M	mass of impacting object
$\underset{\sim}{n}$	wave normal
P_n	Legendre polynomials
q, q_2	impact loading function
$\underset{\sim}{r}$	position vector
s	Laplace transform variable
t	time
t_{ij}	stress tensor
$\underset{\sim}{u}$	displacement vector
u_1^o, u_3^o	inplane displacements
u_2^o	transverse plate displacement
u_1^1, u_3^1	flexural rotation displacements

u_2^1, $u_2^{(2)}$	higher order plate displacements
v	wave velocity
V	velocity of impacting object
x_1, x_2, x_3	cartesian coordinates

α	angle of one-dimensional wave normal
α	relative approach of impacting object and plate
Δ, Δ_1	characteristic acoustic determinant
ϕ	fiber layup angle
κ	Mindlin correction factor, or wave number (see the text)
λ	wave length
ν	Poisson's ratio
ρ	density
ω, Ω_o	frequency
τ	impact time or time parameter
ζ	one-dimensional wave normal direction

APPENDIX C: MATERIAL PROPERTIES

All the calculations in this report are for the composite material consisting of graphite fibers in an epoxy matrix.

The values of the elastic constants for graphite/epoxy, for various ply layup angles, were obtained from an analysis by Chamis (ref. 9). The assumed properties of the graphite fibers and epoxy used by Chamis are as follows;

Epoxy — Young's Modulus $E = 0.57\ 10^6$psi

Poisson's Ratio $\nu = 0.36$

Graphite Fiber (Thornel 50)

"1" Axis along the fiber

$E_{11} = 50\ 10^6$psi

$E_{22} = E_{33} = 1.0\ 10^6$psi

$\nu_{12} = \nu_{13} = 0.20$

$\nu_{23} = 0.25$

$G_{12} = 1.3\ 10^6$

$G_{23} = 0.7\ 10^6$

The values of the elastic constants for the composite are given in the following table.

TABLE I. - STRESS-STRAIN COEFFICIENTS FOR 55 PERCENT GRAPHITE FIBER-EPOXY MATRIX COMPOSITE

[All constants to be multiplied by 10^6 psi; data obtained from ref. 7.]

0° Layup

27.95	0.3957	0.3957	0	0	0
	1.170	0.4601	0	0	0
		1.170	0	0	0
			0.3552	0	0
				0.7197	0
					0.3552

$\pm 15^\circ$ Layup

24.56	0.4000	1.986	0	0	0
	1.170	0.4558	0	0	0
		1.374	0	0	0
			0.3552	0	0
				2.310	0
					0.3552

$\pm 30^\circ$ Layup

16.48	0.4118	5.167	0	0	0
	1.170	0.4400	0	0	0
		3.093	0	0	0
			0.3552	0	0
				5.491	0
					0.3552

$\pm 45^\circ$ Layup

8.197	0.4279	6.758	0	0	0
	1.170	0.4279	0	0	0
		8.179	0	0	0
			0.3552	0	0
				7.082	0
					0.3552

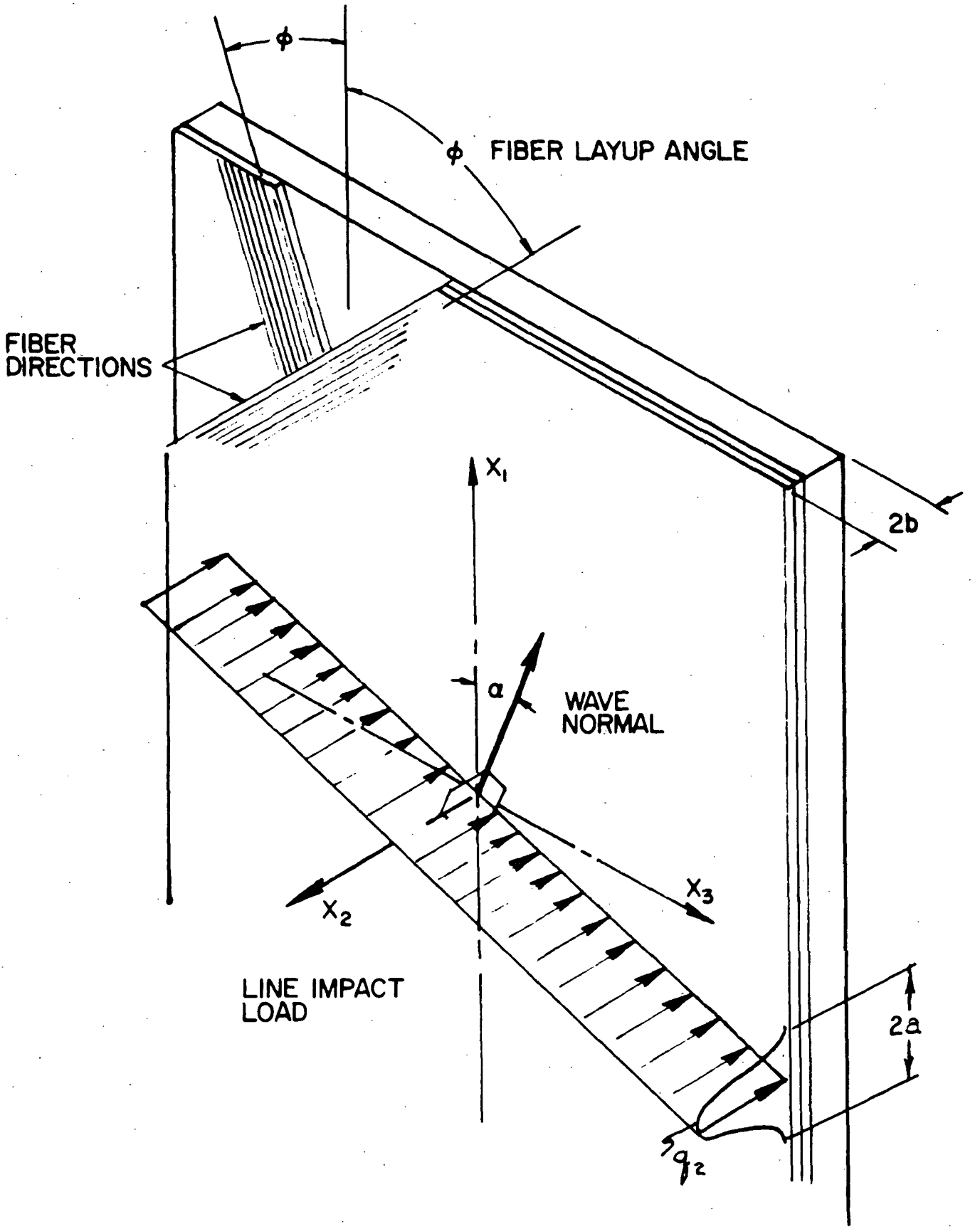

FIGURE 1 · DIAGRAM OF COMPOSITE PLATE GEOMETRY AND NOTATION

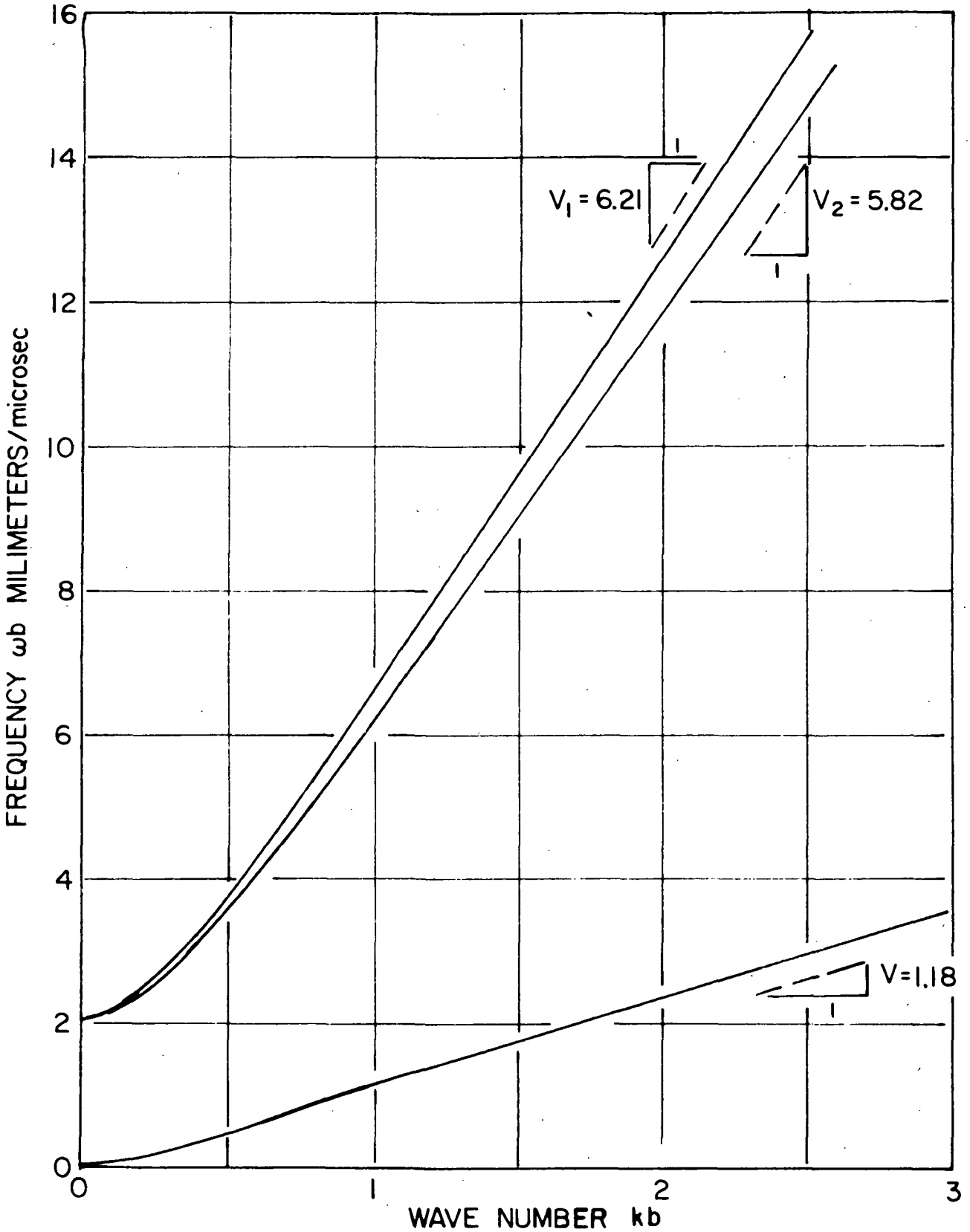

FIGURE 2·DISPERSION RELATION FOR FLEXURAL MOTION ωb vs kb
FOR 55% GRAPHITE-EPOXY ± 45° LAYUP ANGLE
FOR WAVE NORMAL $\alpha = 0$ ALONG X_1 AXIS

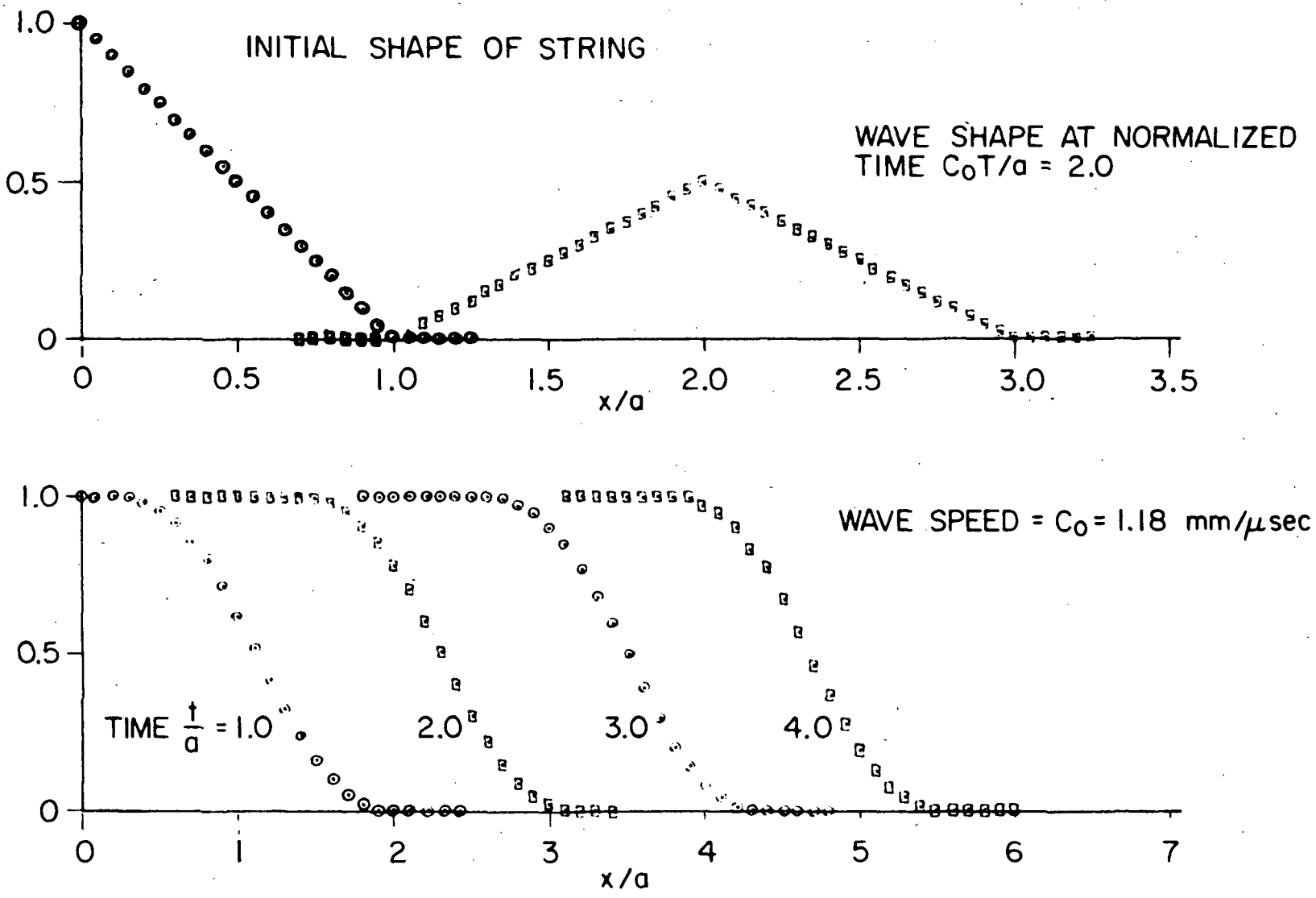

FIGURE 3 · a) WAVE IN AN INFINITE STRING FOR AN INITIAL TRIANGULAR DISPLACEMENT (ONLY RIGHT HALF SHOWN)

b) COMPUTER CALCULATION OF DISPLACEMENT WAVES IN AN INFINITE STRING DUE TO IMPULSE LOADING EQU. (19)

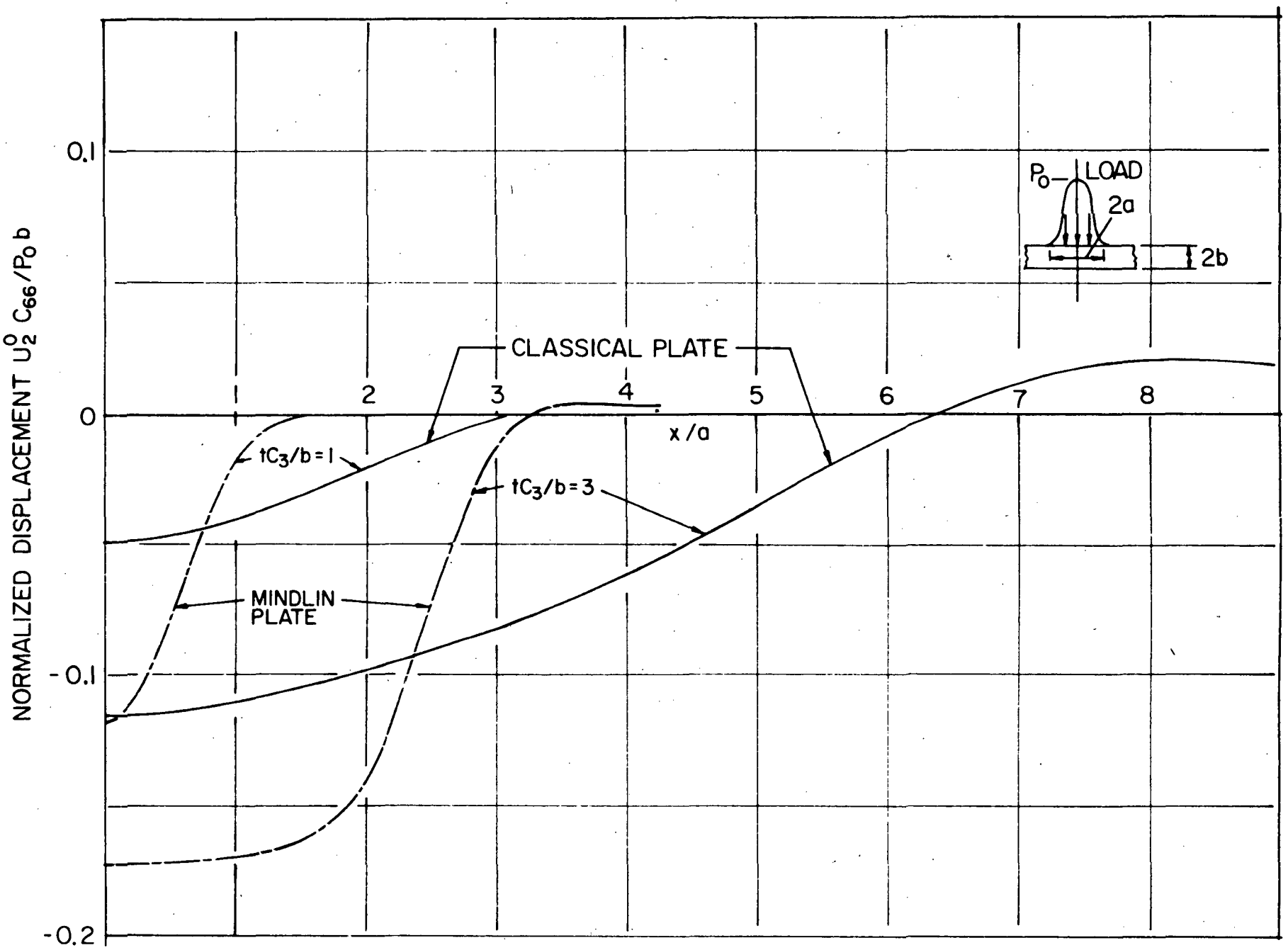

FIGURE 4 · MIDPLANE DISPLACEMENT WAVES 55% GRAPHITE-EPOXY COMPOSITE, ± 45° LAYUP a/b = 1.0, IMPACT LOAD ALONG X_3 AXIS, COMPARISON OF MINDLIN AND CLISSICAL THEORIES

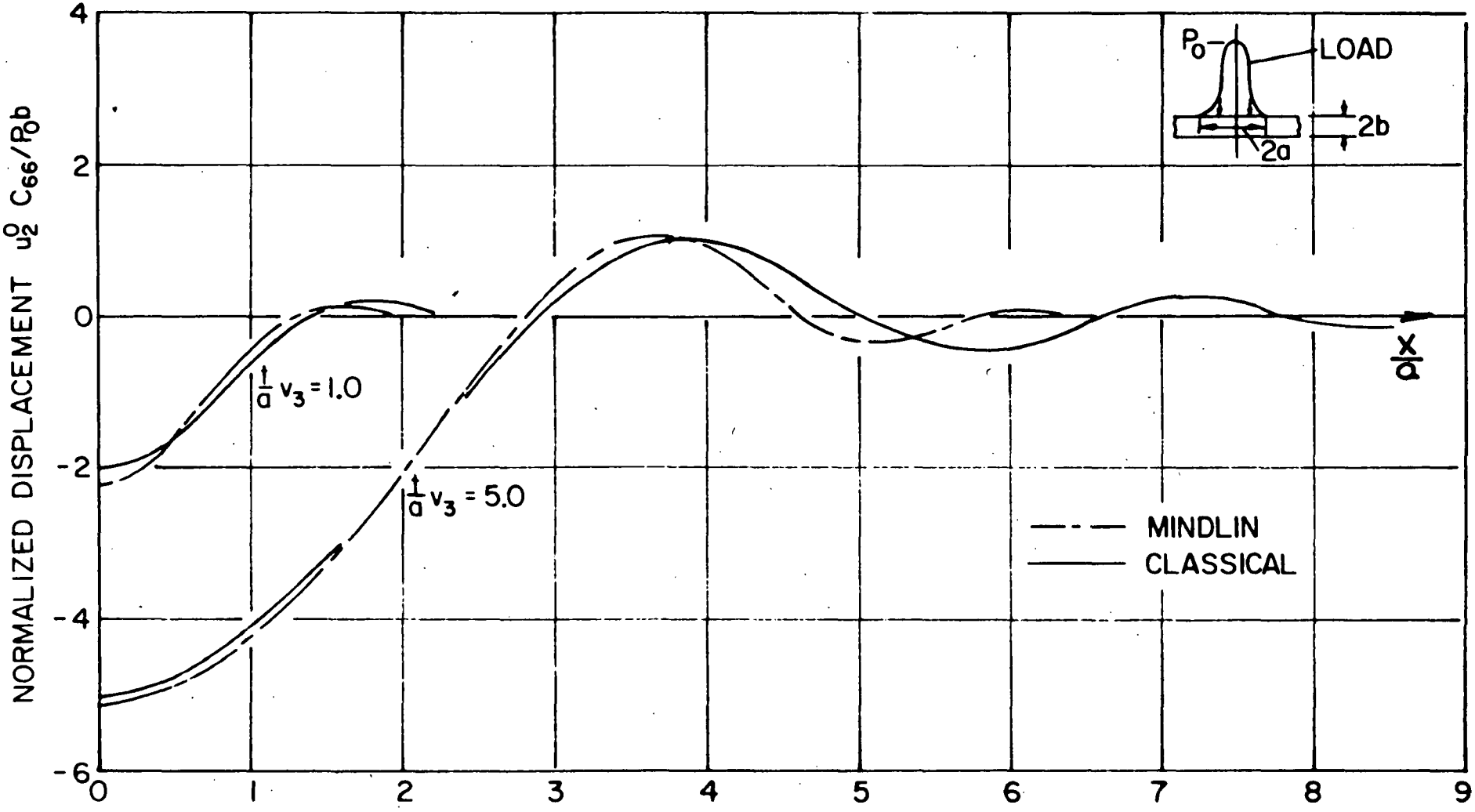

FIGURE 5 · MIDPLANE DISPLACEMENT WAVES, 55% GRAPHITE-EPOXY COMPOSITE, ± 45° LAYUP ANGLE a/b = 10.0, IMPACT LOAD ALONG X_3 AXIS COMPARISON OF MINDLIN AND CLASSICAL THEORIES

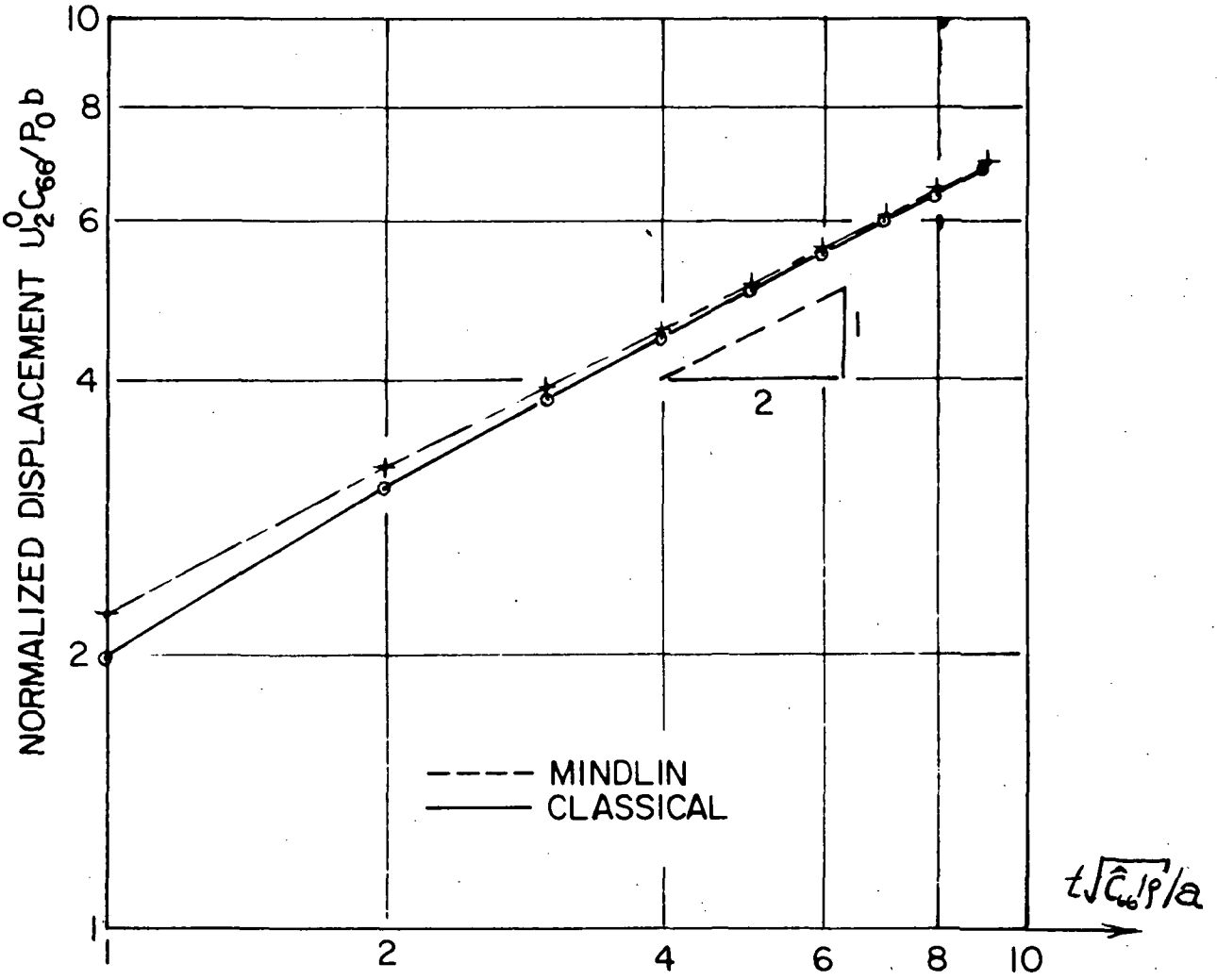

FIGURE 6 · CENTER MIDPLANE DISPLACEMENT vs TIME 55% GRAPHITE - EPOXY COMPOSITE, ±45° LAYUP ANGLE IMPACT LOAD ALONG X_3 AXIS, a/b = 10, COMPARISON OF MINDLIN AND CLASSICAL THEORIES

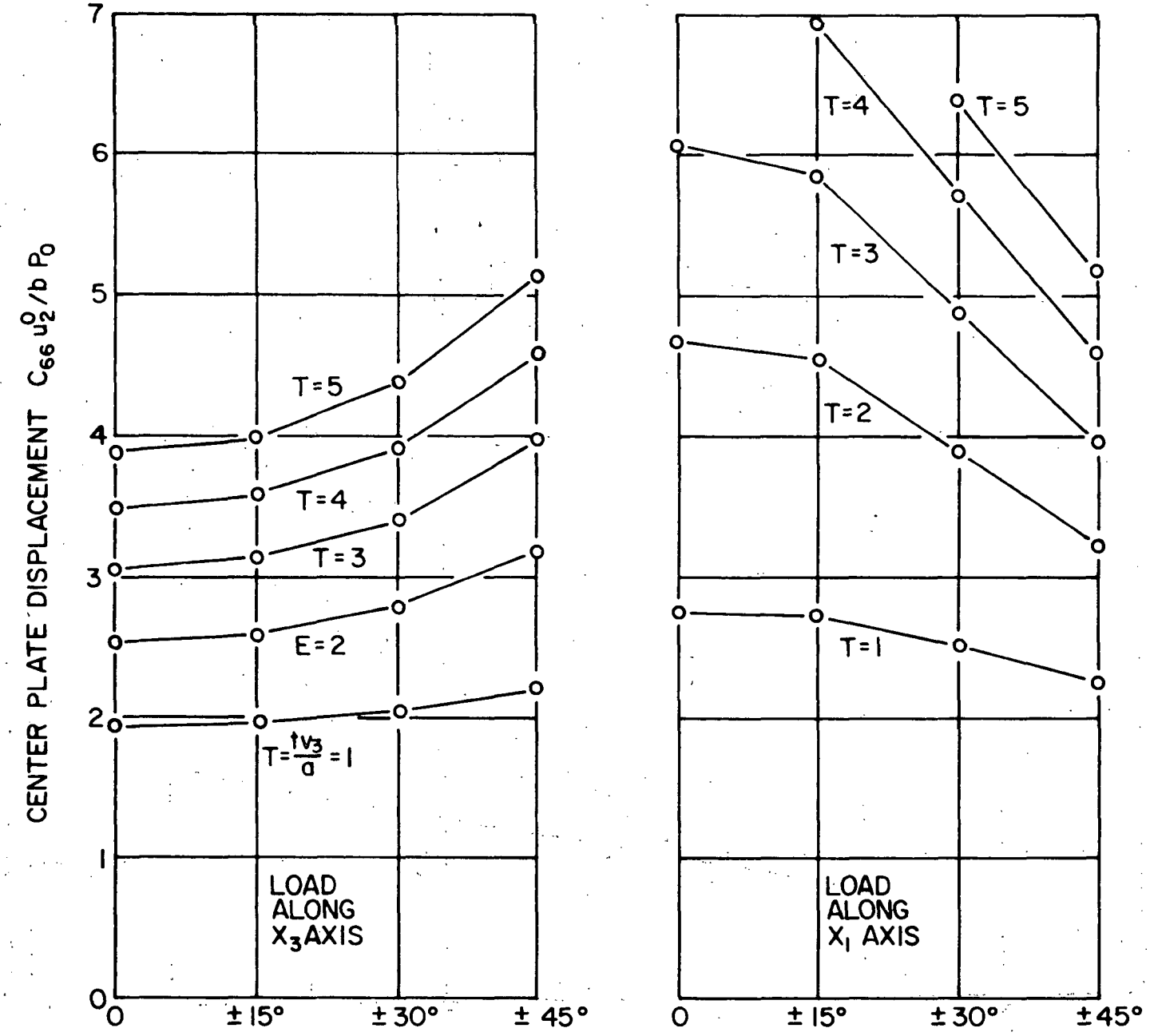

FIGURE 7· CENTER MIDPLANE DISPLACEMENT vs LAYUP ANGLE 55 % GRAPHITE FIBER - EPOXY MATRIX COMPOSITE a/b = 10.0

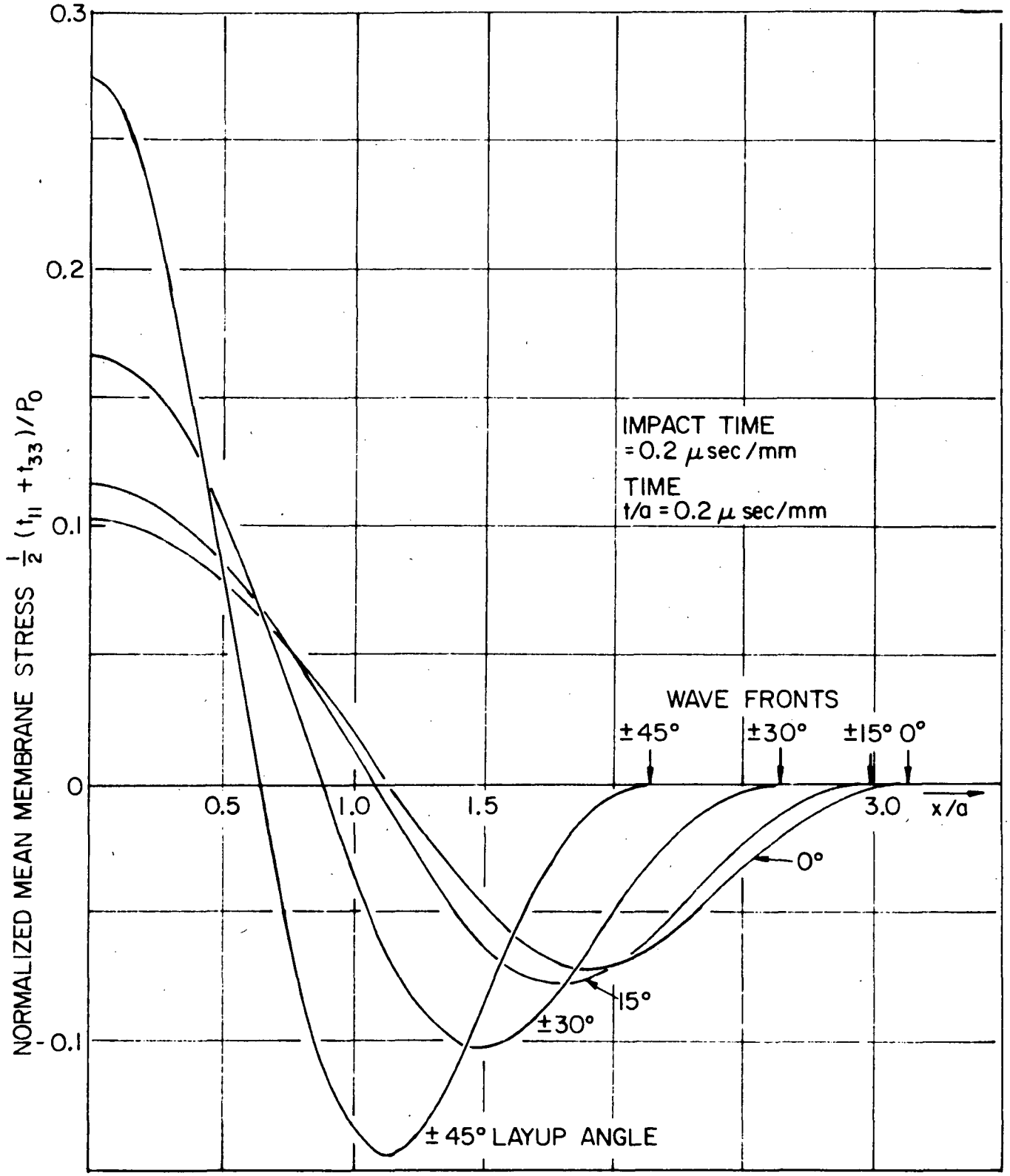

FIGURE 8· MEAN INPLANE STRESS $(t_{11}^0+t_{33}^0)/2$ vs DISTANCE x/a 55% GRAPHITE FIBER - EPOXY MATRIX COMPOSITE PLATE FOR VARIOUS LAYUP ANGLES, LOAD ALONG x_3 AXIS

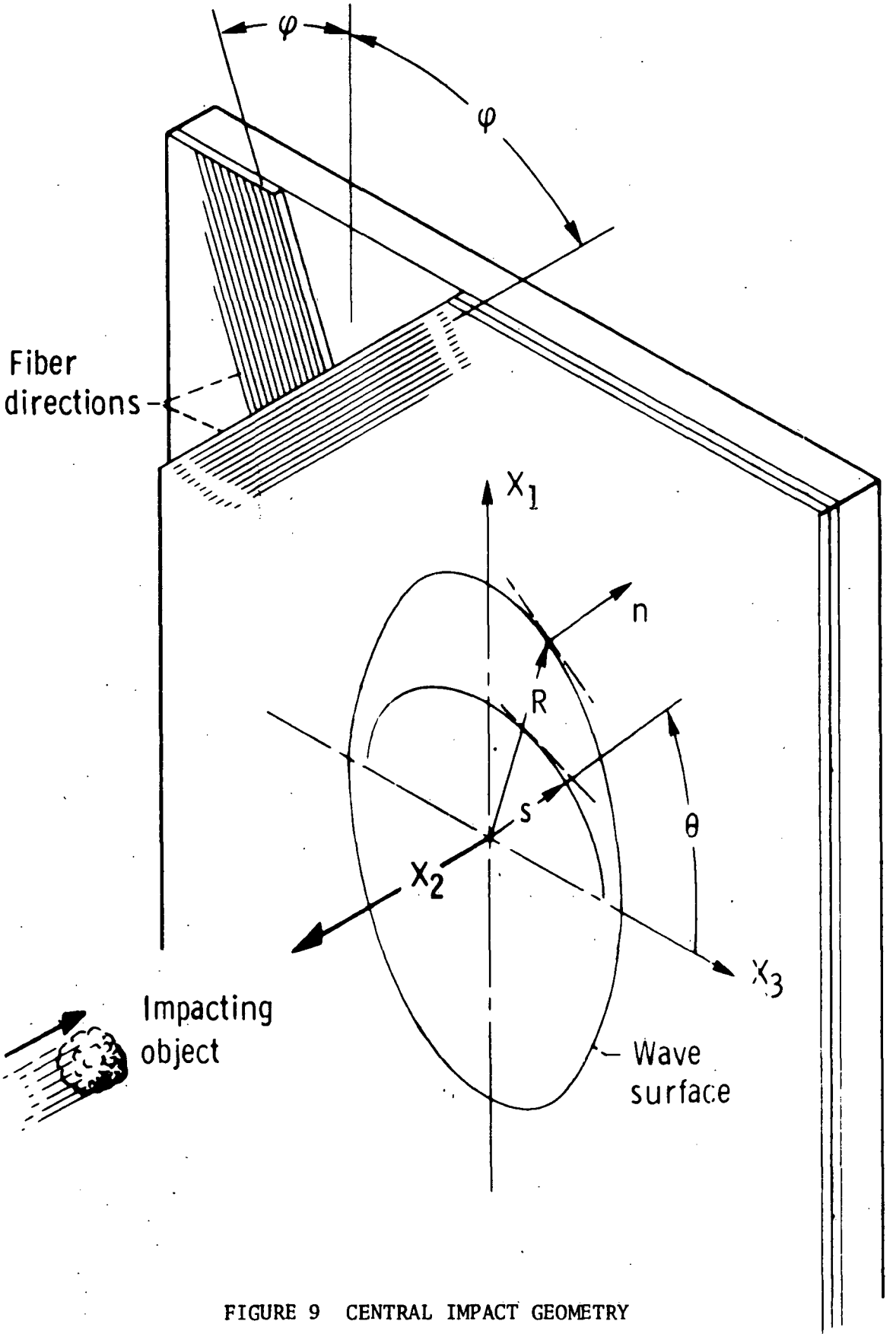

FIGURE 9 CENTRAL IMPACT GEOMETRY

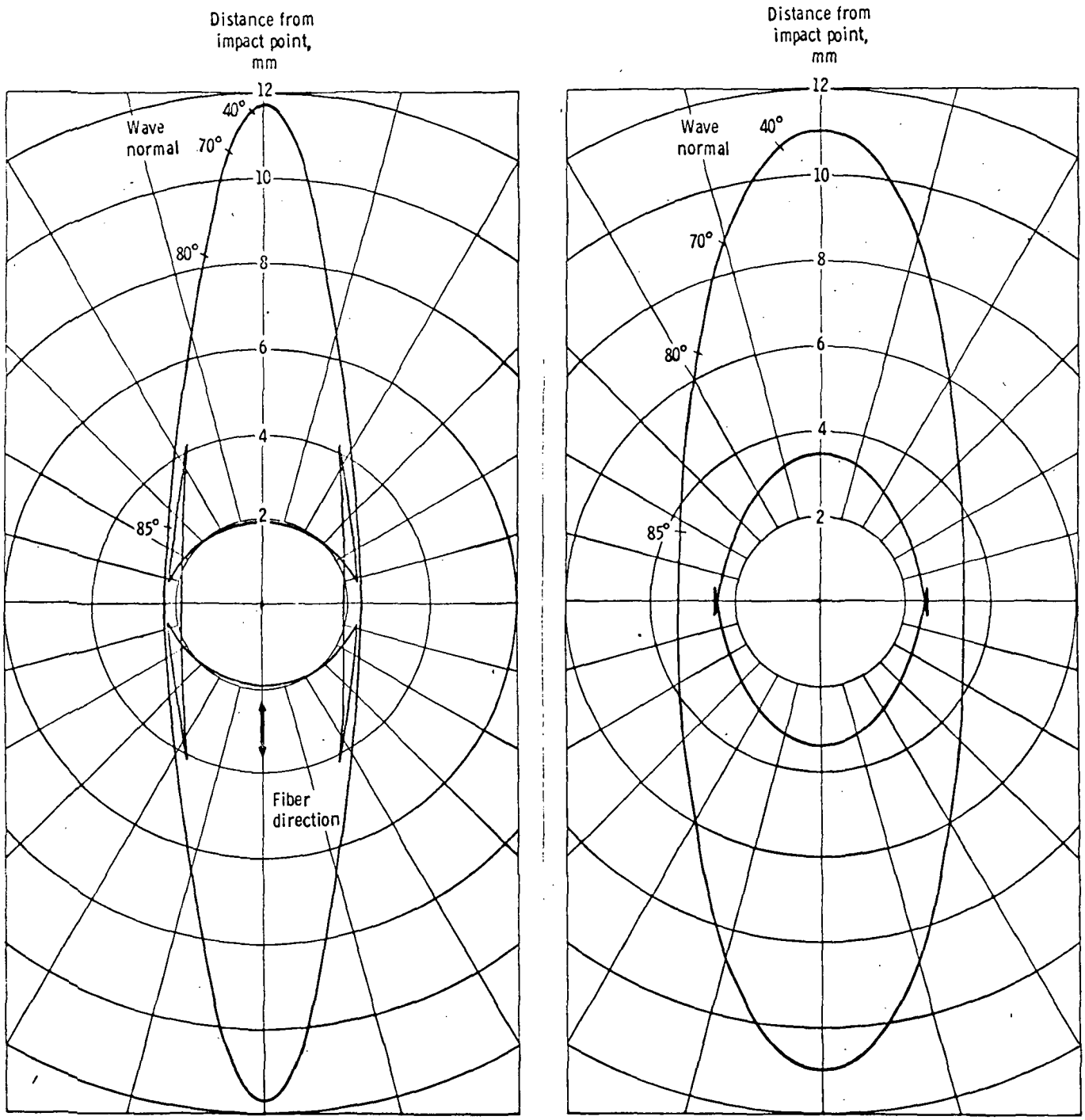

FIGURE 10. a) WAVE SURFACES FOR GRAPHITE/EPOXY 0^{o} and $\pm 15^{o}$ FIBER LAYUP ANGLE

$t = 10^{-6}$ sec.

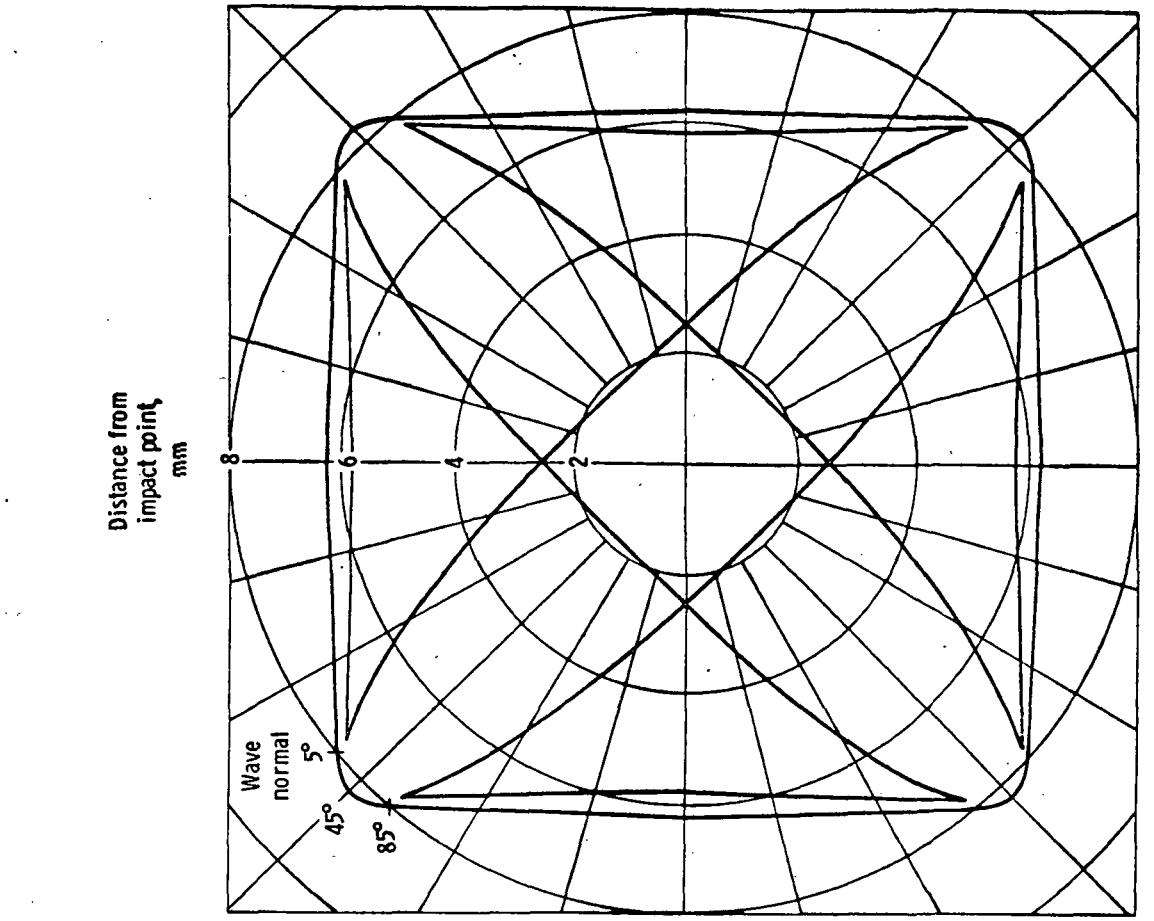

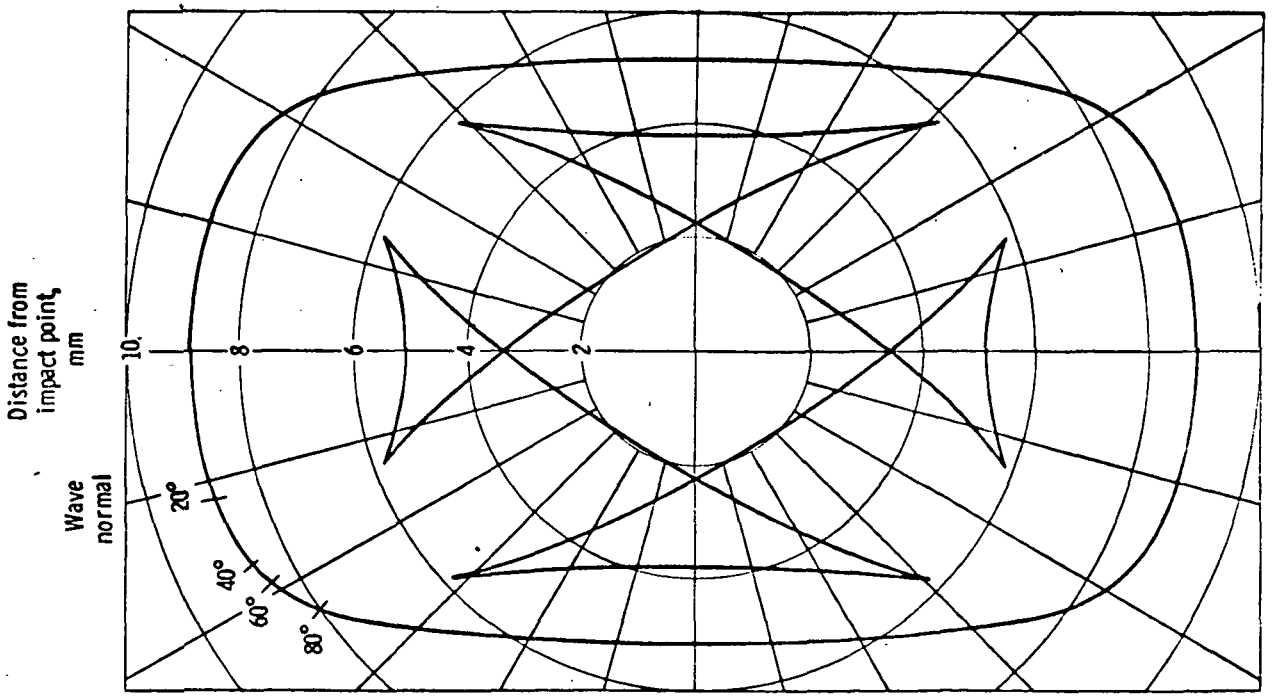

FIGURE 10. b) WAVE SURFACES FOR GRAPHITE/EPOXY $\pm 30^{\circ}$ and $\pm 45^{\circ}$ FIBER LAYUP ANGLE

$t = 10^{-6}$ sec.

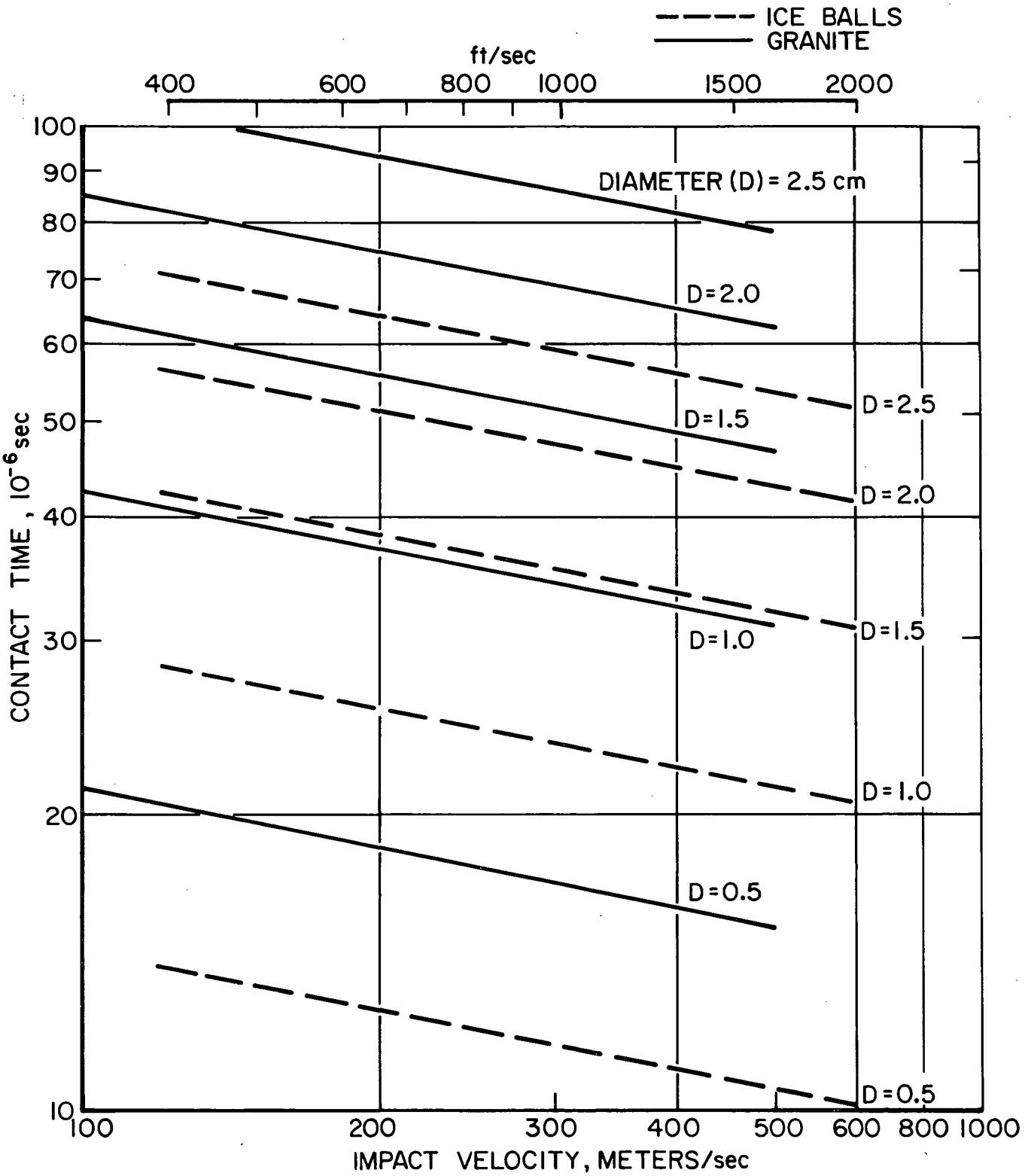

HERTZIAN IMPACT CONTACT TIME FOR GRANITE AND ICE SPHERES ON GRAPHITE/EPOXY COMPOSITE

FIGURE 11

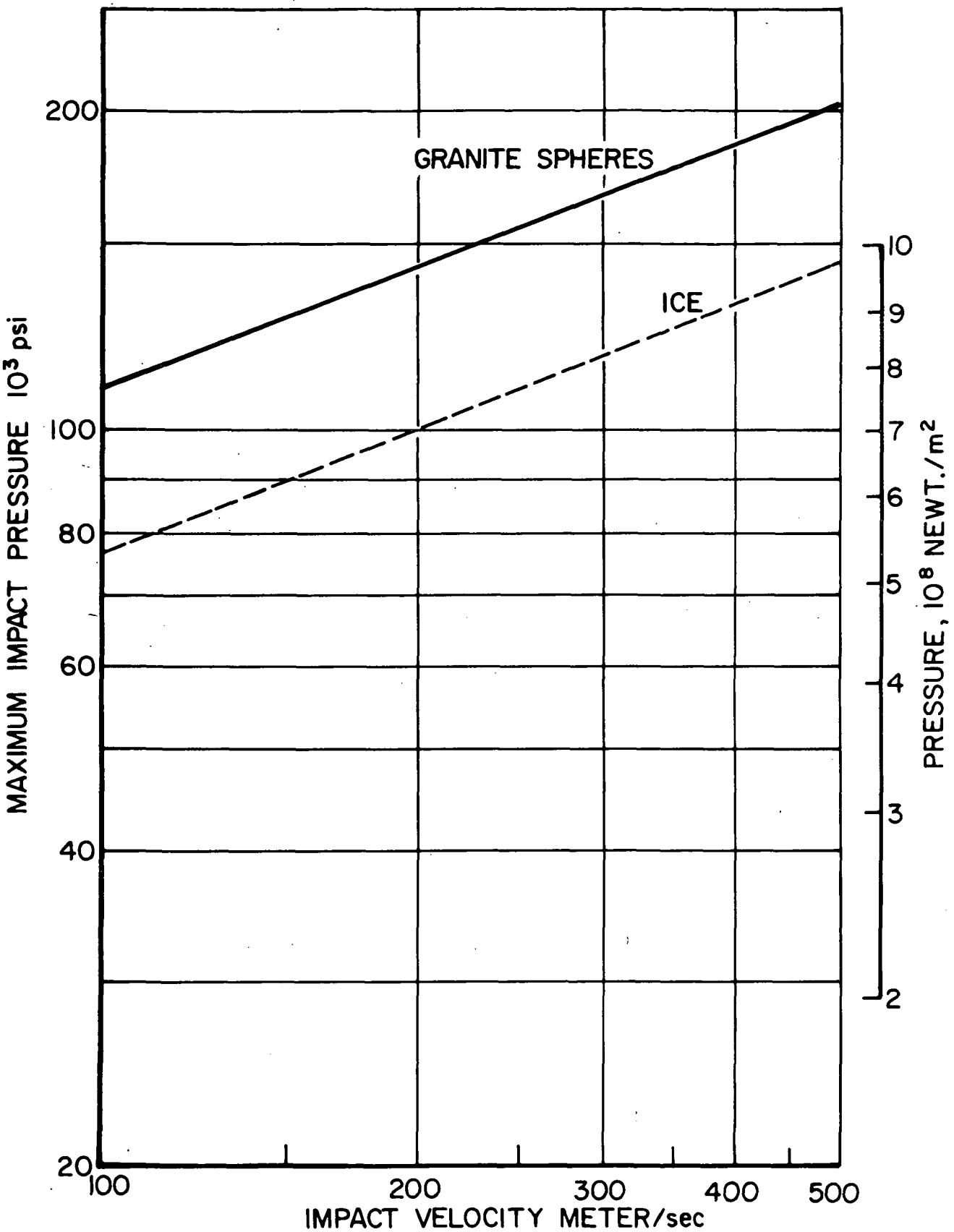

FIGURE 12a MAXIMUM HERTZIAN IMPACT PRESSURE FOR GRAPHITE/EPOXY COMPOSITE

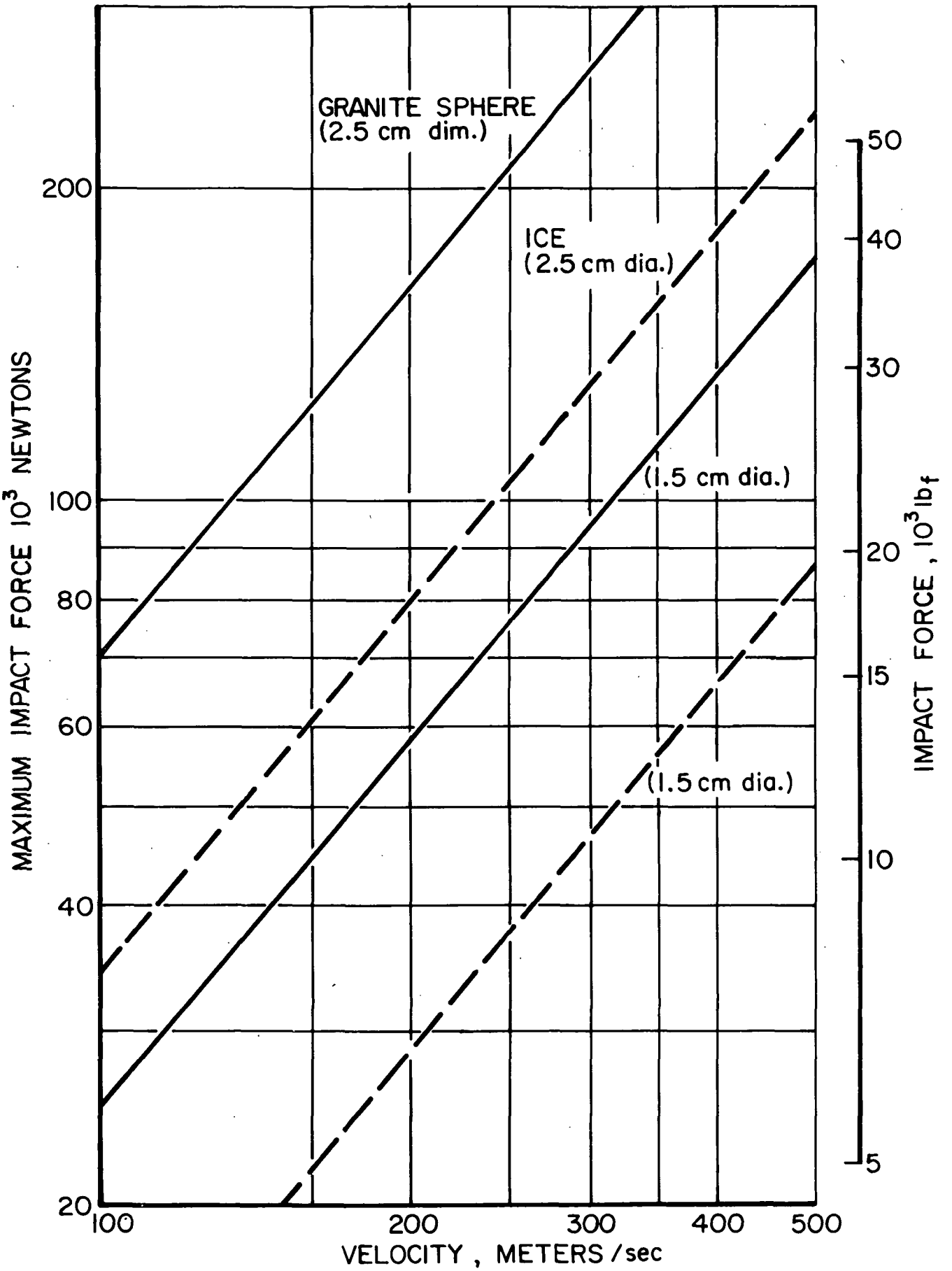

FIGURE 12b MAXIMUM HERTZIAN IMPACT FORCE

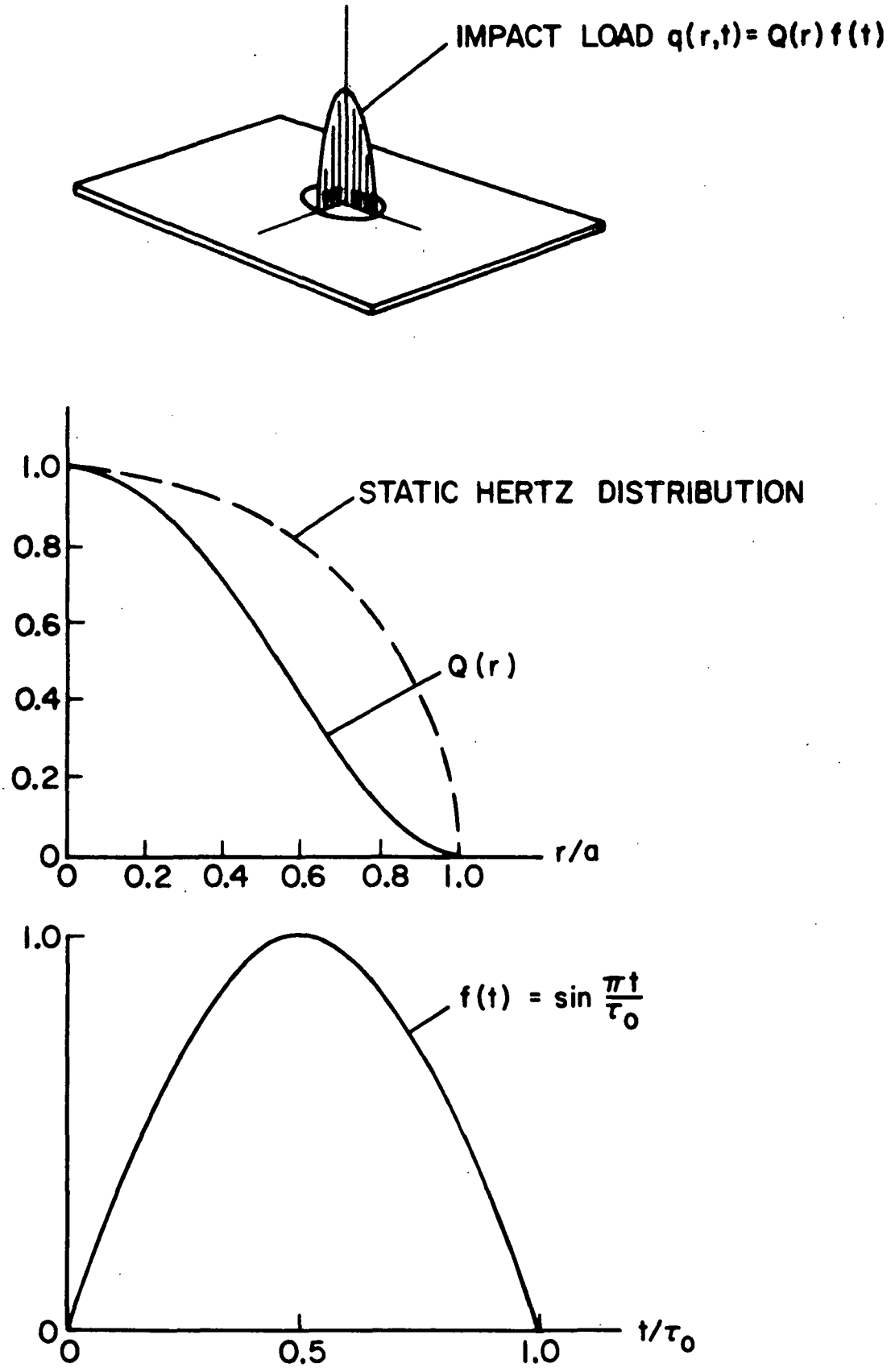

FIGURE 13 IMPACT LOAD DISTRIBUTION

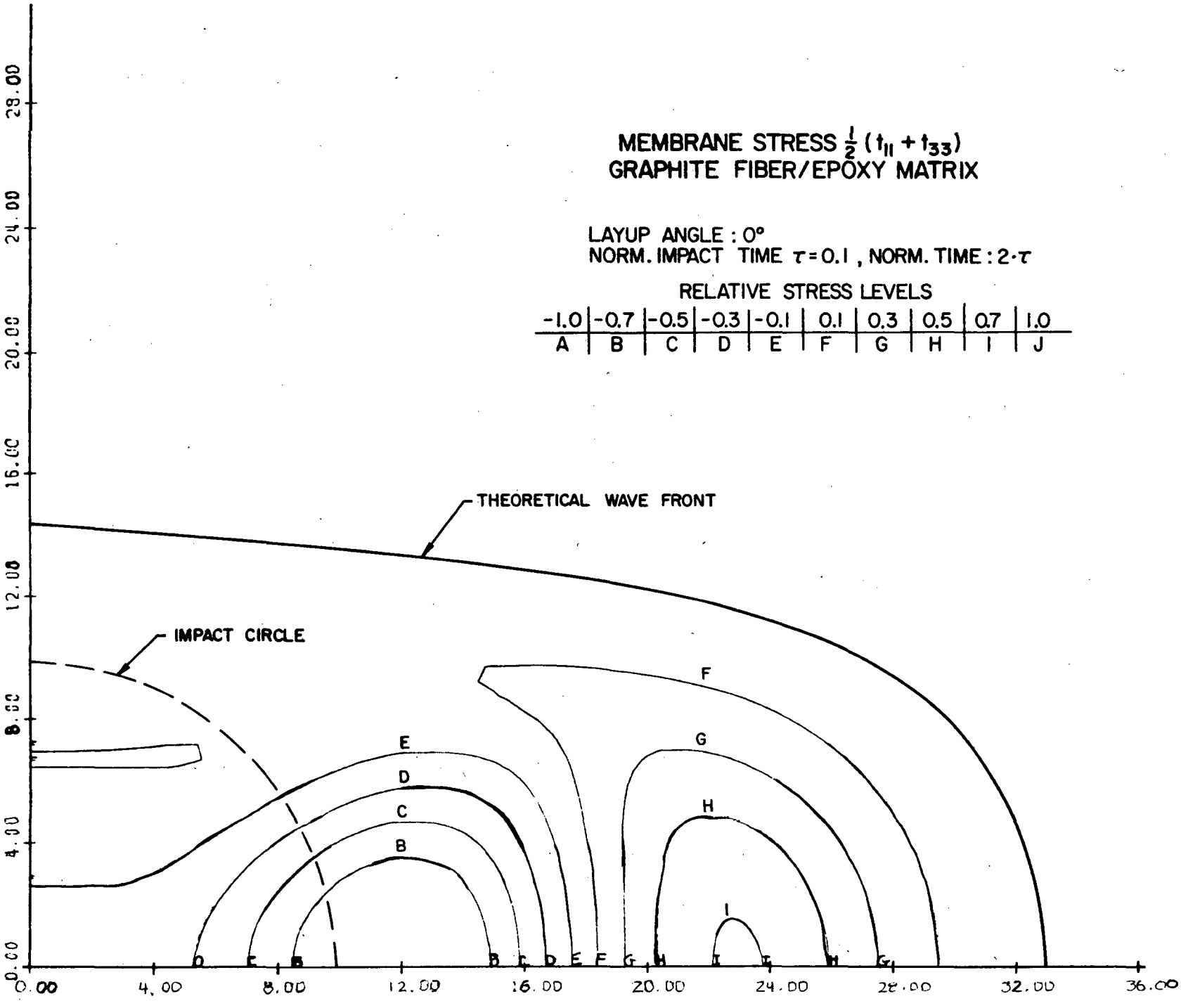
MEMBRANE STRESS $\frac{1}{2}(t_{11} + t_{33})$
GRAPHITE FIBER/EPOXY MATRIX
LAYUP ANGLE : 0°
NORM. IMPACT TIME $\tau = 0.1$, NORM. TIME : $2 \cdot \tau$
RELATIVE STRESS LEVELS
-1.0 | -0.7 | -0.5 | -0.3 | -0.1 | 0.1 | 0.3 | 0.5 | 0.7 | 1.0
A | B | C | D | E | F | G | H | I | J
THEORETICAL WAVE FRONT
IMPACT CIRCLE
0.00
4.00
8.00
12.00
16.00
20.00
24.00
28.00
32.00
36.00

FIGURE 14

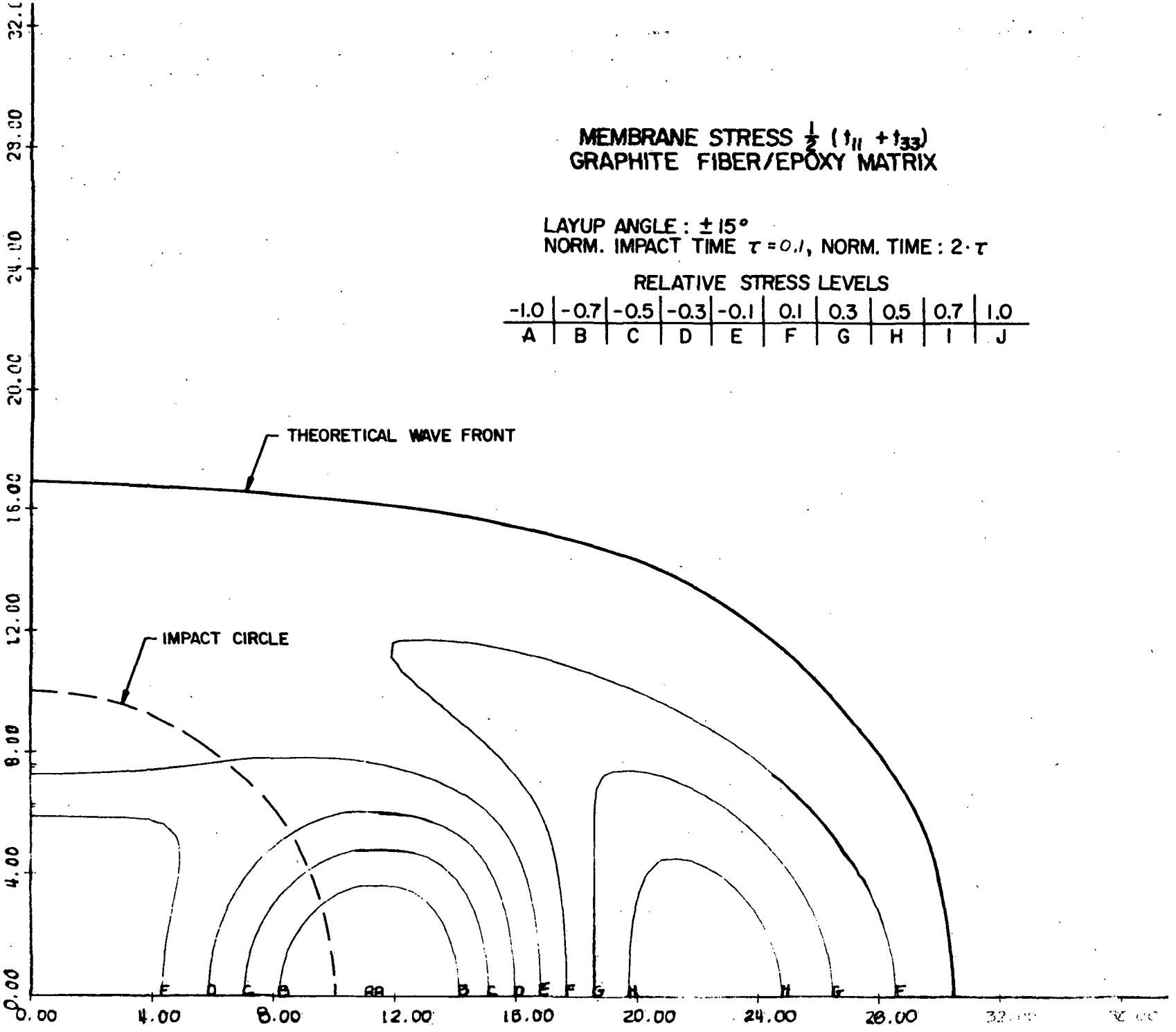
MEMBRANE STRESS $\frac{1}{2}(t_{11}+t_{33})$
GRAPHITE FIBER/EPOXY MATRIX
LAYUP ANGLE : ±15°
NORM. IMPACT TIME $\tau = 0.1$, NORM. TIME : $2\cdot\tau$
RELATIVE STRESS LEVELS
-1.0 | -0.7 | -0.5 | -0.3 | -0.1 | 0.1 | 0.3 | 0.5 | 0.7 | 1.0
A | B | C | D | E | F | G | H | I | J
THEORETICAL WAVE FRONT
IMPACT CIRCLE
0.00
4.00
8.00
12.00
16.00
20.00
24.00
28.00
32.00

FIGURE 15

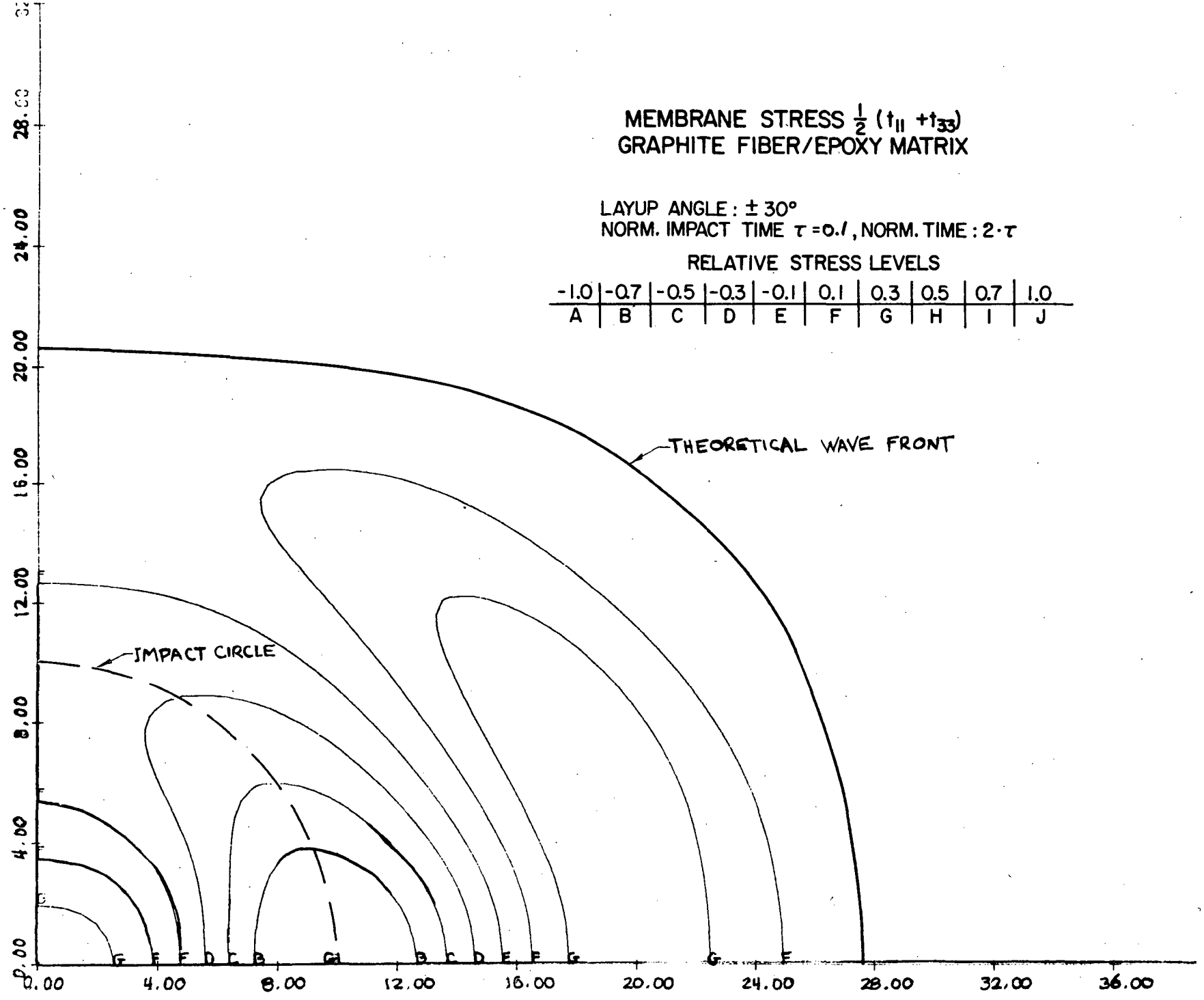
MEMBRANE STRESS $\frac{1}{2}(t_{11}+t_{33})$
GRAPHITE FIBER/EPOXY MATRIX
LAYUP ANGLE : ± 30°
NORM. IMPACT TIME τ = 0.1 , NORM. TIME : 2·τ
RELATIVE STRESS LEVELS
-1.0 | -0.7 | -0.5 | -0.3 | -0.1 | 0.1 | 0.3 | 0.5 | 0.7 | 1.0
A | B | C | D | E | F | G | H | I | J
THEORETICAL WAVE FRONT
IMPACT CIRCLE
0.00
4.00
8.00
12.00
16.00
20.00
24.00
28.00
32.00
36.00

FIGURE 16

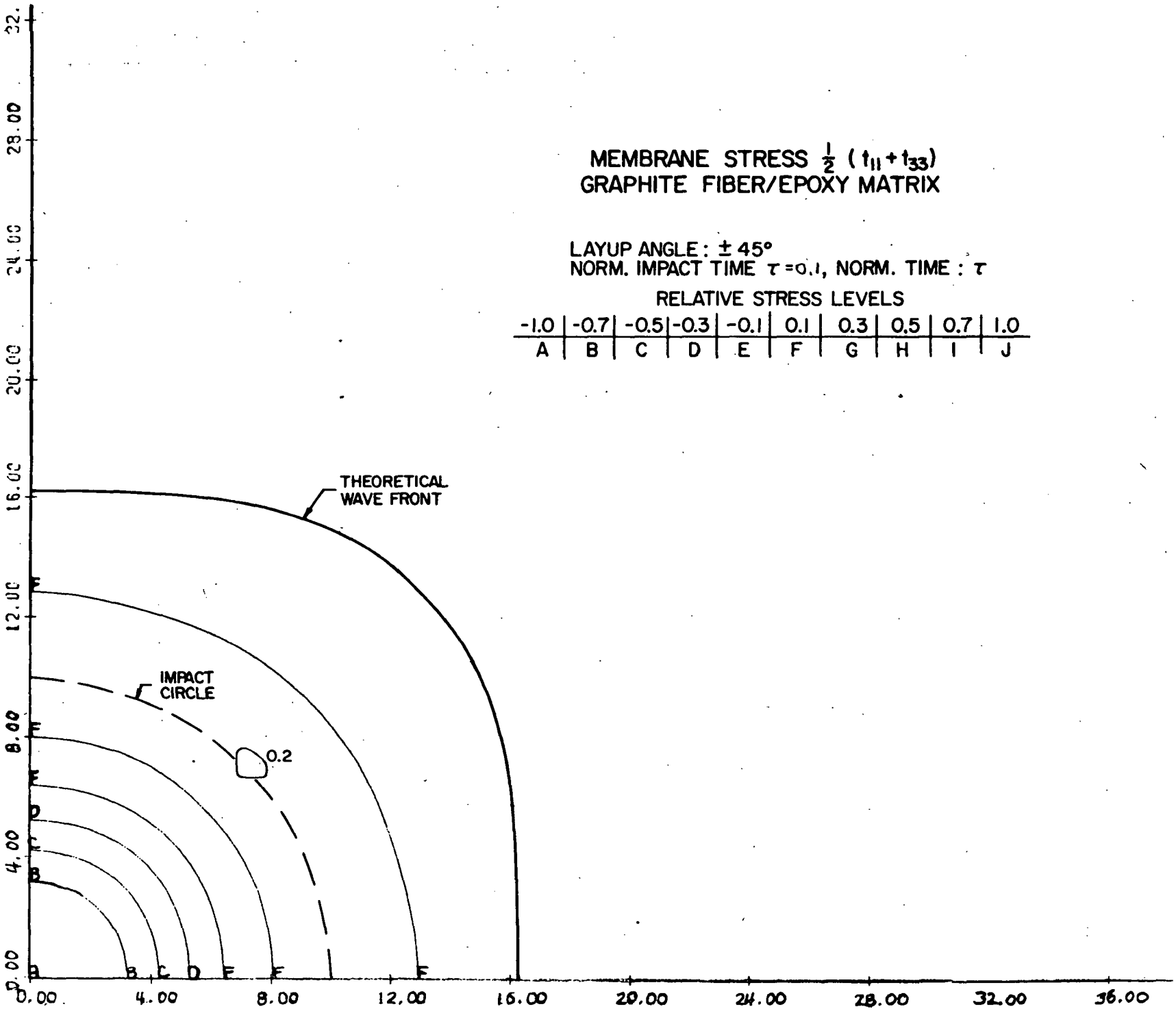
MEMBRANE STRESS $\frac{1}{2}(t_{11}+t_{33})$
GRAPHITE FIBER/EPOXY MATRIX
LAYUP ANGLE : ± 45°
NORM. IMPACT TIME τ =0.1, NORM. TIME : τ
RELATIVE STRESS LEVELS
-1.0 | -0.7 | -0.5 | -0.3 | -0.1 | 0.1 | 0.3 | 0.5 | 0.7 | 1.0
A | B | C | D | E | F | G | H | I | J
THEORETICAL WAVE FRONT
IMPACT CIRCLE
0.2
0.00
4.00
8.00
12.00
16.00
20.00
24.00
28.00
32.00
36.00

FIGURE 17

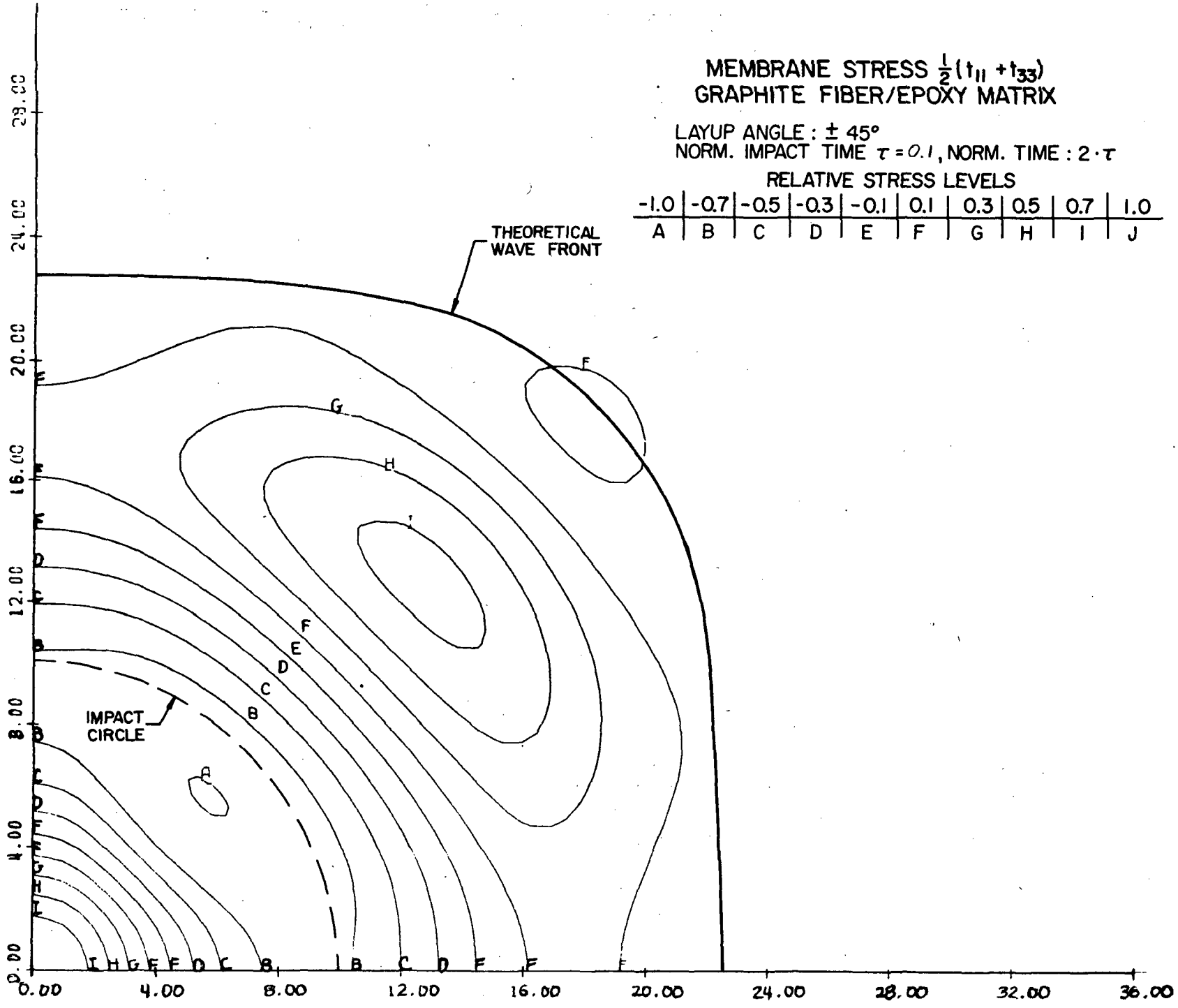
MEMBRANE STRESS $\frac{1}{2}(t_{11} + t_{33})$
GRAPHITE FIBER/EPOXY MATRIX
LAYUP ANGLE : ± 45°
NORM. IMPACT TIME $\tau = 0.1$, NORM. TIME : $2 \cdot \tau$
RELATIVE STRESS LEVELS
-1.0 | -0.7 | -0.5 | -0.3 | -0.1 | 0.1 | 0.3 | 0.5 | 0.7 | 1.0
A | B | C | D | E | F | G | H | I | J
THEORETICAL WAVE FRONT
IMPACT CIRCLE
0.00
4.00
8.00
12.00
16.00
20.00
24.00
28.00
32.00
36.00

FIGURE 18

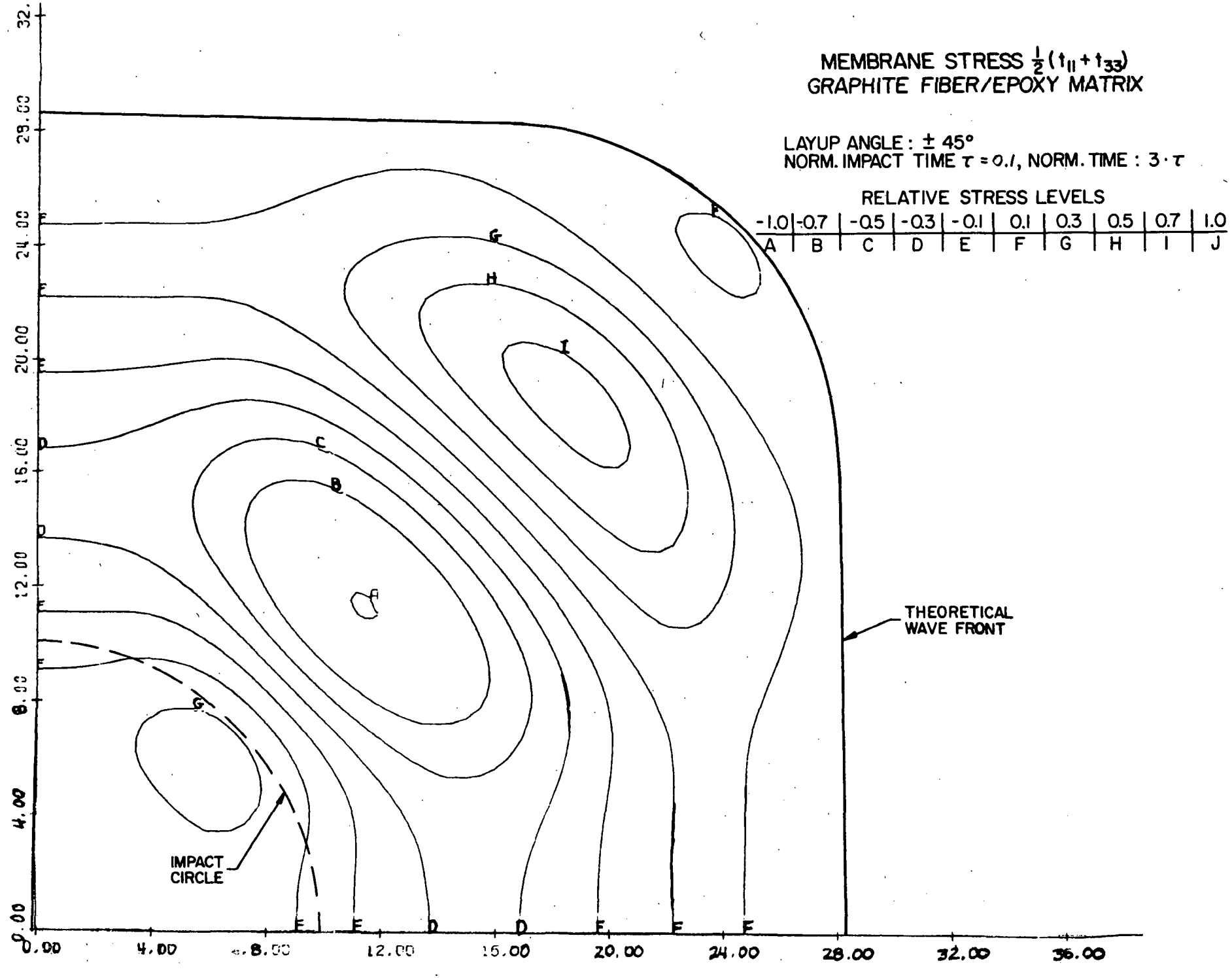
MEMBRANE STRESS $\frac{1}{2}(t_{11}+t_{33})$
GRAPHITE FIBER/EPOXY MATRIX
LAYUP ANGLE : ± 45°
NORM. IMPACT TIME $\tau = 0.1$, NORM. TIME : $3\cdot\tau$
RELATIVE STRESS LEVELS
-1.0 | -0.7 | -0.5 | -0.3 | -0.1 | 0.1 | 0.3 | 0.5 | 0.7 | 1.0
A | B | C | D | E | F | G | H | I | J
THEORETICAL WAVE FRONT
IMPACT CIRCLE
0.00
4.00
8.00
12.00
16.00
20.00
24.00
28.00
32.00
36.00

FIGURE 19

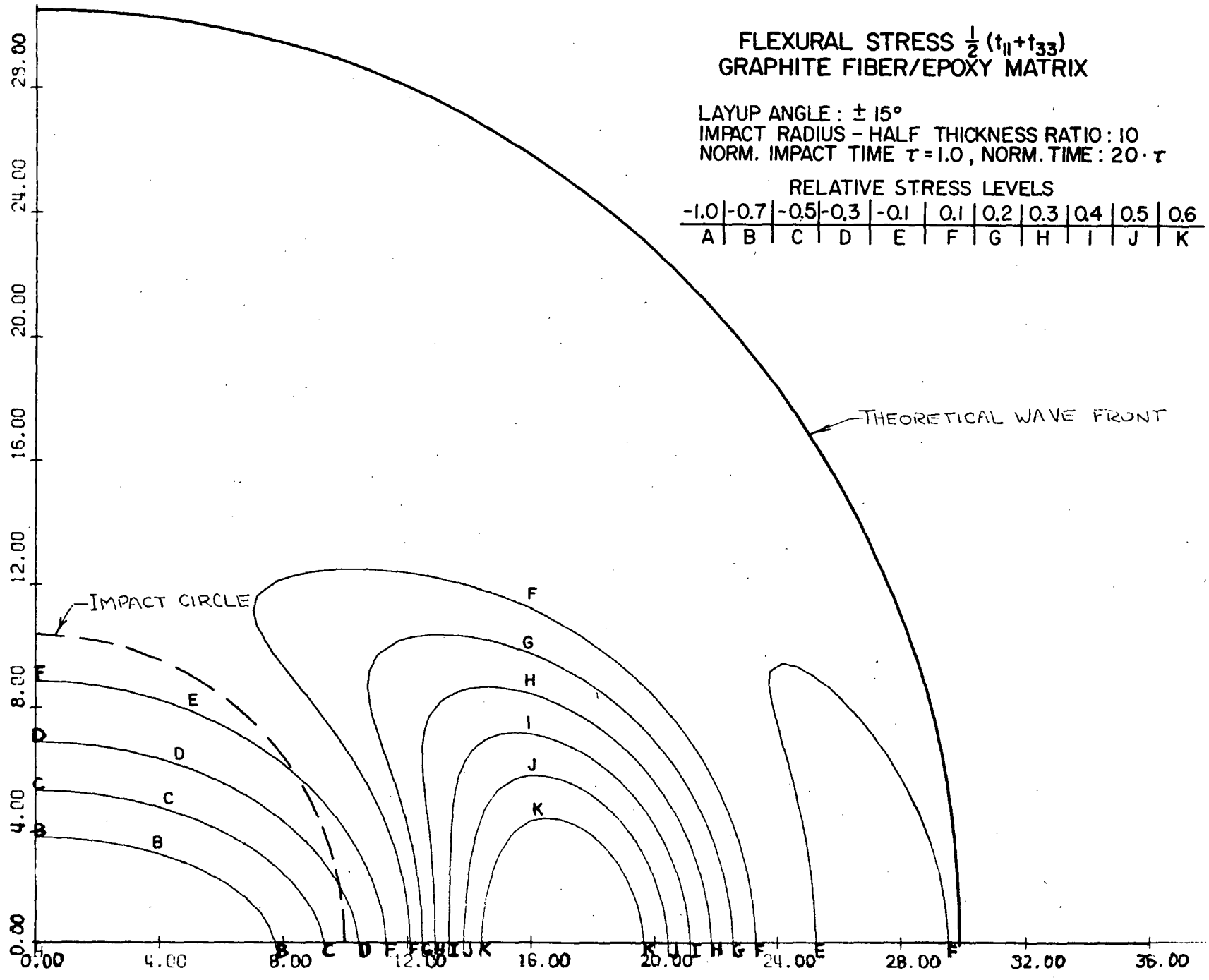
FLEXURAL STRESS $\frac{1}{2}(t_{11}+t_{33})$
GRAPHITE FIBER/EPOXY MATRIX
LAYUP ANGLE : ± 15°
IMPACT RADIUS - HALF THICKNESS RATIO : 10
NORM. IMPACT TIME $\tau = 1.0$, NORM. TIME : $20 \cdot \tau$
RELATIVE STRESS LEVELS
-1.0 | -0.7 | -0.5 | -0.3 | -0.1 | 0.1 | 0.2 | 0.3 | 0.4 | 0.5 | 0.6
A | B | C | D | E | F | G | H | I | J | K
THEORETICAL WAVE FRONT
IMPACT CIRCLE
0.00
4.00
8.00
12.00
16.00
20.00
24.00
28.00
32.00
36.00

FIGURE 20

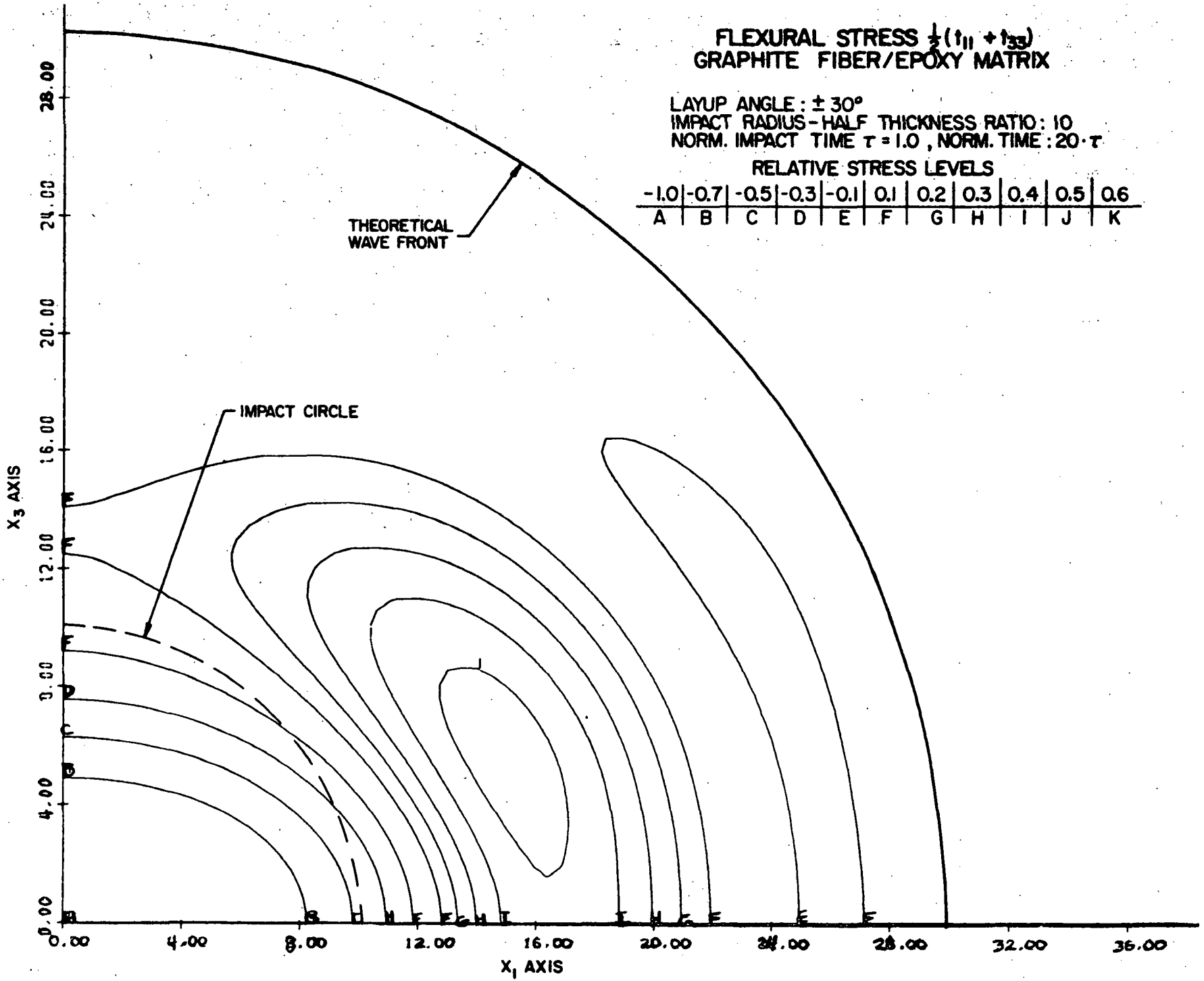
FLEXURAL STRESS $\frac{1}{2}(t_{11} + t_{33})$
GRAPHITE FIBER/EPOXY MATRIX
LAYUP ANGLE : ± 30°
IMPACT RADIUS - HALF THICKNESS RATIO : 10
NORM. IMPACT TIME τ = 1.0 , NORM. TIME : 20·τ
RELATIVE STRESS LEVELS
-1.0 | -0.7 | -0.5 | -0.3 | -0.1 | 0.1 | 0.2 | 0.3 | 0.4 | 0.5 | 0.6
A | B | C | D | E | F | G | H | I | J | K
THEORETICAL WAVE FRONT
IMPACT CIRCLE
X_3 AXIS
X_1 AXIS
0.00
4.00
8.00
12.00
16.00
20.00
24.00
28.00
32.00
36.00

FIGURE 21

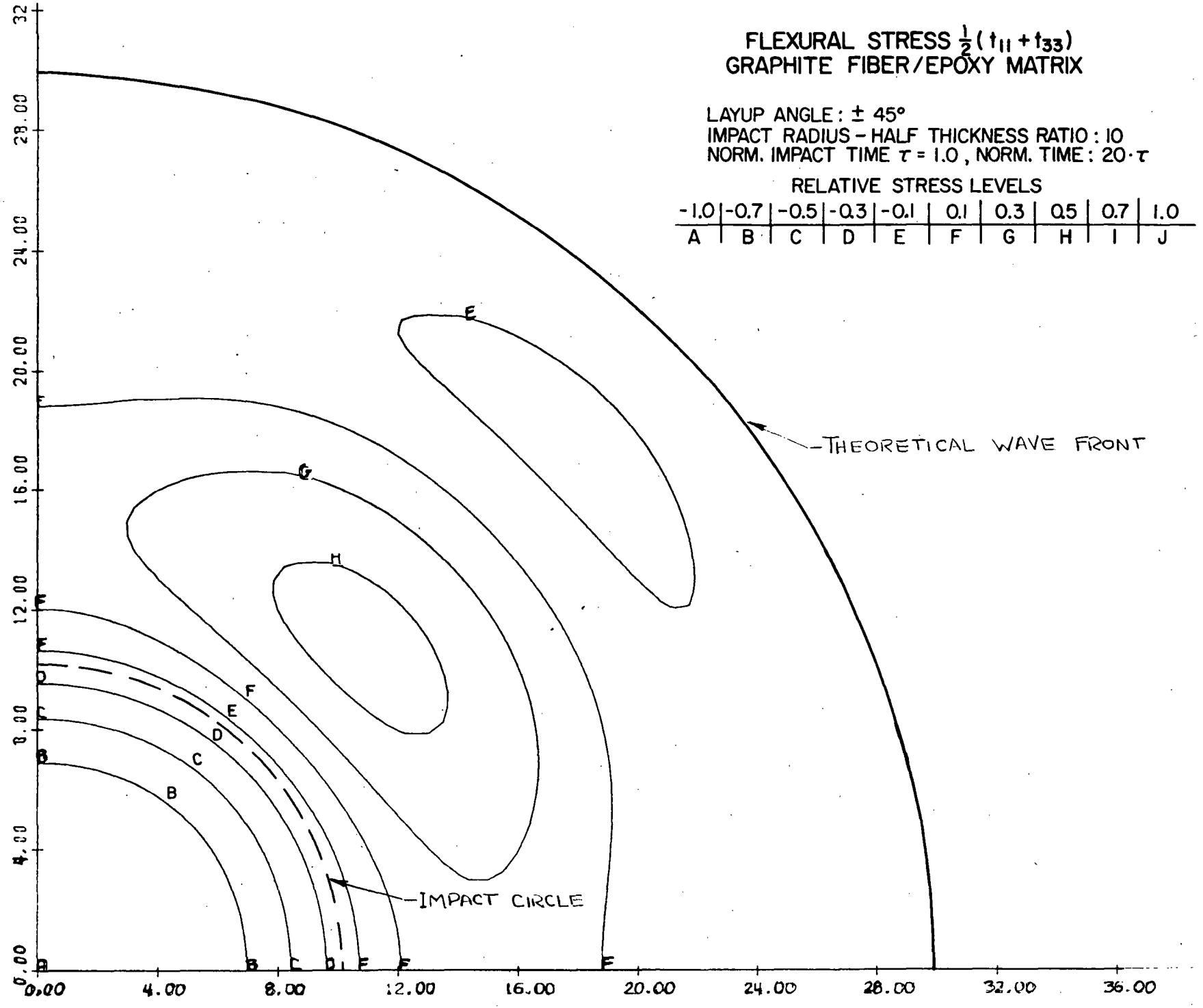
FLEXURAL STRESS $\frac{1}{2}(t_{11}+t_{33})$
GRAPHITE FIBER/EPOXY MATRIX
LAYUP ANGLE : ± 45°
IMPACT RADIUS – HALF THICKNESS RATIO : 10
NORM. IMPACT TIME τ = 1.0 , NORM. TIME : 20·τ
RELATIVE STRESS LEVELS
-1.0 | -0.7 | -0.5 | -0.3 | -0.1 | 0.1 | 0.3 | 0.5 | 0.7 | 1.0
A | B | C | D | E | F | G | H | I | J
THEORETICAL WAVE FRONT
IMPACT CIRCLE
0.00
4.00
8.00
12.00
16.00
20.00
24.00
28.00
32.00
36.00

FIGURE 22

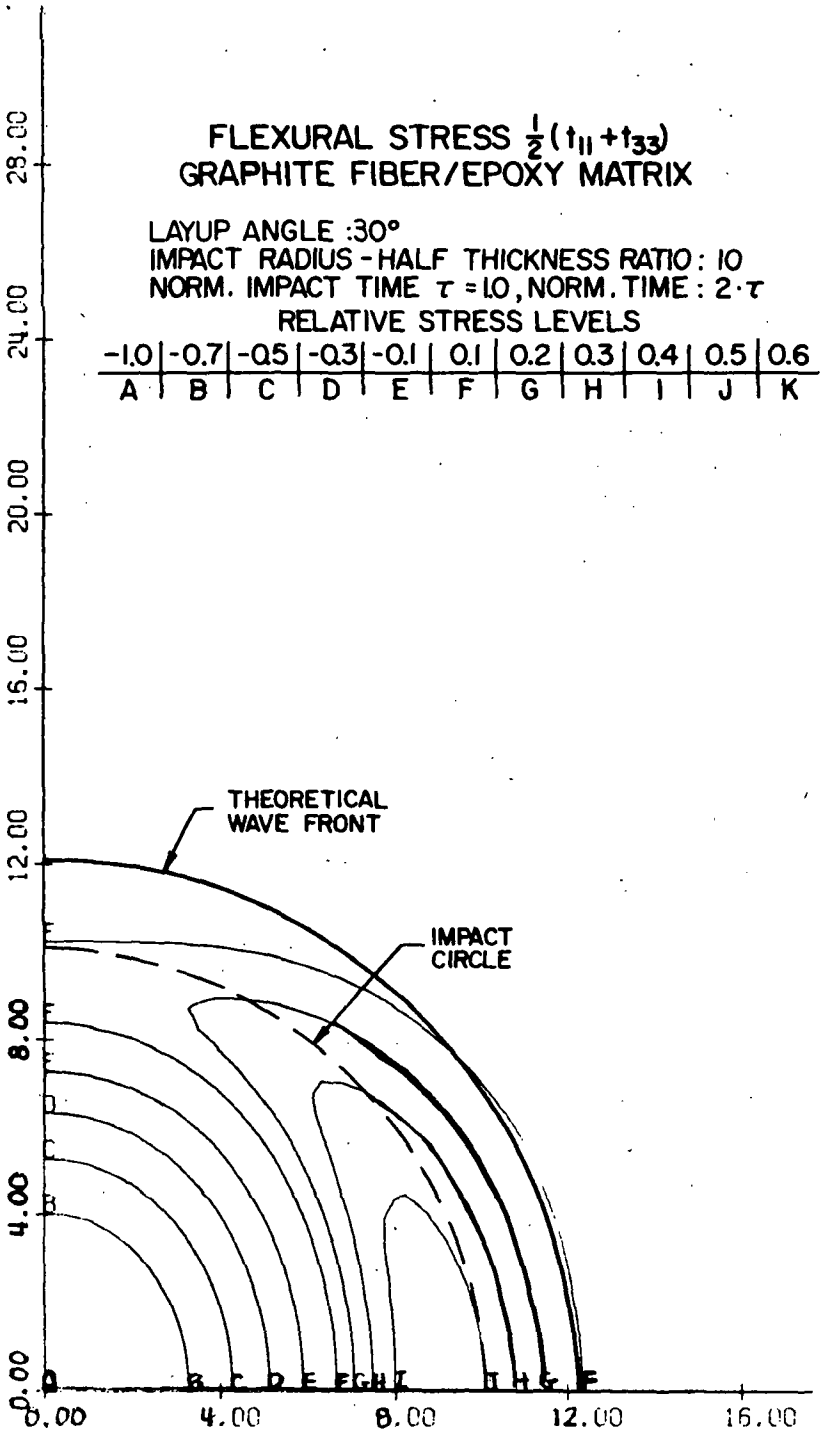
FLEXURAL STRESS $\frac{1}{2}(t_{11}+t_{33})$
GRAPHITE FIBER/EPOXY MATRIX
LAYUP ANGLE :30°
IMPACT RADIUS - HALF THICKNESS RATIO: 10
NORM. IMPACT TIME τ = 1.0, NORM. TIME : 2·τ
RELATIVE STRESS LEVELS
-1.0 | -0.7 | -0.5 | -0.3 | -0.1 | 0.1 | 0.2 | 0.3 | 0.4 | 0.5 | 0.6
A | B | C | D | E | F | G | H | I | J | K
THEORETICAL WAVE FRONT
IMPACT CIRCLE
0.00
4.00
8.00
12.00
16.00
20.00
24.00
28.00

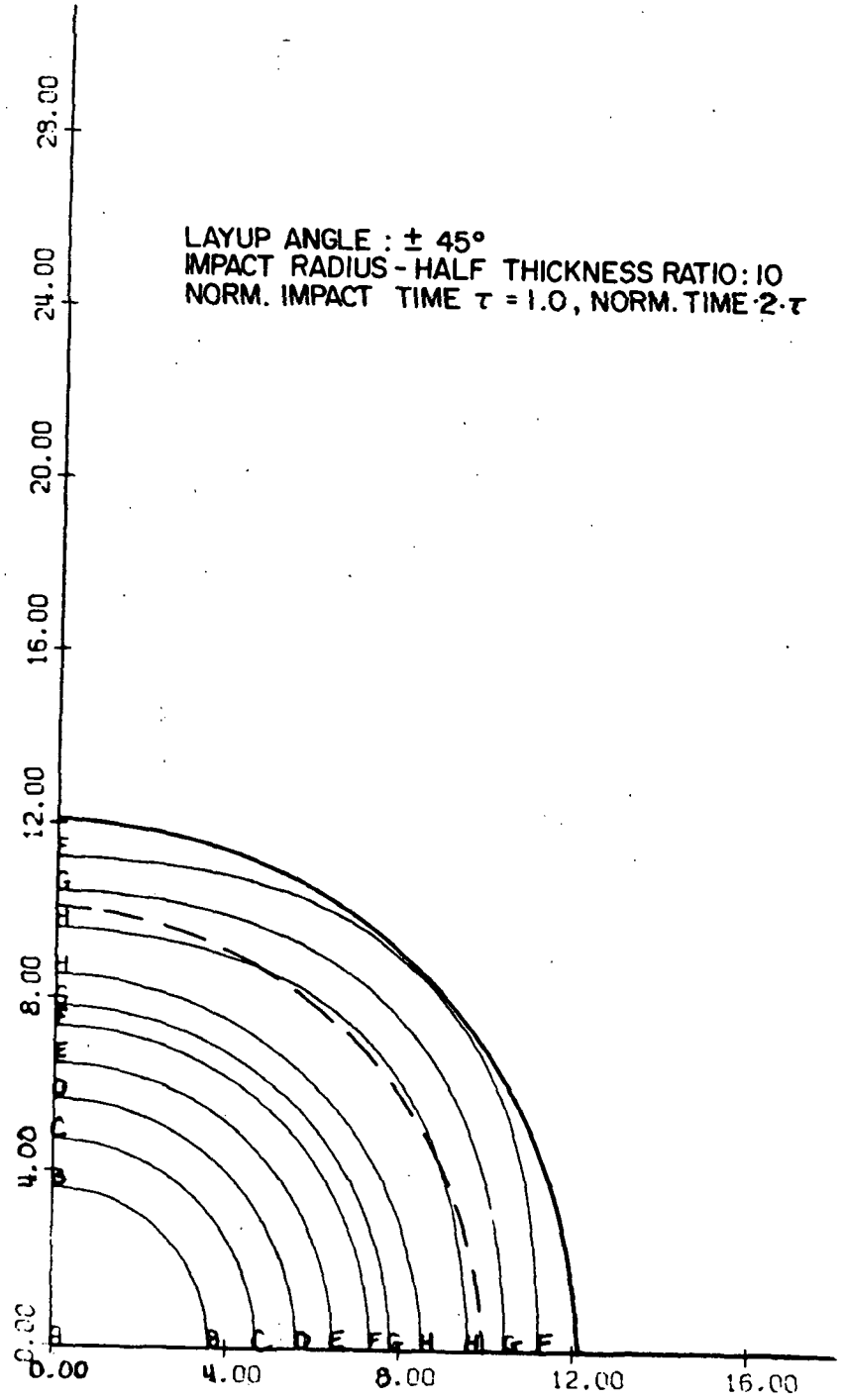
LAYUP ANGLE : ± 45°
IMPACT RADIUS - HALF THICKNESS RATIO: 10
NORM. IMPACT TIME τ = 1.0, NORM. TIME·2·τ
0.00
4.00
8.00
12.00
16.00
20.00
24.00
28.00

FIGURE 23

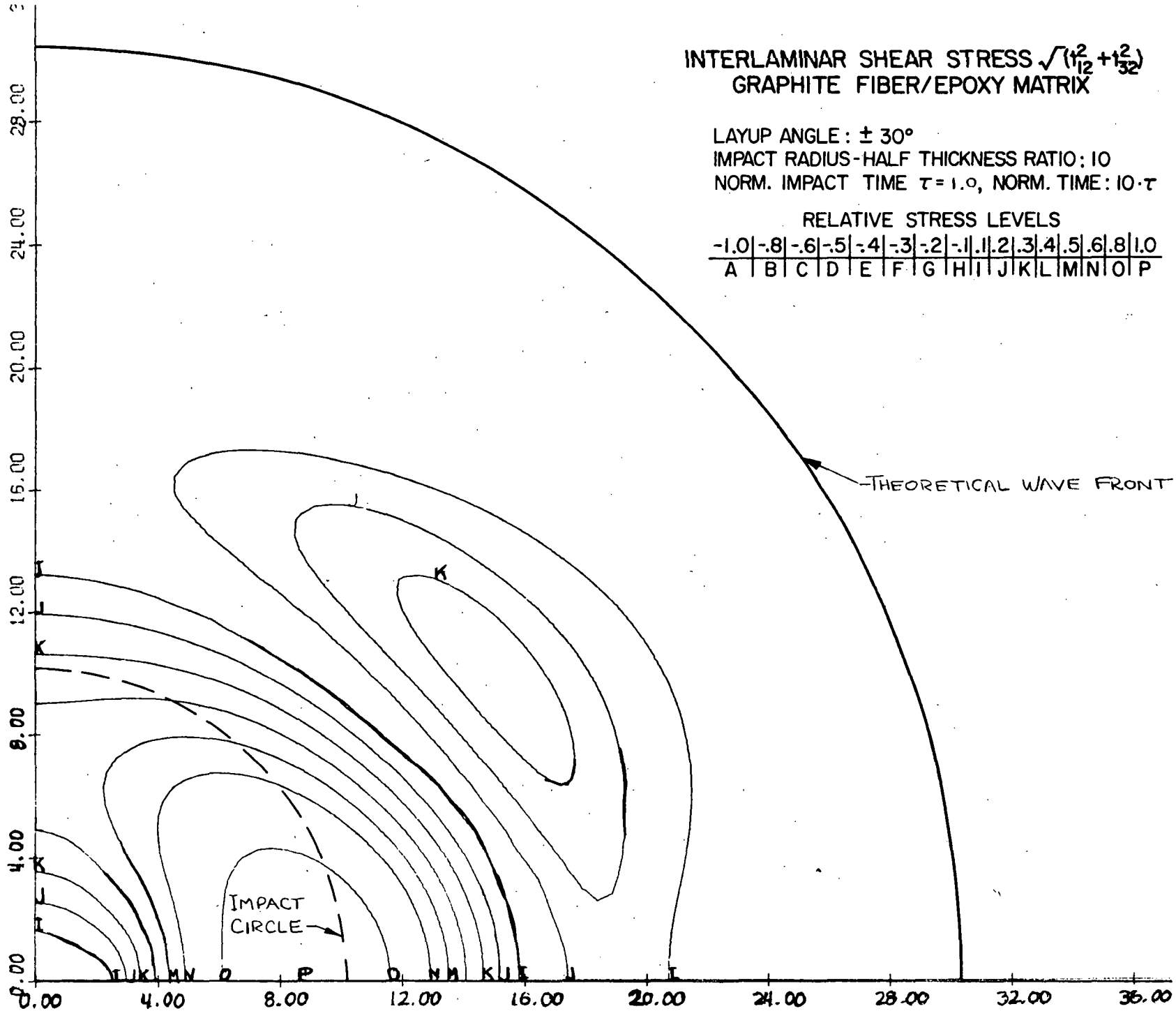
INTERLAMINAR SHEAR STRESS $\sqrt{(t_{12}^2 + t_{32}^2)}$
GRAPHITE FIBER/EPOXY MATRIX
LAYUP ANGLE : ± 30°
IMPACT RADIUS-HALF THICKNESS RATIO : 10
NORM. IMPACT TIME τ = 1.0, NORM. TIME : 10·τ
RELATIVE STRESS LEVELS
-1.0 | -.8 | -.6 | -.5 | -.4 | -.3 | -.2 | -.1 | .1 | .2 | .3 | .4 | .5 | .6 | .8 | 1.0
A | B | C | D | E | F | G | H | I | J | K | L | M | N | O | P
THEORETICAL WAVE FRONT
IMPACT CIRCLE
0.00
4.00
8.00
12.00
16.00
20.00
24.00
28.00
32.00
36.00

FIGURE 24

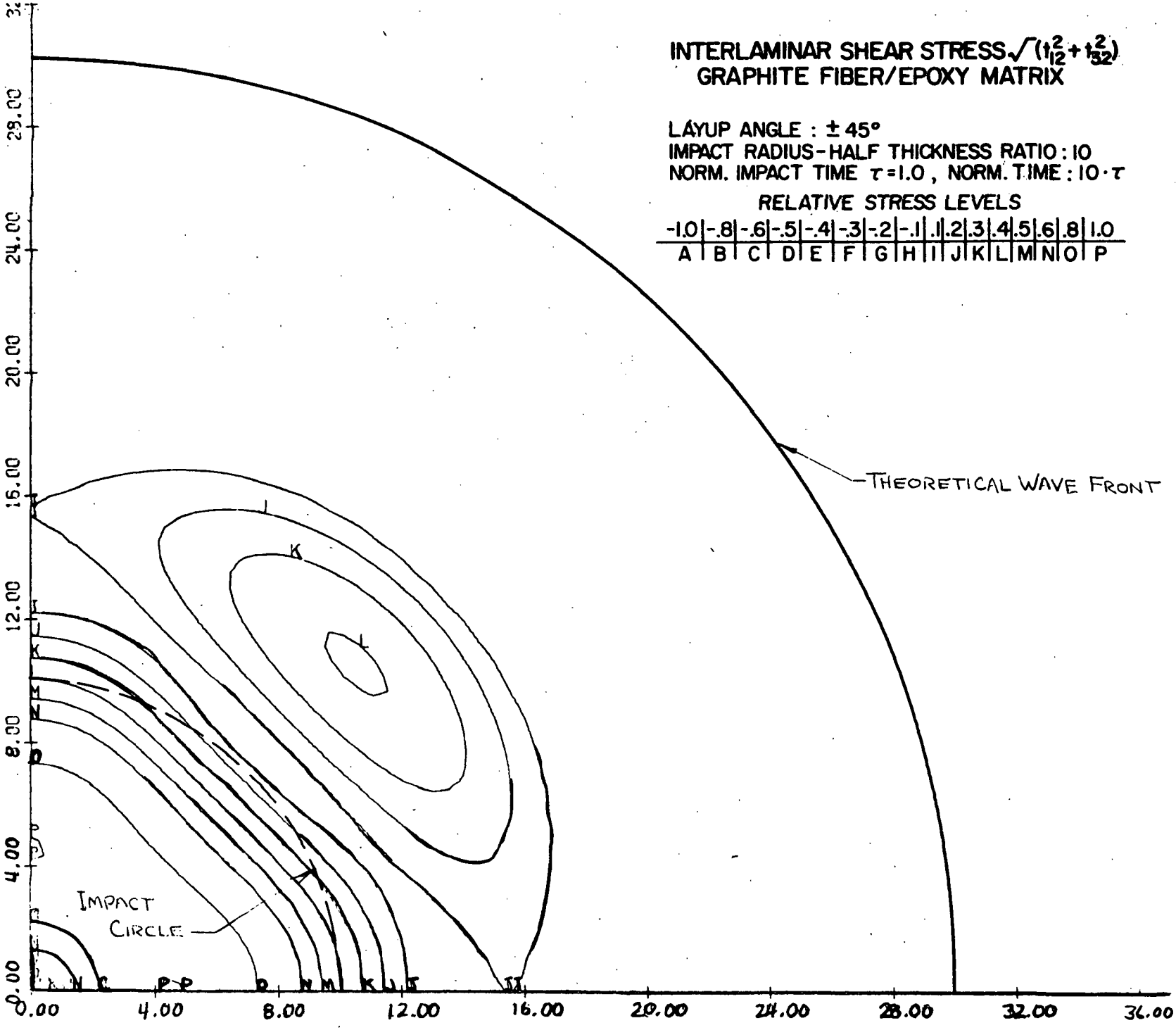
INTERLAMINAR SHEAR STRESS $\sqrt{(t_{12}^2 + t_{32}^2)}$
GRAPHITE FIBER/EPOXY MATRIX
LAYUP ANGLE : ± 45°
IMPACT RADIUS-HALF THICKNESS RATIO : 10
NORM. IMPACT TIME τ = 1.0 , NORM. TIME : 10·τ
RELATIVE STRESS LEVELS
-1.0 | -.8 | -.6 | -.5 | -.4 | -.3 | -.2 | -.1 | .1 | .2 | .3 | .4 | .5 | .6 | .8 | 1.0
A | B | C | D | E | F | G | H | I | J | K | L | M | N | O | P
THEORETICAL WAVE FRONT
IMPACT CIRCLE
0.00
4.00
8.00
12.00
16.00
20.00
24.00
28.00
32.00
36.00

FIGURE 25

TRANSVERSE DISPLACEMENT
GRAPHITE FIBER/EPOXY MATRIX

LAYUP ANGLE : ± 45°
IMPACT RADIUS - HALF THICKNESS RATIO : 10
NORM. IMPACT TIME $\tau = 0.5$, NORM. TIME : $3 \cdot \tau$

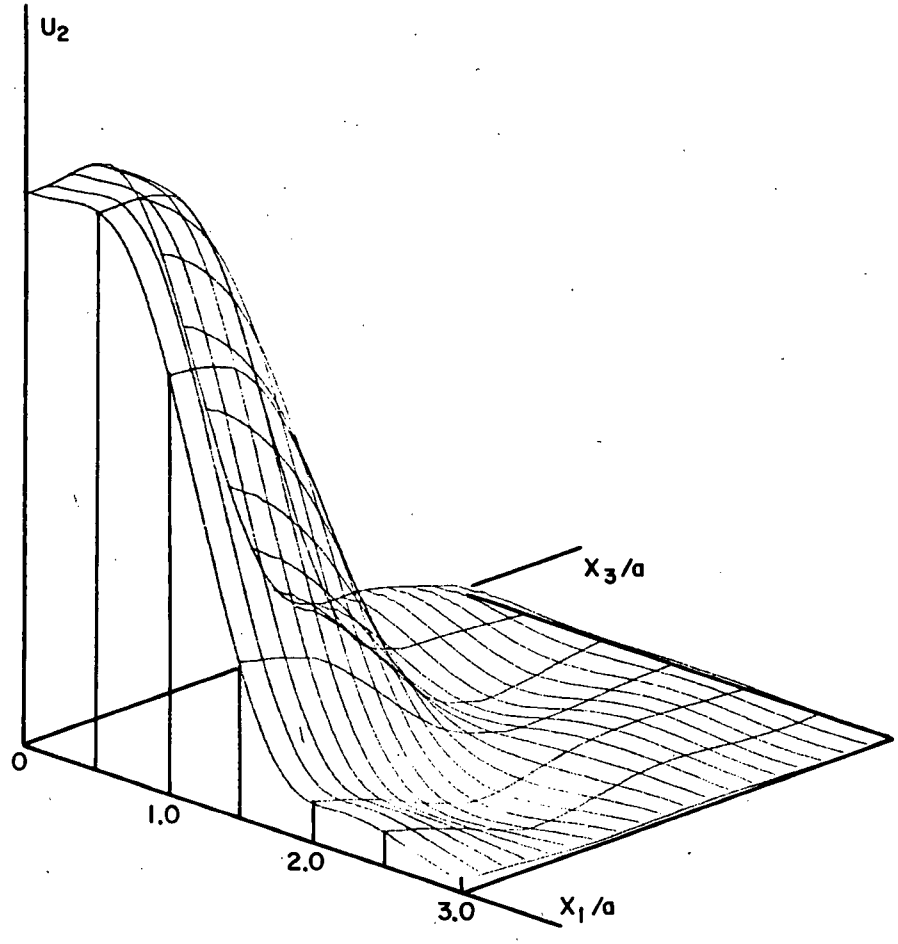

FIGURE 26

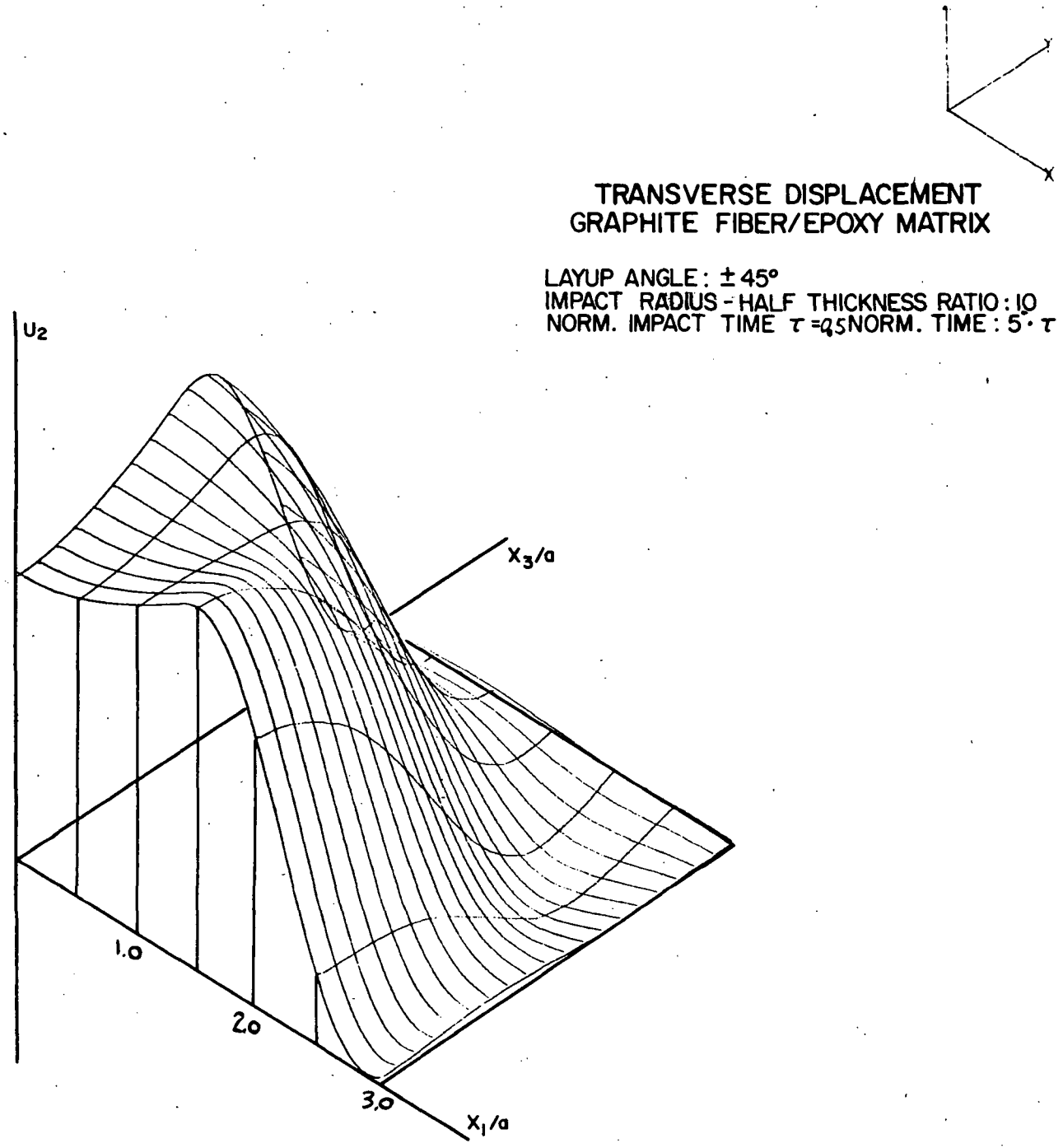
TRANSVERSE DISPLACEMENT
GRAPHITE FIBER/EPOXY MATRIX
LAYUP ANGLE: ±45°
IMPACT RADIUS - HALF THICKNESS RATIO: 10
NORM. IMPACT TIME τ = 0.5 NORM. TIME: 5·τ
U2
X3/a
1.0
2.0
3.0
X1/a

FIGURE 27

FIGURE 28

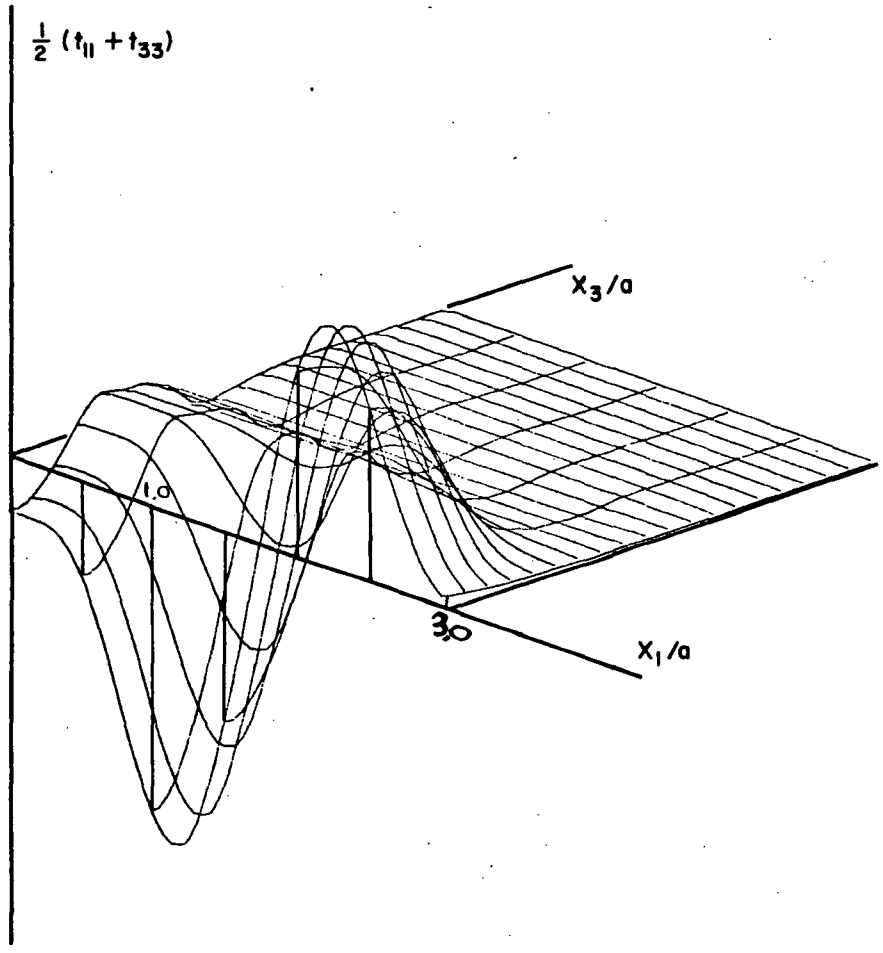

Mean In-Plane Stress Profile After Impact

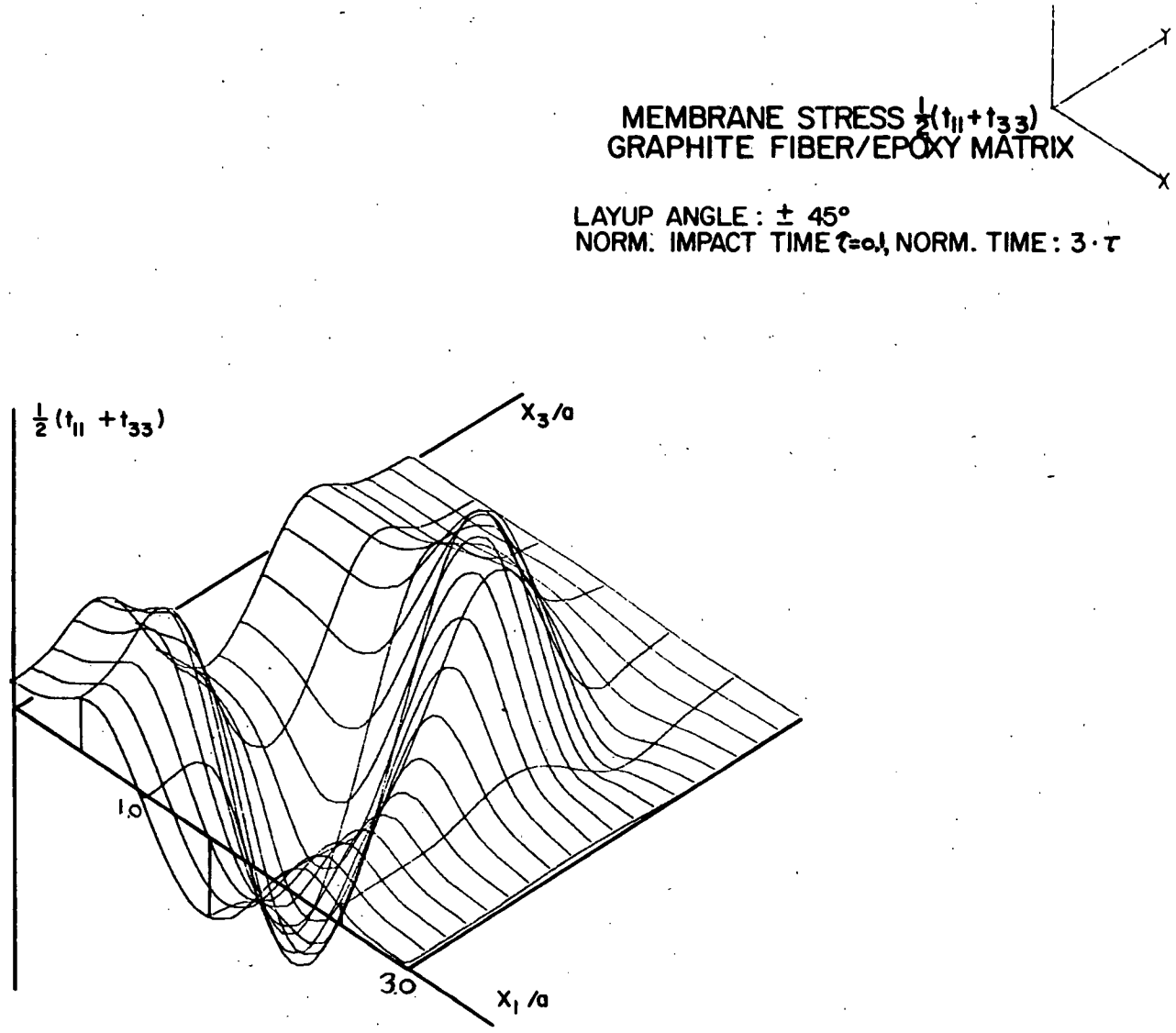
MEMBRANE STRESS $\frac{1}{2}(t_{11}+t_{33})$
GRAPHITE FIBER/EPOXY MATRIX
LAYUP ANGLE : ± 45°
NORM. IMPACT TIME τ=0.1, NORM. TIME : 3·τ
Y
X
$\frac{1}{2}(t_{11}+t_{33})$
X_3/a
1.0
3.0
X_1/a

FIGURE 29

FLEXURAL STRESS $\frac{1}{2}(t_{11}+t_{33})$
GRAPHITE FIBER/EPOXY MATRIX

LAYUP ANGLE : ± 45°
IMPACT RADIUS - HALF THICKNESS RATIO : 10
NORM. IMPACT TIME τ = 1.0 ,NORM. TIME : 10·τ

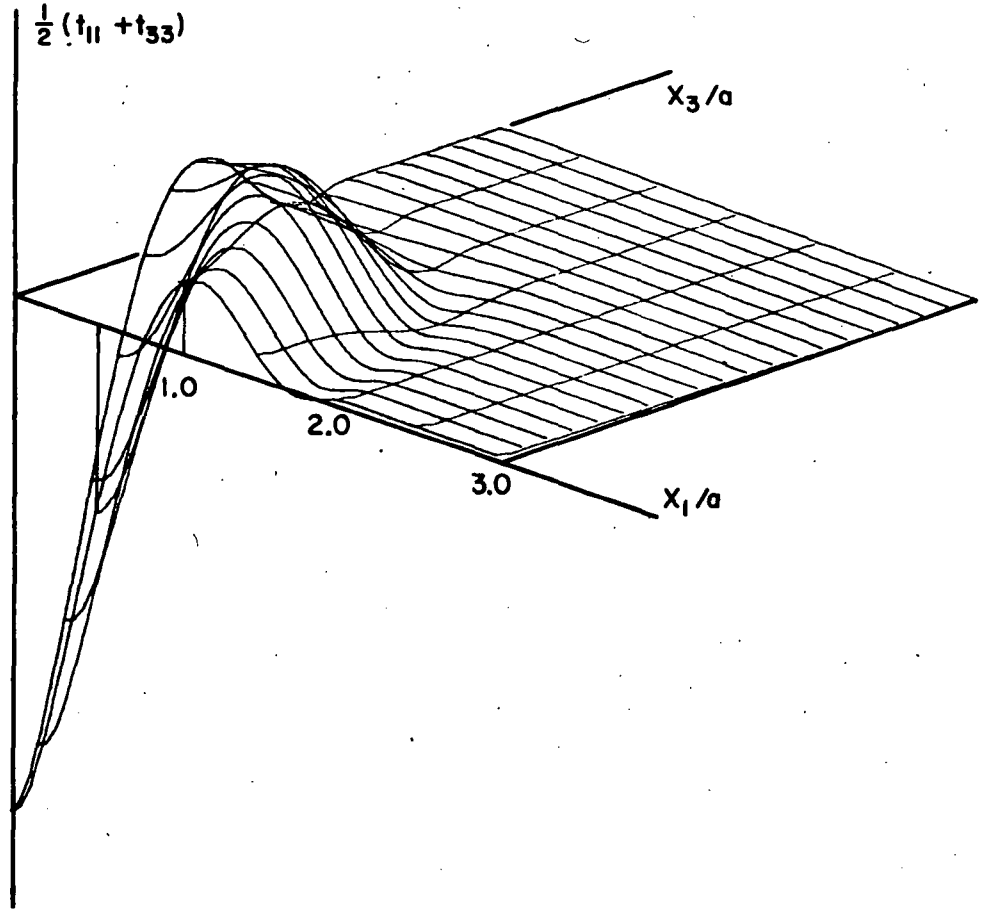

FIGURE 30

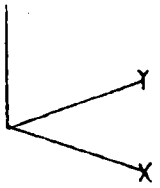

FLEXURAL STRESS $\frac{1}{2}(t_{11}+t_{33})$
GRAPHITE FIBER/EPOXY MATRIX

LAYUP ANGLE : ± 45°
IMPACT RADIUS - HALF THICKNESS RATIO : 10
NORM. IMPACT TIME τ = 1.0 , NORM. TIME : 20·τ

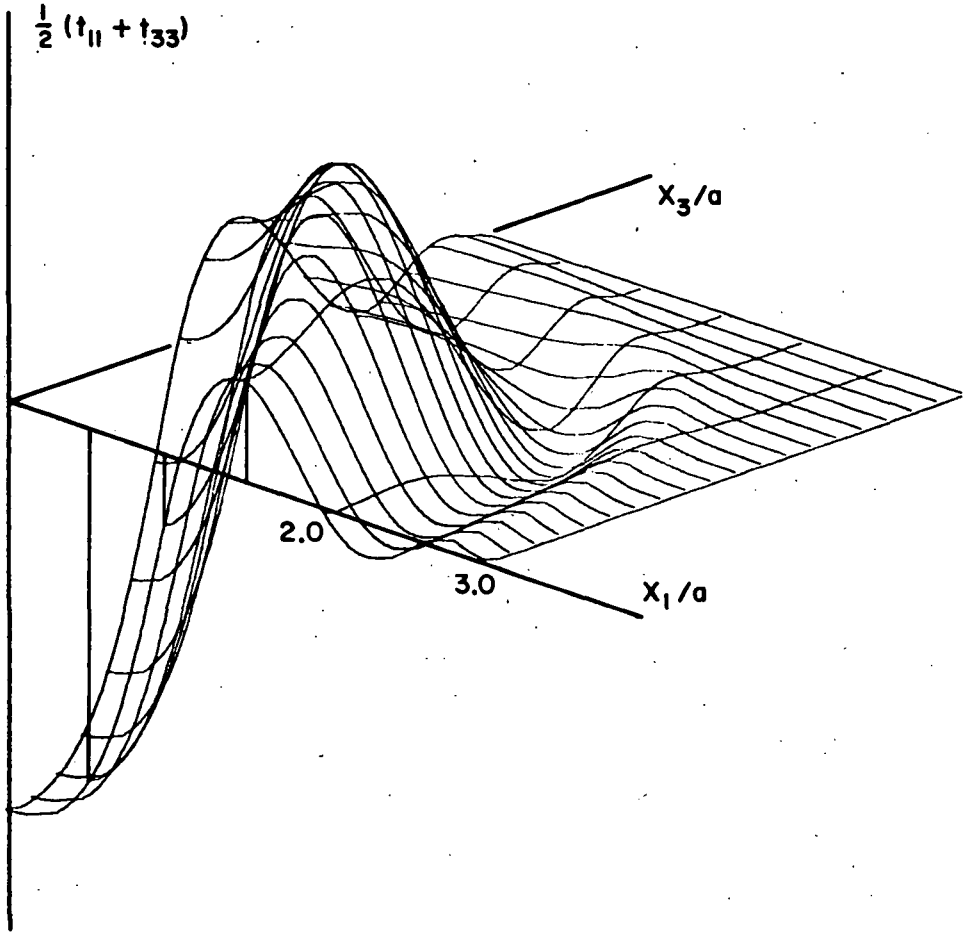

FIGURE 31

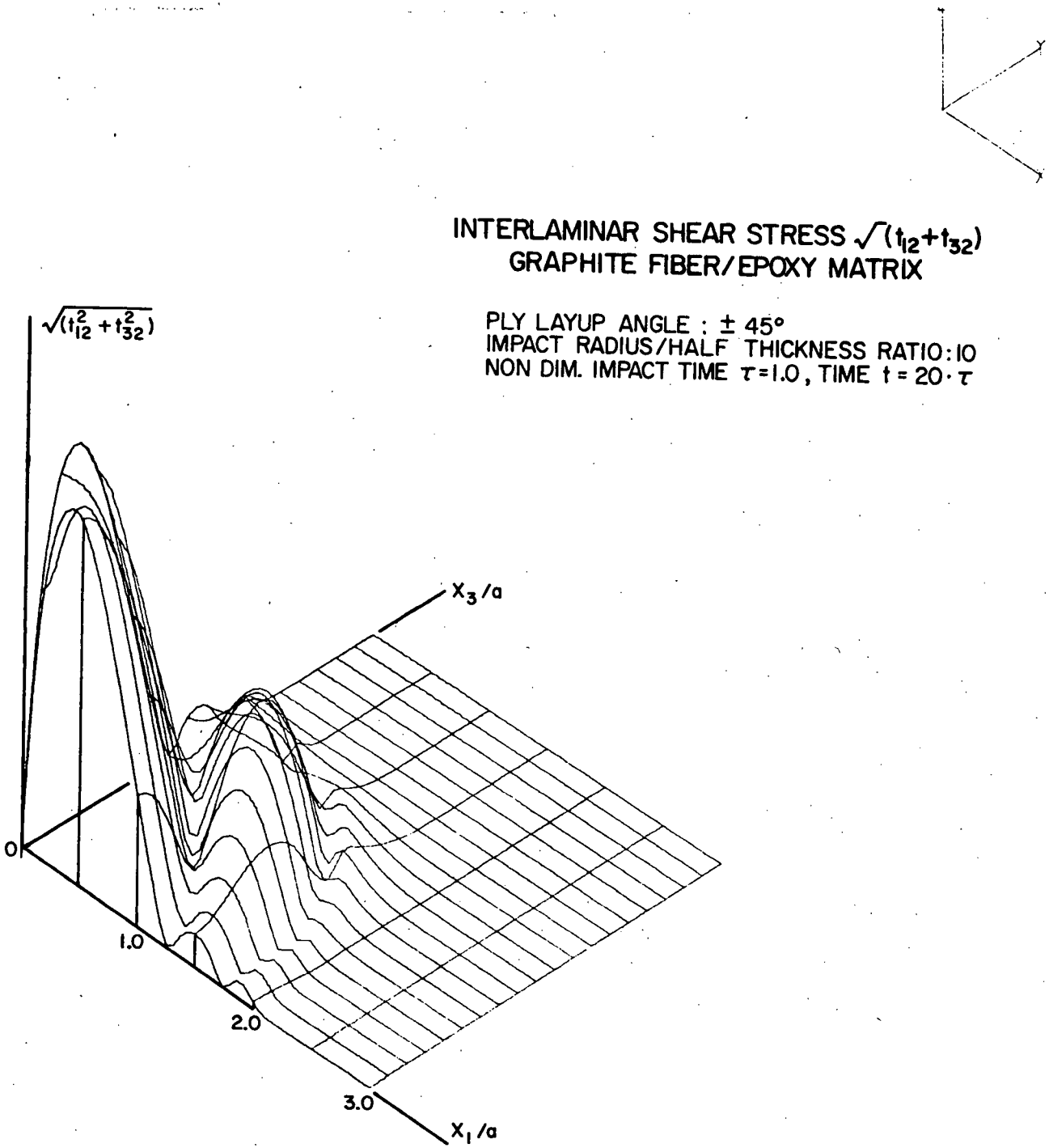
INTERLAMINAR SHEAR STRESS $\sqrt{(t_{12}+t_{32})}$
GRAPHITE FIBER/EPOXY MATRIX
PLY LAYUP ANGLE : ± 45°
IMPACT RADIUS/HALF THICKNESS RATIO: 10
NON DIM. IMPACT TIME τ=1.0, TIME $t = 20 \cdot \tau$
$\sqrt{(t_{12}^2 + t_{32}^2)}$
X_3/a
0
1.0
2.0
3.0
X_1/a

FIGURE 32

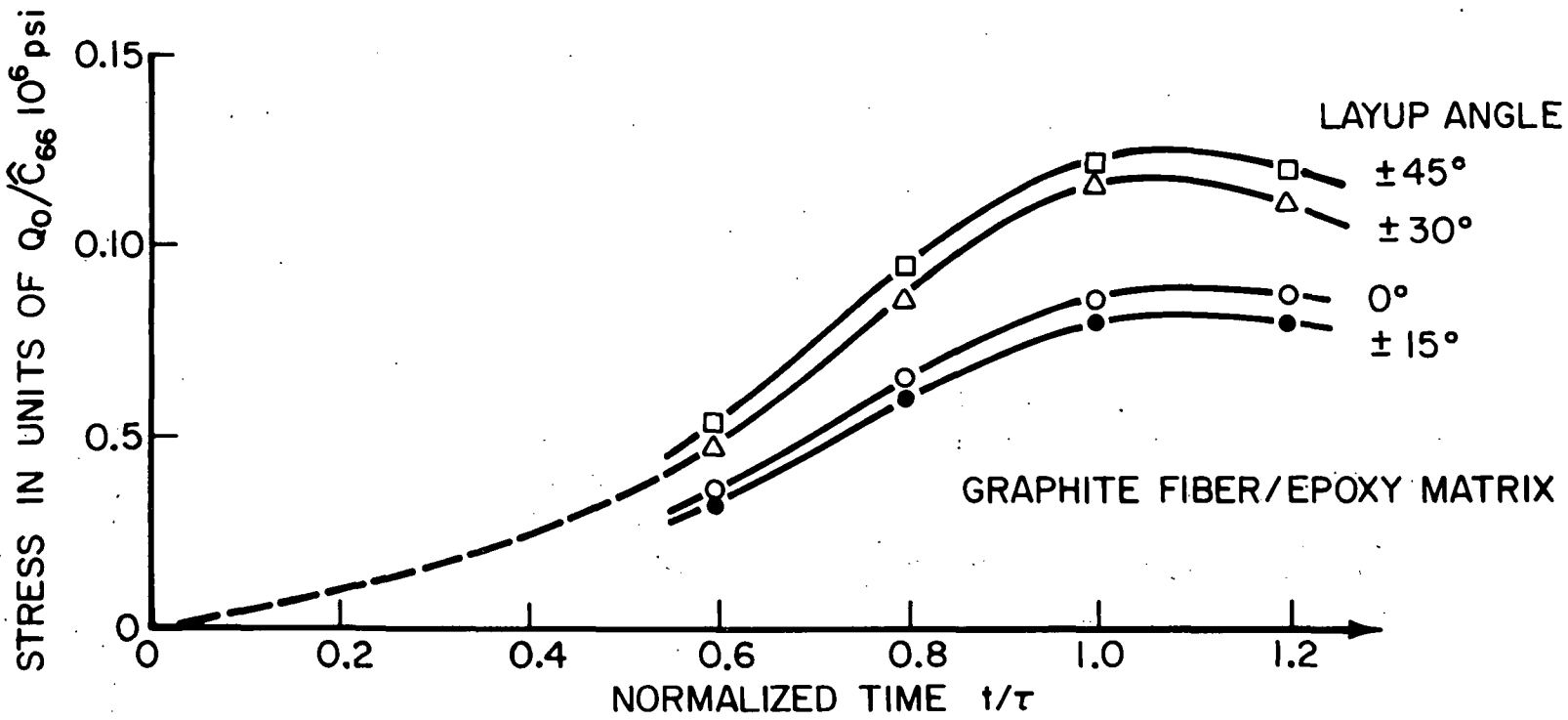

FLEXURAL STRESS $t_{11} + t_{33}$ AT ORIGIN vs TIME, $a/b = 1.0$

NORMALIZED CONTACT TIME $\tau V_3/b = 1.0$ ($V_3 = 1.18$ mm/μ sec)

FIGURE 33

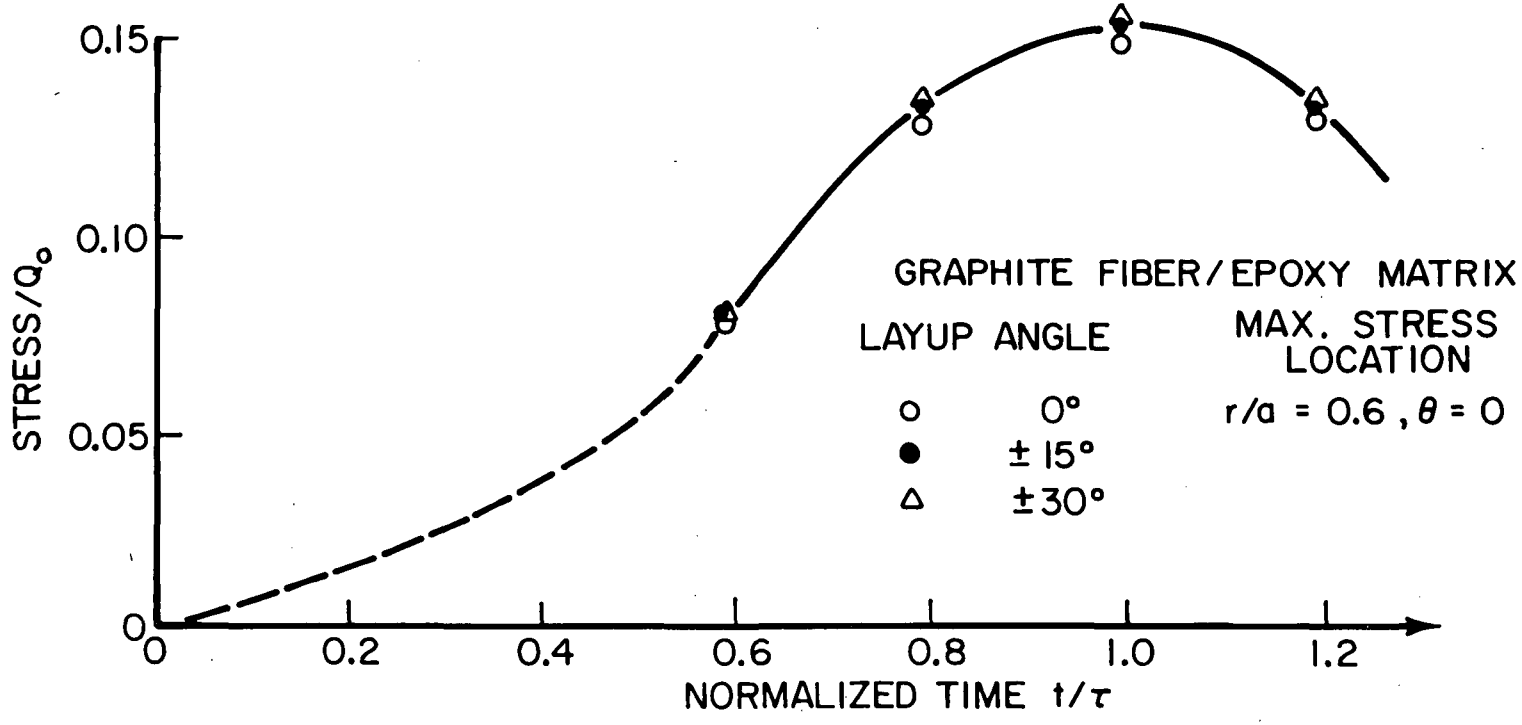

FLEXURAL STRESS $\left[t_{12}^2 + t_{32}^2\right]^{1/2}$ vs TIME FOR a/b = 1.0 ,
NORMALIZED CONTACT TIME $\tau V_3/b = 1.0$ (V_3 = 1.18 mm/μsec

FIGURE 34